Influence of embedded surface patterns on the performance of automotive, box beam, aluminum crash absorbers.

Omer Masood Qureshi

PhD Thesis

XXIV Cycle
'Enzo Ferrari' Faculty of Engineering
University Of Modena E Reggio Emilia,
Modena, Italy
March 2012

Tutor:
Dr. Antonio Strozzi

Co Tutor:
Dr. Enrico Bertocchi
Dr. Andrea Baldini

Hayay Abba ji, Kithay Phasaya Jay ?

Publications associated with this thesis:

International Journals:

1. O. M. Qureshi, E. Bertocchi, Crash behavior of thin-walled box beams with complex sinusoidal relief patterns, Thin-Walled Structures 53 (2012) 217–223.

(Based on work done in Chapter 3)

2. O. M. Qureshi, E. Bertocchi, Crash performance of notch triggers and variable frequency progressive-triggering on patterned box beams during axial impacts, Submitted for publication, (2012), Thin Walled Structures.

(Based on work done in Chapter 4)

3. O. M. Qureshi, E. Bertocchi, Oblique impact performance of pattern embedded box beams with notch and progressive triggers, Submitted for publication, (2012), International Journal of Crashworthiness.

(Based on work done in Chapter 5)

Conferences:

1. Omer Masood Qureshi, Thin-walled box beams with complex sinusoidal relief patterns, Oral presentation, 4th GACM Colloquium on Computational Mechanics, Dresden, August 31 - September 2, 2011.

2. Omer Masood Qureshi, Improvement of crash absorber beams through embedded sinusoidal surface patterns: FEM testing and trigger design, proceedings of the International Conference on Transportation and Logistics Engineering, Phuket, December 21 - 23, 2011.

Abstract

This thesis proposes a new automotive box-beam crash absorber design with sinusoidal patterns embedded on the beam surfaces. Six different types of surface patterns were initially proposed and a total of 63 samples were simulated using the commercial pre-processor HyperCrash™ and the commercial explicit FEM solver RADIOSS™. The aim of the study is to improve energy absorption properties of the beams by controlling the wavelength of progressive buckle formations and obtaining denser collapse formations. It was found that the relief patterns could be used effectively to change the buckling modes and reduce the buckle wavelength. A maximum of 42 percent increase in the amount of total energy absorbed and an increase in the energy efficiency factor from 1.08 to 1.54 was observed moving from the reference model to the most optimized design

The viability of using conventional notch triggers on patterned beams is also evaluated. A progressive triggering mechanism on box beams with embedded patterns is also proposed by a novel idea of using a variable pattern throughout the length of the beam. In these progressively triggered beams, the reaction force slightly increases with each progressive collapse buckle formation throughout the collapse. An extensive FEM study is performed and it is found that, as opposed to point triggers, progressive triggering through variable pattern formulation effectively triggers and initiates a more stable collapse. More importantly, progressive triggers cause less stray deformations elsewhere along the beam and are consequently much more robust against global bending.

Since majority of real world automotive impacts are not perfectly aligned to the axial direction, the third part of this thesis focuses on testing the proposed beams for performance in oblique and offset impacts. Three types of model setups are evaluated: 1) Aligned impact with an off center mass, 2) Impact with an oblique frictionless wall with a capped rigid impact end, 3) Impact with an oblique frictionless wall with a uncapped deformable impact end. A perimeter called the critical angle is defined and used as an effective performance indicator. It was found that the SLD beams with progressive triggering were superior in oblique and offset impacts as compared to the reference beams according to all three tests. They sustained the proffered

axial mode of collapse to a considerably higher mass-offset/inclination as compared reference beams and were less prone to global bending; while SLD beams with notch triggers performed almost comparable to the reference model. It is also noted that the offset mass test and the oblique test with uncapped ends is more prone to erratic readings as compared tests with capped impact ends.

It is concluded in this thesis that embedding beams with sinusoidal perturbations and triggering them with progressive variable frequency can improve both their energy absorption performance and oblique impact performance greatly.

A total of 478 HyperCrash™ simulations were run in the due course of this project. There are three international journal publications and two conference publications associated with this thesis.

Keywords: *Crash absorbers, Box beams, Automotive crash analysis,*

Table of Contents.

Acknowledgments:

I would like to thank my Ph.D Supervisor, Prof. Antonio Strozzi for giving me this opportunity to come and study in the university of Modena and guiding me throughout my degree, and to my co-supervisors Dr. Enrico Bertocchi, Dr. Matteo Giacopini, and Dr. Andrea Baldini who have constantly supported me throughout.

I am extremely grateful to my parents Masood and Rumana Qureshi, whose selfless untiring efforts enabled me to come this far, to my wife, Farah who stood by me all this time, and to my dear friends and colleagues, Luca Bertocchi, Giuseppe Mulas, Elenora Ciampioni, Sara Mantovani, Antonio Libbra, Francesca Tavoni and Sergio Gallo for making my stay in Italy a very memorable part of my life.

I would also like to thank Italy in general, for it is a country that I have immensely learned from – both in the field of automotive and otherwise.

Chapter 1. Introduction to automotive crash worthiness

1.1 Historical perspective

The idea occupant crash safety is almost as old as the concept of motor vehicles itself. As speeds rose and the usage of cars became more widespread, crash safety of vehicles developed remarkably over the course of the last century as an important field of study.

There are three distinct periods in the development of the subject of crashworthiness and occupant safety. The first period starts from the first recorded motor accident fatality in 1889 and till early into the next century to 1937. This was a period of genesis in which the first concepts of safety were conceived. Early designers focused on basic problems like pneumatic tire bursting that caused a complete loss of vehicle control, which still remains an issue today to the now completely obsolete issue of injuries caused by a manual engine cranking lever. Other now basic items like headlights to improve night visibility and Indicators that mimicked moving arms were first conceived in this era. Protection of occupants from catching fire in case of an accident was also one of the main focus in those early days of innovation and thus led to the development of 'engine-firewall'.

The second period was heralded by Auto Union AG. when they pioneered in conducting an experimental crash test program in 1937. They conducted frontal impact tests, side impact tests, a car pole impact and also the first rollover tests. These testes were very rudimentary and only visual post crash observations were done. Only the rollover tests could be captured on film as the rest of the tests were too fast to capture for the camera technology at that time. These studies were motivated by the aim to introduce cheaper building material such as wood and plastic instead of steel in car body structure. The pace of development accelerated across

the Atlantic too when General Motors also launched an impact test program. The first concept of the crash crumple zone was patented in 1951 by the Hungarian engineer Bela Barenyi. Bela did immense contributions to including crash safety steering wheel, safety door locks in the early 60's. He eventually amassed a staggering 2500 patents to his name and eventually became known as the 'Father of Crash safety engineering'

Fig. 1.1. A Car Wreck from 1907.

Significant breakthroughs in safety biomechanics were done by John Strapp, an early American pioneer who studied the effects of high accelerations on the human body during impacts, Often using himself as a test dummy. Strapp went on to organize the first conference on automotive safety in 1955. The conference recently celebrated its 50th meeting in 2006. This first meeting proposed things like moving dashboards, energy absorbing padding, safety locks and bumper design for crash.

The first proper sled tests also appeared in the 50s. Interestingly, it was observed then that the probability to survive in an automotive crash at 50km/h was almost zero, many of the fatalities happened because occupants were thrown of the vehicles. The interior of the vehicle was adequate to prevent head injuries and the steering wheel and dashboard had tremendous room crash issues.

But perhaps the biggest pinnacle of this time was the invention of the three point seat belt. It was invented by Nils Bohlin and first offered in Volvo cars in 1959. To this day, his invention continues to save millions of lives worldwide.

The third and final phase arrived in 1966 when the first road safety acts and regulations were passed. During the post-regulatory phase a number of government regulations were passed which the every new vehicle model had to comply with to be given a road worthy certificate. These standards, known as the Federal Motor Vehicle Safety Standards (FMVSS), made it mandatory for manufacturers to comply with and thus brought the subject into a mainstream consideration. These standards have evolved vastly since then and now cover a wide range of scenarios from pedestrian safety to vehicle rollovers.

The field diversified in this boom period, Finite element modeling techniques developed and the crash simulation became a superbly helpful tool in design and testing of vehicles. The boost in electronics gave new innovative safety devices such as anti lock brakes, pre-collision detection and traction controls.

The formation of NCAP tests (new car accreditation program) in the 1990s was yet another leap forward in automotive safety. These tests did not mandate anything, rather offered a safety rating for each car on a five star based system. This made safety a more marketable and standardized property for the car manufacturers. Car buyers were able to accurately guage a vehicles safety through an independent body as opposed to the manufacturers claims. Companies began to invest more in safety and strived to aim for higher NCAP ratings in their designs. The NCAP ratings, which were initially criticized to be unachievable and stringent, eventually raised the standard of safety higher. Volvo S40 became the first car to achieve a 4 star rating in 1997. Three years later in 2001, Renault Laguna became the first car to achieve a full five star rating. There have been many cars with five star rating since.

Fig. 1.2. Daihatsu Charade NCAP frontal offset test with a deformable barrier.

The future offers endless possibilities. Automakers are collaborating together on crash safety such as vehicle aggressivity i.e. the propensity of a vehicle to cause damage to the occupant of the 'other' vehicle in a crash. and crash compatibility between different vehicles. Regulations for crash compatibility might appear soon. Electronic based 'Smart' devices will appear which will behave according to occupants size, and gender and position in case of a crash.

More advancement is foreseen in active safety devices which will try to pre-detect and prevent a crash altogether. These devices will eventually be made mandatory through regulations and the near future could possibly even see automotive crashes as a thing of the past.

1.2 Vehicle structure

The car structure has evolved over the past century in the pursuit of many different design objectives, some of which have been in direct conflict with other. Exterior shapes have been dictated by good aerodynamic properties. Performance and fuel efficiency has favored the use of lightweight structures, occupant comfort and luxury have paved way for a comfortable cabin design with many facilities. Additionally, aesthetics has also been a great driving force, and lately, safety during crashes is now one of the key design parameters.

Currently there are two major types of car body structures: body over frame structure and the unit body structure. The body over frame configuration is used in larger vehicles such as SUVs and light trucks. The chassis frame forms the backbone of the vehicle and supports everything above that. In case of frontal impacts, the front chassis and the sheet metal absorbs the maximum amount of force.

The unit body structure was first introduced in the US in 1980s in which the entire body frame and all structural components are made of stamped sheet metal and fastened together using spot welding and other fastening techniques to make a space frame. There is no separate chassis in the unit body design. This configuration offered higher rigidity and a lower weight as compared to the body over frame layout. Its usage grew since the 1980s; today, almost all passenger cars have this design.

Since there is no chassis, unit body structures have specifically designed crash absorbing beams, which function as structural members under normal conditions but also serve as energy absorbers during a crash. Fig.1 depicts a car unit- body structure with frontal crash absorbers.

Materials have also seen significant development, Steel had dominated as the structural component in cars since the entire century of car innovation. It was relatively cheap, widely available and a malleable material which offered adequate strength to be used as a building material.

Recently, the use of Aluminum body structures has been seen as a replacement of steel in high end car design. Aluminum is more lightweight and has a high strength to cost ratio as compared to steel and thus more desirable. It has a lower melting point in comparison and thus easier to form, extrude into components. Many mainstream luxury and sports cars nowadays boast a complete aluminum chassis.

Carbon-fiber is also a new exotic material for structural design but currently due to its high cost its usage is limited to extremely high end sport road vehicles such as the Pagani Zonda and Ferrari Enzo or outright race track formula vehicles.

1.3 Crash types

Car accidents are diverse in nature and each one is unique and different from the other. Vehicles may collide with each other or with stationary objects such as trees or poles etc. In case they collide with each other, their shape, size, bumper height and aggresivity may vary

greatly. In other cases multiple cars might be involved in a single car accident. The different combinations of speeds might have totally different results. These are just some of the factors to provide an insight on the complexities of accidents and their reconstruction and analysis faced by crash safety engineers in designing a road worthy vehicle. These same factors also complicate assessment of a vehicle for regulatory authorities who need to devise tests for gauging it.

Generally, for design classifications, engineers have classified impacts into four basic modes: frontal, side, rear and rollover crashes.

According to accident statistics collected worldwide, frontal impacts are the most common type of accidents that occur are frontal impacts. They account for 56 percent of all impacts that take place as shown in Fig. 1.3 and Fig. 1.4 The second likely mode of impact is sideways which accounts for 38 percent of accidents, while rear impacts are quite rare and only 6 percent of accidents happen that way.

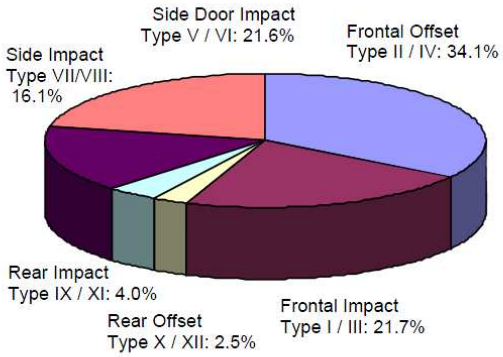

Fig. 1.3 Pie Chart showing percentages of automotive crashes

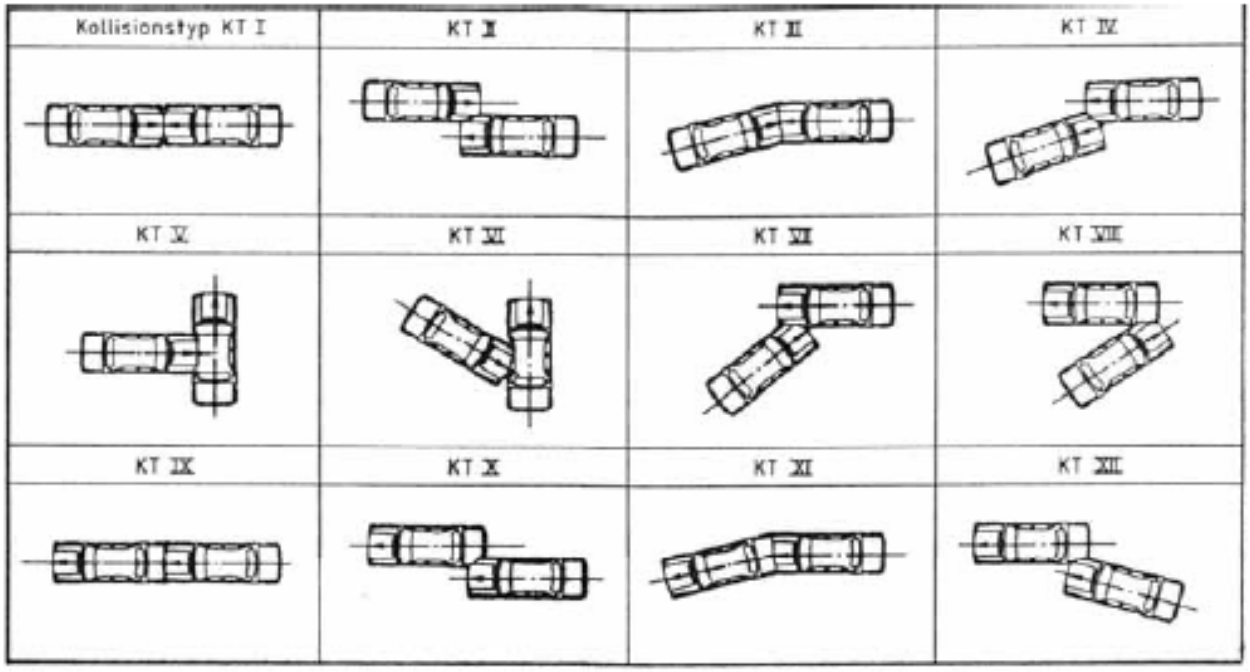

Fig. 1.4. Orientations of automotive crashes.

Until recently, the frontal impacts were considered as the most dangerous type of impacts and claimed an ample number of lives. However the compulsion of new restraints systems such as seat belts and airbags have and more importantly, the better design of the front crumple zone has made frontal impacts less and less severe with time.

Due to limited attention and limited space to work with, Such improvement has not been the case with side impacts. Side impacts now account more a greater proportion of serious injuries as compared to frontal impacts.

1.4 Regulatory and rating crash tests

Planning accurate crash tests for vehicles is as complicated a task for regulatory authorities as it is for design a safe car. Newer and newer crash tests and designed and the criteria constantly improved each year. Test standards vary from country to country. America follows FMVSS standards and the EU follows the ECE standards.

Despite the amazing amount of advancement that has undergone in the field of Finite element modeling and simulations. The real test of vehicles has to be done in reality on a crash test jig. This is especially true as far as the certification authorities are concerned. But not undermine the importance of Finite Element Methods. Automakers extensively use them with a fair bit of accuracy. This shortens the design cycle, reduces cost and ensures that the first physically made prototype is bound to work.

The Testing criteria is roughly divided into three parts:

1) **Pre-Crash Phase** - Active Safety / Crash Avoidance.
   (100 Series in FVMSS tests)

   Eg: Braking (ABS), electronic stability control (ESC), lighting and signaling

2) **Crash Phase** - Passive Safety / Crashworthiness.
   (200 Series in FVMSS tests)

   Eg: Frontal impact (FVMSS-208), Side Impact Protection (FVMSS-214), Rollover test (FVMSS-216)

3) **Post-Crash Phase** - Fire-related .
   (300 Series in FVMSS tests)

   Eg: Fuel System integrity for fire avoidance, (FVMSS-301)

The scope of this project is related solely to the second category, i.e The passive safety phase. More particularly, Full frontal impact, offset frontal impact and 30 degree offset frontal impact on a deformable barrier are the benchmarks that our crash absorber design is mainly concerned with concerned with, Fig. 1.5 illustrates a number of tests criteria.

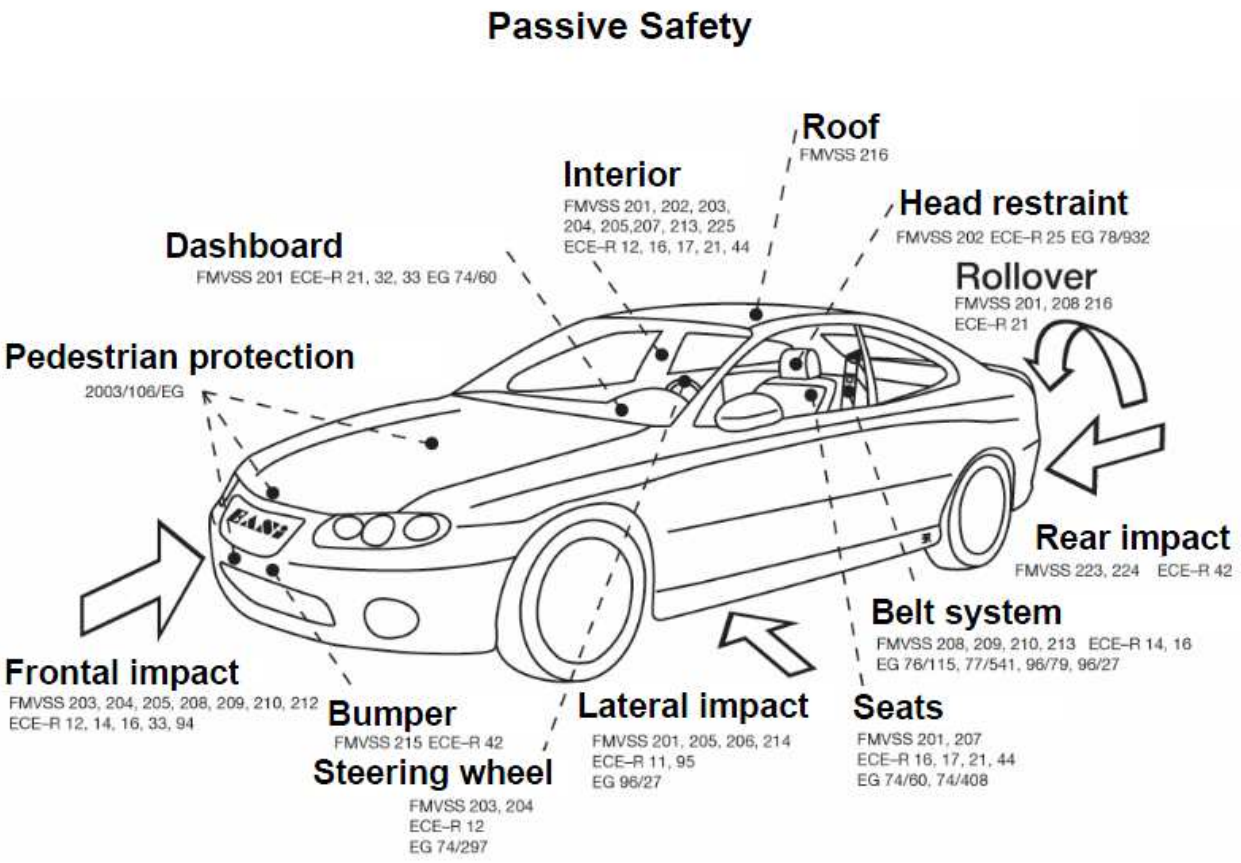

Fig. 1.5 Depiction of different vehicle safety standards.

The FMVSS and ECE tests set a minimum acceptable threshold. These days it is extremely rare that a new production car fails any of these standards. However, the NCAP tests give a rating based on the probability of serious injury. For example, In a 56km/h into a rigid wall frontal impact Less than 10 percent chance of a serious injury (with a 50 percentile male dummy) earns a car a five star frontal impact rating; while 46 percent or greater chance of serious injury earns a car a single star rating. Manufactures constantly strive for higher ratings on this scale.

These crash test procedures and their test speeds (e.g. frontal impact at 56kmph, side impact at a 30 degree angle, etc.) have become the design benchmarks for designers also. Simulations and testing during the design phase is also done at the same criteria. In this work on frontal crash absorbers, the same velocities are used.

Chapter 2. Aims of this project and thesis outline.

2.1 Background of the project

Thin walled beams are widely used as frontal crash absorbers in unit-body automotive chassis design. These beams are specifically designed to absorb high amounts of energy during a crash to ensure passenger cabin integrity and passenger safety. Consequently, a good crash absorber design becomes desirable. Weight reduction is also important for the vehicle performance. Therefore, the collapse modes, buckle wavelengths and optimal triggers are studied and optimized extensively by designers by using impact testing techniques and, more recently, by FEM simulations.

There however remains a huge room for improvement. The demand for lighter and more efficient absorbers is evermore increasing. Furthermore, these beams only work at strictly head-on collisions, even a slight offset is at times enough to send these beams into a global bending mode which absorbs much less energy. Therefore, addition diagonal reinforcements must be added in the form of diagonal beams or sheet metal pan to counter this. This may not be required for the rear crash absorbers because oblique rear impacts is not a testing criterion by regulatory bodies. Fig.2.1 and Fig. 2.2 show the frontal and rear area of a Ferrari F430 chassis with crash absorbers.

Fig.2.2 front crumple zone of a Ferrari F430.

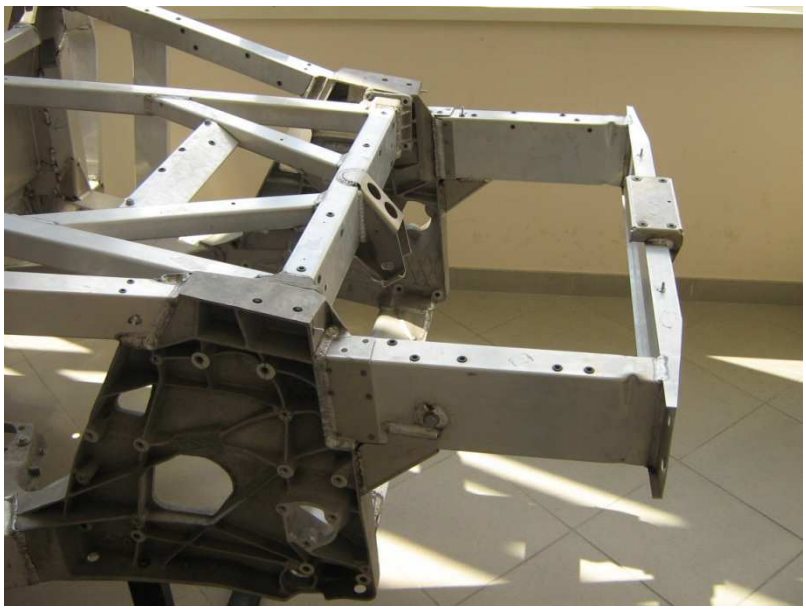

Fig.2.2 Rear crumple zone of a Ferrari F430.

The importance and the need for crash absorbers that perform well in misaligned crashes cannot be overstated. A new and better design was planned in the light of this requirement.

2.2 Aim and methodology

The aim of the project was to design an more efficient crash absorber and make the absorber more resistant to global bending in misaligned crashes. Three main basic optimization areas in crash energy absorbers are listed below.

1) The total energy absorbed during collapse should be maximized per unit weight of the beam.

2) Energy should be dissipated evenly throughout the collapse. Spikes of resistance forces should be avoided as they cause spikes of deceleration that can harm the passengers. An effective trigger is usually used to lower the initial force spike.

3) The design should also be robust against an oblique impact. It should be as resistive as possible to bending or kneeing out in case the impact is slightly misaligned to the beam direction.

A new and novel idea of improving through embedding sinusoidal complex patterns was conceived. These patterns are formed by interference of multiple sinusoidal waves on different axis, the formulation and the details of which will be detailed later in this thesis.

The aim of this project was to study these proposed beams, study them extensively and test them in different conditions through FEM simulations.

The commercial software Altair Hyperworks suite was used to perform all calculations. Details of the FEM modeling and its analytical verification is given in chapter 3.

By the end of this project, a crash absorber design with 42 percent higher energy absorption and 1.6 times more resistance to global bending has been done.

2.2 Thesis layout

The first chapter of the thesis gives a brief overview on the topic of crash safety. It gives a brief historical perspective of the development of crash safety followed by a small outline of the vehicle structure nowadays and the presence of crumple zones. The types of crashes and the requirements of federal car safety regulatory authorities.

Chapter two provides the relevant project background and the specific aims of the project. A small project methodology is also given.

Chapter three provides the state of the art in axial collapse and gives an analytical formulation of the beams. It then goes on to propose frequency induced beams and test their performance in axial collapse through different stages and ends at an optimized solution of a new beam design.

In the fourth chapter, the patterned beams optimized and proposed in chapter three are tested for performances with notch triggers. A new and novel triggering mechanism is proposed with variable frequency progressive triggering.

The fifth chapter tests these beams along with the progressive triggers for performance in oblique, and offset impacts. Different tests are designed to check the performance of SLD beams in oblique impacts.

Conclusions are given separately at the end of each chapter. Formulation for all beams tested are given in Appendix 1.

Chapter 3. Patterned beams in axial collapse

3.1 Introduction and state of the art.

There has been an extensive study of crash absorbers in the past and various authors have contributed to the knowledge reference on crash absorber design.

An approximate theoretical model was firstly proposed by Alexander [1] to predict the mean crushing force and the energy absorption of circular tube under axial crush loading**.** Wierzbicki, Jones, Abramowicz and Kecman [2-8] in their respective studies performed pioneering work in the analytical and FEM modeling of progressive buckling mechanisms of box and circular section beams.

Further contributions were done by YuCheng Liu [9,10] who focused on optimizing the crash absorber shape. Several other authors [11-15] simulated, experimented and analyzed the performance of foam filled sections and proved them to absorb much more energy than hollow sections of similar weight. Xiong Zhang et al. [16] and Heung-Soo Kim [17] proposed multi cellular extruded sections and proved them as even more effective than foam filled sections in axial loading. However, the cross section dimensions of foam filled beams and multi cellular beams are reduced in comparison to hollow beams of similar weigh. Unfortunately, beams with reduced cross-section dimensions are more vulnerable to global bending or kneeing-out during even minutely oblique impacts. Other authors like X. W. Xhang et al. [18] studied the effect of

buckling initiators (triggers) on the overall effectiveness and stability of crash absorber beam collapse.

In a relevant study Daneshi and Hosseinipour [19] conducted experimental tests by adding grooves to circular tubes for axial crash. They concluded that the energy absorption capacity of the tubes was reduced in comparison with the conventional tubes although adding corrugations or grooves could, to some extent, control the energy absorbed by the tubes and improve the uniformity of the load–displacement curves. A similar study of adding grooves on box shaped beams was done by Sunghak Leea et al. [20].

In another study similar to the present work, X. Zhang et. al. [21] added triangular perturbation patterns on the beams and showed them to greatly improve energy absorption during an axial crash using FE analysis. They were able to control the buckle wavelength and reduce it. Double sign wave patterns were proposed by W. Jiang, J.L. Yang [22]. They proved that the buckling could be somehow regularized by inducing a double sign wave but they were not able to increase the dissipated energy value. In his noteworthy recent work, [23], Norman Jones derived an energy efficiency factor. This dimensionless parameter allows comparisons to be made of the energy absorption effectiveness among crash absorbers of various geometrical shapes and materials.

The current work builds further upon this platform of knowledge. An alternative approach is proposed in which complex sinusoidal perturbations are added in the box beam surface to improve energy absorption under compressive axial impacts. Contrary to techniques like foam filled sections and multi cellular sections, adding sinusoidal relief patterns does not require a cross-section reduction to respect an imposed weight.

Recent developments in hydro forming techniques in engineering applications have considerably eased the manufacturing of such patterns using an appropriately shaped die.

The initial aim of this study is to develop perturbation patterns which could control the collapse formation and alter it to form denser collapse wavelengths. The collapse results obtained are compared in terms of both total energy absorption and energy efficiency factor introduced in [23].

3.2 Reference model collapse

3.2.1 Model description.

A standard 100mm*100mm box tube with a wall thickness of 1.7mm was used as a reference specimen.

A load of 500 kilograms was fixed on an axial guiderail perpendicular to the wall. Both the load and the beam were given an initial velocity of 15.6m/s (typical value for NCAP crash tests) and impacted upon a rigid wall.

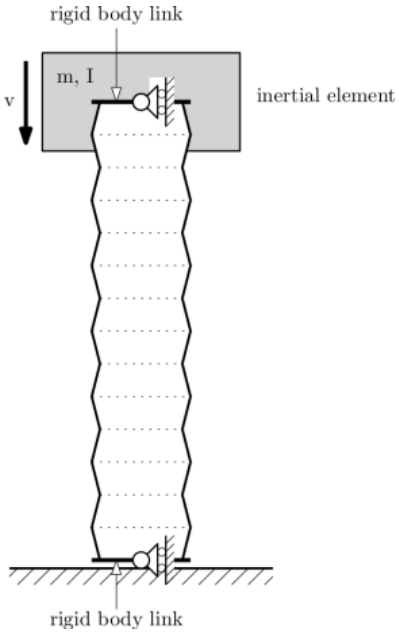

Fig. 3.1. FE model setup.

Both ends on the beam were fixed with an RBE2 link to a central node of each end to simulate a welded plate at both ends as shown in Fig. 3.1. No scheme was employed in the FE model to constrain the global bending and none of the models tested displayed any global bending tendencies.

The cumulative value of the energy absorbed depends on a good design of a trigger, which lowers the initial force spike at the buckle initiation. For beams similar to the reference model, optimized triggers have been investigated by many authors but no such optimized trigger is available for our proposed frequency embedded design. To minimize the effect of the initial peak spike which may falsely raise or lower the total energy absorbed value and hinder us in drawing a good comparison among the designs mentioned in Table 1, a reasonably long beam of 1200 mm was tested. Typical crash absorber length used in cars is about 600 mm.

3.2.2 Material properties

The material properties of Aluminum Alloy AL6260T6, commonly employed for frontal crash absorbers, were used in all simulations. This aluminum alloy has a nominal flow stress of 0.326 GPa, a Young's Modulus of 75 GPa and a rupture strain of 12.8%. However, the purpose of this study is not limited to a specific geometry or material. The Stress Strain curve of AL6260T6 is given in Fig. 3.2

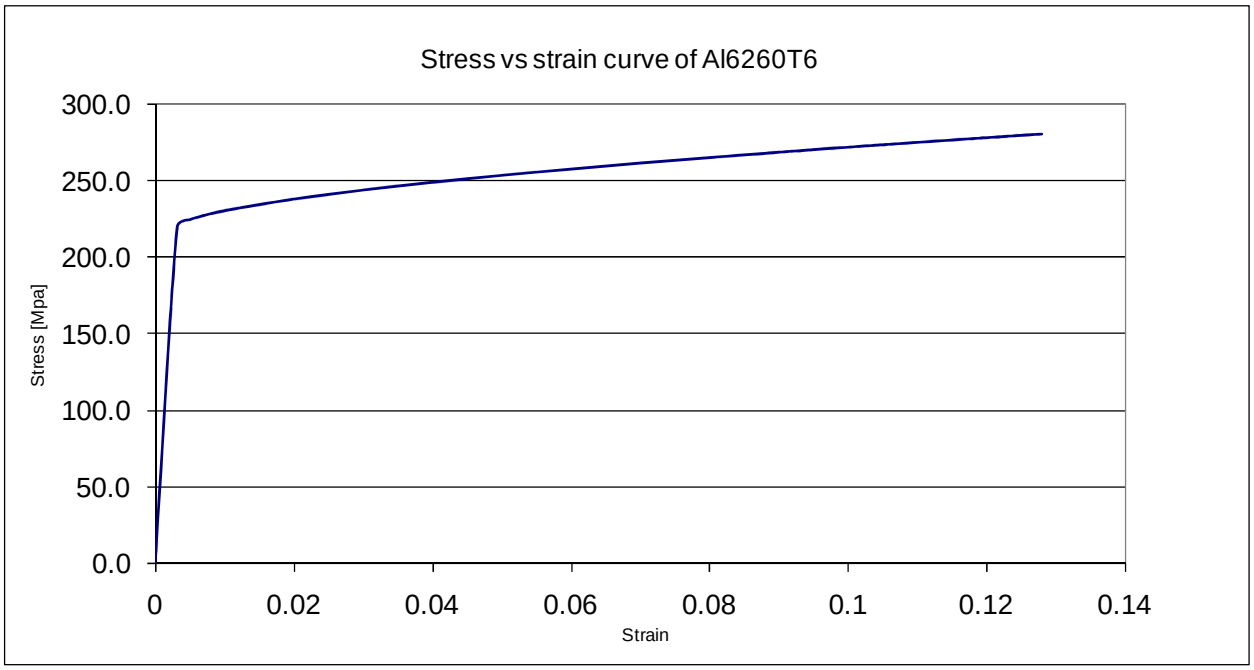

Fig. 3.2. Material properties of Al6260T6

3.2.3 Analytical formulation

Wierzbicki and Abramowicz [4] presented the super folding element in their pioneering work on crash absorbers. Abramowicz and Jones [5,6] further continued this work and derived analytical formulas for each of the distinct collapse modes.

The average collapse force P_m for a box section beam under axial collapse can be approximated by the formula:

$$\frac{P_m}{M_o} = 52.22\left(\frac{C}{H}\right)^{1/3} \qquad (2.1)$$

where *C* is the sectional width and *H* is the wall thickness.

The hinge moment M_o can be given by:

$$M_o = \frac{\sigma_o H^2}{4} \quad (2.2)$$

where σ_o is the flow stress of the material.

If strain hardening effects are also considered, the equivalent flow stress can be calculated by the following formula:

$$\sigma_o = \sqrt{\frac{\sigma_y \sigma_u}{1+n}} \quad (2.3)$$

where σ_y is the yield strength, σ_u is the ultimate tensile strength and *n* is the hardening exponent.

The buckle fold length l, can be predicted as:

$$\frac{l}{H} = 0.99\left(\frac{C}{H}\right)^{2/3} \quad (2.4)$$

These analytical equations were used to calculate the average collapse force of the reference model that is later compared to the numerical simulations for assessment. Since Aluminum is almost strain rate insensitive, these same formulas could be used for both dynamic (uniform-velocity and initial-velocity-and-momentum type) and for quasi static impacts.

Energy efficiency factor is used to benchmark our comparisons against each other. Energy efficiency factor has been firstly defined by N. Jones [23] as:

$$\varphi = \frac{3P_m}{4A\sigma_0 \varepsilon_r} \quad (2.5)$$

where ε_r is the rapture strain of the material and A is the cross-section area.

3.2.4 Finite Element results.

HyperCrash™ was used to set up the model and the RADIOSS™ explicit commercial solver was used for the numerical solutions. These softwares are commonly used for crash analysis applications by automotive industry and researchers. A relatively dense mesh of 5mm size, necessary to correctly mimic the proposed sinusoidal perturbations (visible in Fig. 3.4.), was employed.

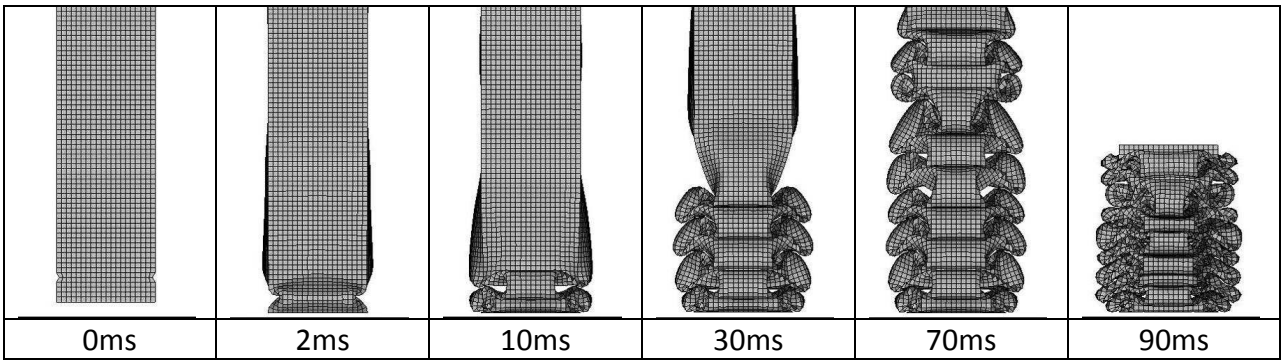

Fig. 3.3. Reference model typical collapse behavior.

It can be observed in the collapse showed in Fig. 3.3 that the buckle does not strictly adhere to a constant deformation wavelength. After the initiation phase, the progressive buckles settle into a more regular, approximately constant pattern. A good trigger is necessary in ensuring a stable initial collapse.

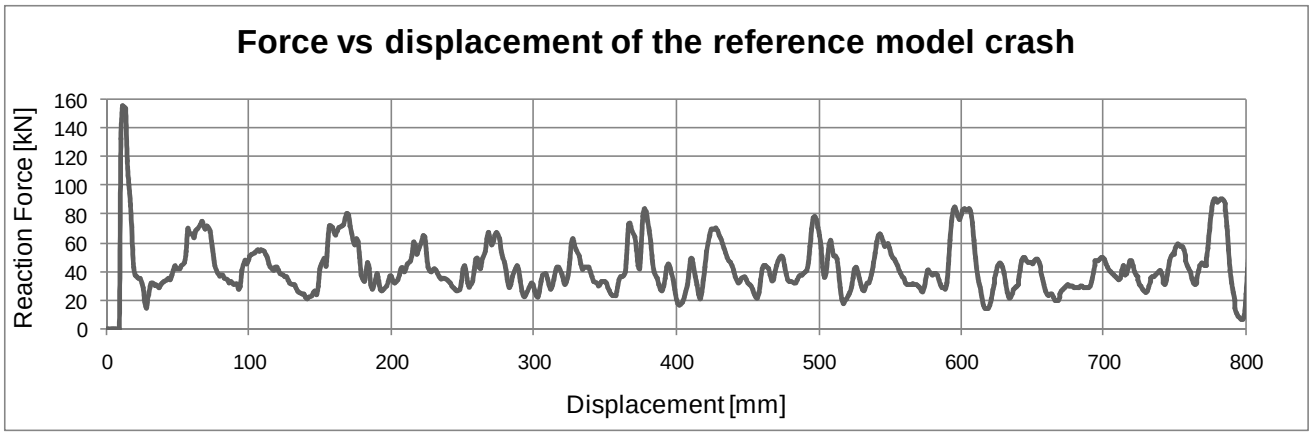

Fig. 3.4. Reaction force Vs displacement for reference model.

Fig. 3.4 shows a high initial force peak followed by low intermittent peaks during the folding process. In a preferred mode of collapse, the initial force peak could be lowered to reduce the deceleration jolt, whereas the subsequent peaks could be raised in order to absorb more energy.

An average force value of 41.83 kN obtained from the numerical computations compares reasonably with an analytical prediction of 47.84 kN calculated using equations 2.1 - 2.3. The numerical average force taken form FE results is calculated ignoring the initial force spike and the ending buckle condensation. The average free form buckle length l was found to be 29.5mm in the FE predictions versus a calculated length of 25.4mm using Equation 2.4. The energy efficiency Factor for the Reference model using Equation 2.5 is 1.08.

3.3 Proposed frequency Induced models

Initially, several types of pattern formations were proposed. Different combinations of trigonometric formulas were used in both the axes along the surface to achieve the desirable surface perturbations. Fig. 3.5a to Fig3.5e show the relative shapes of some of these perturbations along with a sample formulation. Type TR patterns are similar to those tested by W. Jiang, J.L. Yang [22] in their research, while the other pattern types A, B, SA, SLO, SL are not traceable in the pertinent literature.

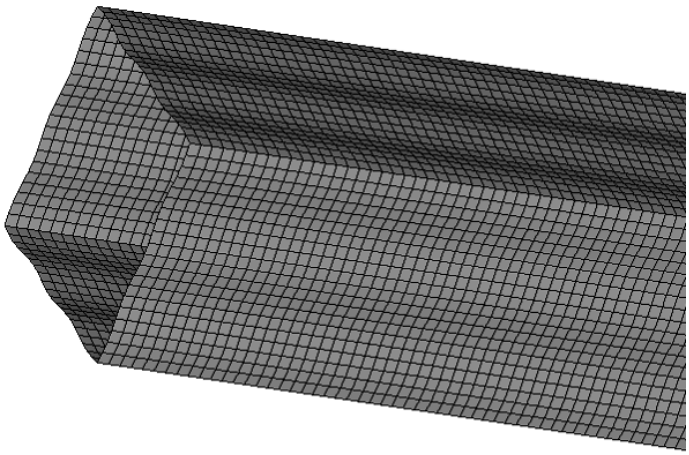

Fig. 3.5a. Type A pattern.

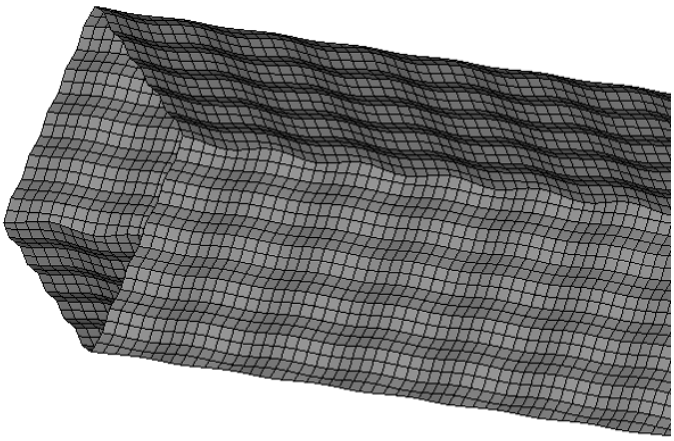

Fig. 3.5b. Type TR pattern.

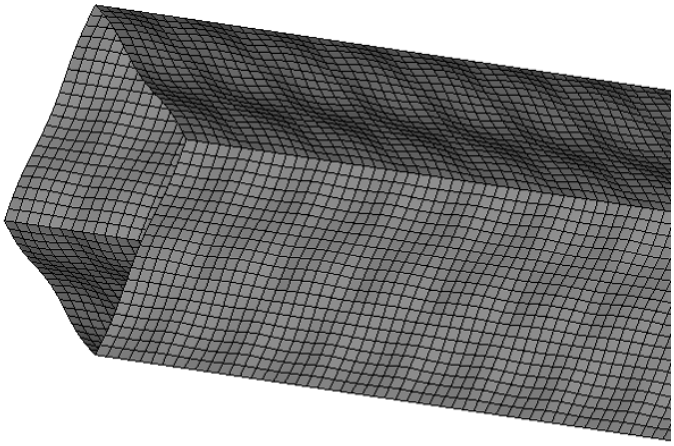

Fig. 3.5c. Type SA pattern.

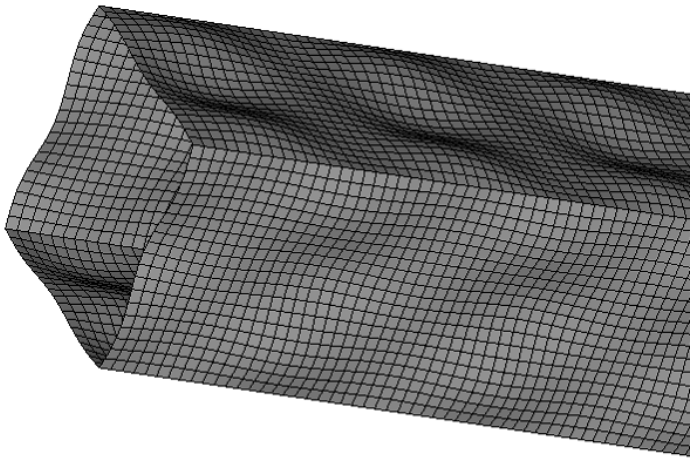

Fig. 3.5d. Type SLO pattern.

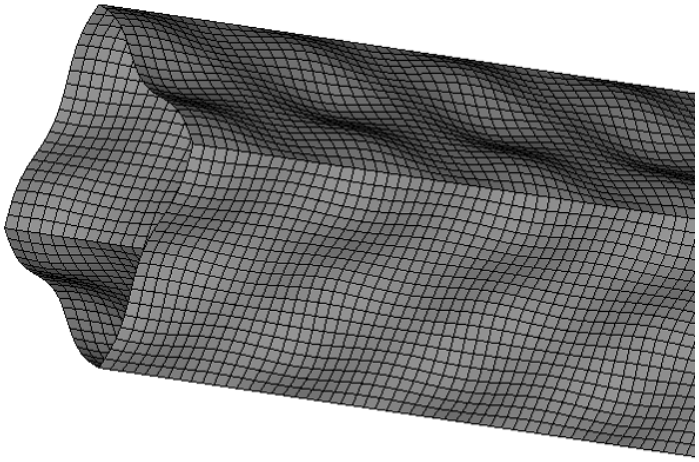

Fig. 3.5e. Type SL pattern.

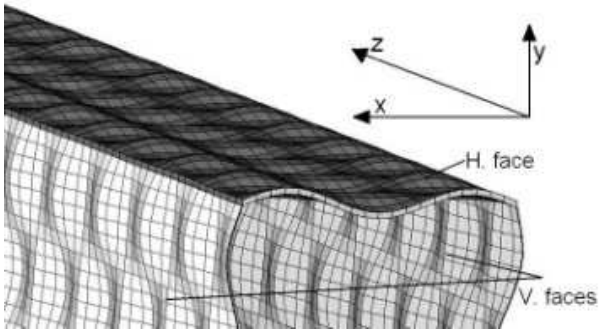

Fig. 3.6. Coordinate system for mathematical expressions

A global coordinate system shown in Fig. 3.6 with the origin at the center of the beam was used for the mathematical expressions listed in Table 1.

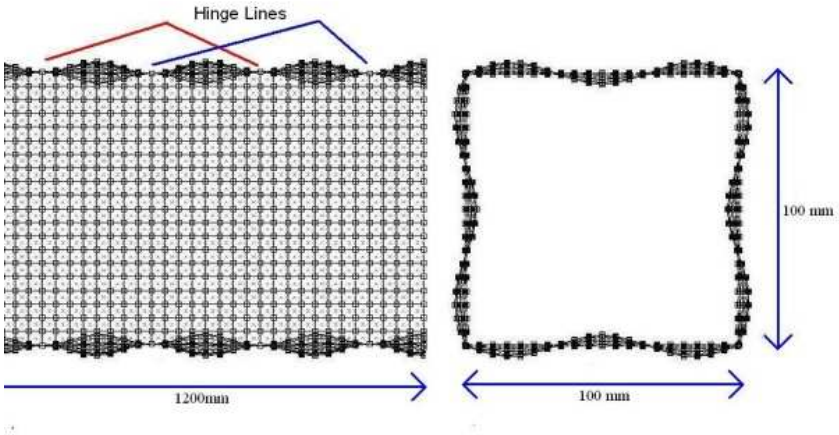

Fig. 3.7. Nodal hinges in SL and SLD type patterns.

Some perturbation types have distinct flat zones or nodes which could act as hinges while collapsing, while other perturbation types do not. Fig. 3.7. illustrates SL type patterns that have distinct nodal hinges.

Table 3.1 illustrates a list of trigonometric formulas used to create the complex perturbations on the beam surfaces along with the pattern nomenclature.

Name	Nodal line spacing	Formula Horizontal Wall	Formula Vertical Wall
A1	NA	-50-(cos(y*π/20))	-50-(cos(y*π/20))
B1	10	-50-(cos(z*π/20))	50+(cos(z*π/20))
B2	15	-50-(cos(z*π/30))	50+(cos(z*π/30))
TR1	NA	50+(cos(((z/1.5)+y)*π/20))*cos(((z/1.5)-y)*π/20)+ cos(y*π/20)	50+(cos(((z/1.5)+y)*π/20))*cos(((z/1.5)-y)*π/20)+cos(y*π/20)
ZE1	NA	50+(sin(((z/2)+y)*π/20))*sin(((z/2)-y)*π/20)*2	50+(cos(((z/2)+y)*π/20))*cos(((z/2)-y)*π/20)*2

ZE2	NA	-50-(cos(((z/1.5)+y)*π/20))*cos(((z/1.5)-y)*π/20)	-50-(cos(((z/1.5)+y)*π/20))*cos(((z/1.5)-y)*π/20)
OB1	NA	50+(sin((z+x)*π/20))*sin((z-x)*π/20)	50+(sin((z+y)*π/20))*sin((z-y)*π/20)
V1	40	-50+(cos(z*π/20))*cos(x*π/20)/2	-50+(cos(z*π/20))*cos(y*π/20)/2
V2	40	-50+(-cos(z*π/20))*cos(x*π/20)/2	-50+(cos(z*π/20))*cos(y*π/20)/2
V3	20	-50+(-cos(z*π/20))*cos(x*π/20)/2-(cos(z*π/20))/2	-50+(-cos(z*π/20))*cos(y*π/20)/2-(cos(z*π/20))/2
V4	20	-50+(cos(z*π/10))*cos(x*π/20)/2	-50+(cos(z*π/10))*cos(y*π/20)/2
V5	40	50+(cos(z*π/60))*cos(x*π/20)	50+(cos(z*π/60))*cos(x*π/20)
V6	40	50+(cos(z*π/40))*cos(x*π/20)	50+(cos(z*π/40))*cos(x*π/20)
SA1	50	50-cos(x*π/33.33)*abs(cos(z*π/50))*2	50-cos(y*π/33.33)*abs(cos(z*π/50))*2
SA2	40	50-cos(x*π/33.33)*abs(cos(z*π/40))*2	50-cos(y*π/33.33)*abs(cos(z*π/40))*2
SA3	35	50-cos(x*π/33.33)*abs(cos(z*π/35))*2	50-cos(y*π/33.33)*abs(cos(z*π/35))*2
SA4	90	50-cos(x*π/33.33)*abs(cos(z*π/90))*2	50-cos(y*π/33.33)*abs(cos(z*π/90))*2
SLO1	90	50-cos(x*π/33.33)*((cos((z+0)*π/45))+1)*2	50-cos(y*π/33.33)*((cos((z+45)*π/45))+1)*2
SL2	70	50-cos(x*π/33.33)*((cos((z+35)*π/35))+1)*2	50-cos(y*π/33.33)*((cos((z+0)*π/35))+1)*2
SL3	70	50-cos(x*π/33.33)*((cos((z+0)*π/35))+1)*2	50-cos(y*π/33.33)*((cos((z+0)*π/35))+1)*2
SL4	50	50-cos(x*π/33.33)*((cos((z+0)*π/25))+1)*2	50-cos(y*π/33.33)*((cos((z+0)*π/25))+1)*2

SL5	60	50-cos(x*π/33.33)*((cos((z+0)*π/30))+1)*2	50-cos(y*π/33.33)*((cos((z+0)*π/30))+1)*2
SL6	40	50-cos(x*π/33.33)*((cos((z+0)*π/20))+1)*2	50-cos(y*π/33.33)*((cos((z+0)*π/20))+1)*2
SLD1	40	50-(cos(x*π/33.33)*((cos((z+0)*π/20))+1)*2)+((sin(z*π/40))*.3)	50-(cos(y*π/33.33)*((cos((z+0)*π/20))+1)*2)-((sin(z*π/40))*.3)
SLD2	40	50-(cos(x*π/33.33)*((cos((z+0)*π/20))+1)*2)+((sin(z*π/40))*.15)	50-(cos(y*π/33.33)*((cos((z+0)*π/20))+1)*2)-((sin(z*π/40))*.15)
SLD3	34	50-(cos(x*π/33.33)*((cos((z+0)*π/17))+1)*2)+((sin(z*π/34))*.15)	50-(cos(y*π/33.33)*((cos((z+0)*π/17))+1)*2)-((sin(z*π/34))*.15)
SLD4	30	50-(cos(x*π/33.33)*((cos((z+0)*π/15))+1)*2)+((sin(z*π/30))*.15)	50-(cos(y*π/33.33)*((cos((z+0)*π/15))+1)*2)-((sin(z*π/30))*.15)
SLD5	34	50-(cos(x*π/33.33)*((cos((z+0)*π/17))+1)*2)+((sin(z*π/34))*.3)	50-(cos(y*π/33.33)*((cos((z+0)*π/17))+1)*2)-((sin(z*π/34))*.3)
SLD6	34	50-(cos(x*π/20)*((cos((z+0)*π/17))+1)*2)+((sin(z*π/34))*.3)	50-(cos(y*π/20)*((cos((z+0)*π/17))+1)*2)-((sin(z*π/34))*.3)

SLD7	34	50- (cos(x*π/20)*((cos((z+0)*π/17))+1)*2)+ ((sin(z*π/34))*.3)	50+(cos(y*π/20)*((cos((z+0)*π/17))+1) *2)-((sin(z*π/34))*.3)
SLD8	34	50+(cos(x*π/20)*((cos((z+0)*π/17))+1) *2)+ ((sin(z*π/34))*.3)	50+(cos(y*π/20)*((cos((z+0)*π/17))+1) *2)-((sin(z*π/34))*.3)
SLD9	34	50- cos(y*π/33.33)*((cos((z+0)*π/34))+0)* 2+ ((sin(z*π/34))*.3)	50- cos(y*π/33.33)*((cos((z+0)*π/34))+0)* 2- ((sin(z*π/34))*.3)
SLD10	30	50+(cos(x*π/20)*((cos((z+0)*π/15))+1) *2)+ ((sin(z*π/30))*.3)	50+(cos(y*π/20)*((cos((z+0)*π/15))+1) *2)-((sin(z*π/30))*.3)
SLD11	30	50+(cos(x*π/20)*((cos((z+0)*π/15))+1) *2)+ ((sin(z*π/30))*.15)	50+(cos(y*π/20)*((cos((z+0)*π/15))+1) *2)-((sin(z*π/30))*.15)
SLD12	26	50+(cos(x*π/20)*((cos((z+0)*π/13))+1) *2)+ ((sin(z*π/26))*.3)	50+(cos(y*π/20)*((cos((z+0)*π/13))+1) *2)-((sin(z*π/26))*.3)
SLD13	26	50- (cos(x*π/14.2857)*((cos((z+0)*π/13))+ 1)*2)+ ((sin(z*π/26))*.3)	50- (cos(y*π/14.2857)*((cos((z+0)*π/13))+ 1)*2)-((sin(z*π/26))*.3)
SLD14	20	50- (cos(x*π/14.2857)*((cos((z+0)*π/10))+ 1)*2)+ ((sin(z*π/20))*.3)	50- (cos(y*π/14.2857)*((cos((z+0)*π/10))+ 1)*2)-((sin(z*π/20))*.3)
SLD15	26	50-	50-

		(cos(x*π/14.2857)*((cos((z+0)*π/13))+1)*2)+ ((sin(z*π/26))*.15)	(cos(y*π/14.2857)*((cos((z+0)*π/13))+1)*2)-((sin(z*π/26))*.15)
SLD16	26	50-(cos(x*π/14.2857)*((cos((z+0)*π/13))+1)*2)+ ((sin(z*π/26))*.1)	50-(cos(y*π/14.2857)*((cos((z+0)*π/13))+1)*2)-((sin(z*π/26))*.1)
SLD17	26	50-(cos(x*π/14.2857)*((cos((z+0)*π/13))+1)*1)+ ((sin(z*π/26))*.1)	50-(cos(y*π/14.2857)*((cos((z+0)*π/13))+1)*1)-((sin(z*π/26))*.1)
SLD18	26	50-(cos(x*π/14.2857)*((cos((z+0)*π/13))+1)*1)+ ((sin(z*π/26))*.3)	50-(cos(y*π/14.2857)*((cos((z+0)*π/13))+1)*1)-((sin(z*π/26))*.3)
SLD19	30	50+(cos(x*π/20)*((cos((z+0)*π/15))+1)*1)+ ((sin(z*π/30))*.3)	50+(cos(y*π/20)*((cos((z+0)*π/15))+1)*1)-((sin(z*π/30))*.3)

Table 3.1. Section formulas.

3.3.1 Selected FE results at stage 1

From the initial tests results shown in Fig. 3.8, it appeared that buckling behavior could be controlled through embedding frequencies. The A and B series only have a single directional perturbation frequency. Interestingly, in case of A type patterns (longitudinal wave) the buckling got more erratic and the mean wave length increased. In the B type patterns (traverse wave) the buckling was controllable and its wavelength was reduced, but it still absorbed less energy than the reference model.

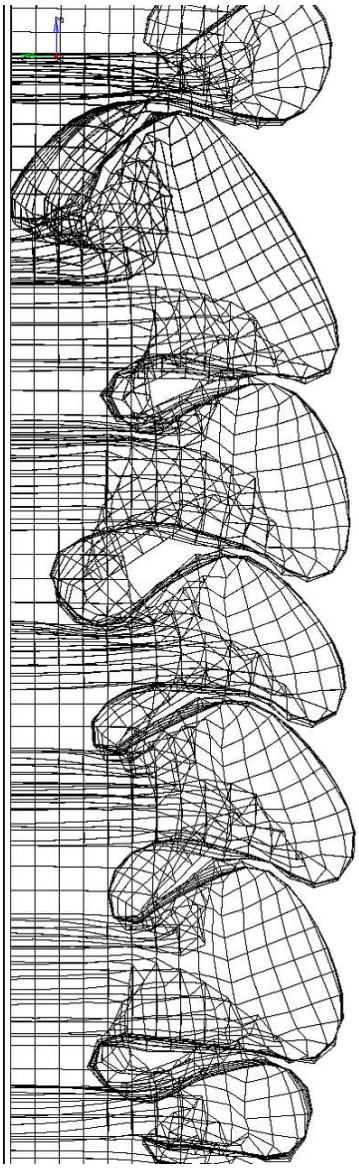

Fig. 3.8a Reference,

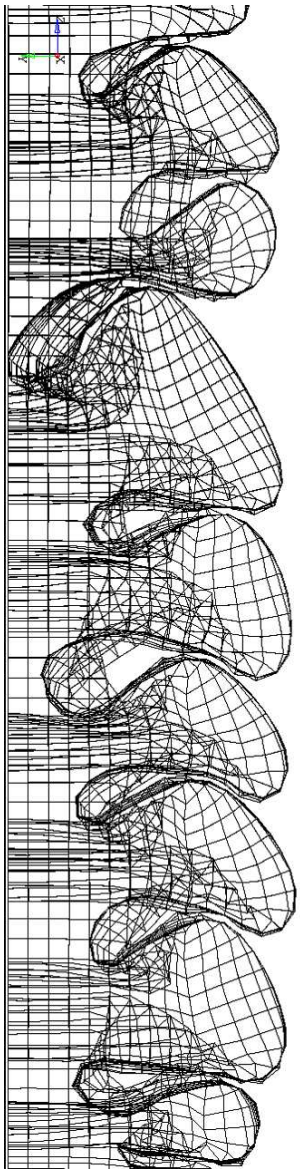

Fig. 3.8b A1

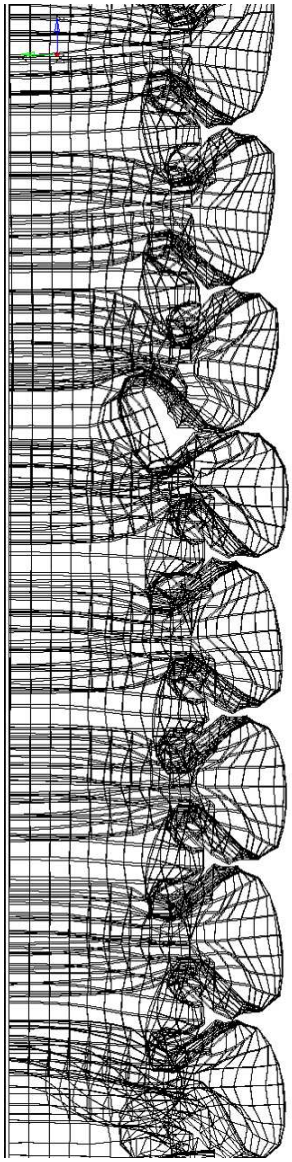

Fig. 3.8c B1

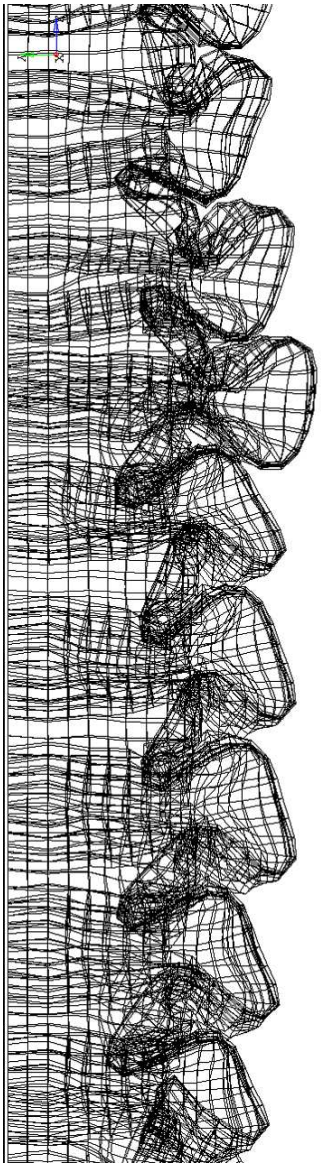

Fig. 3.8d TR1

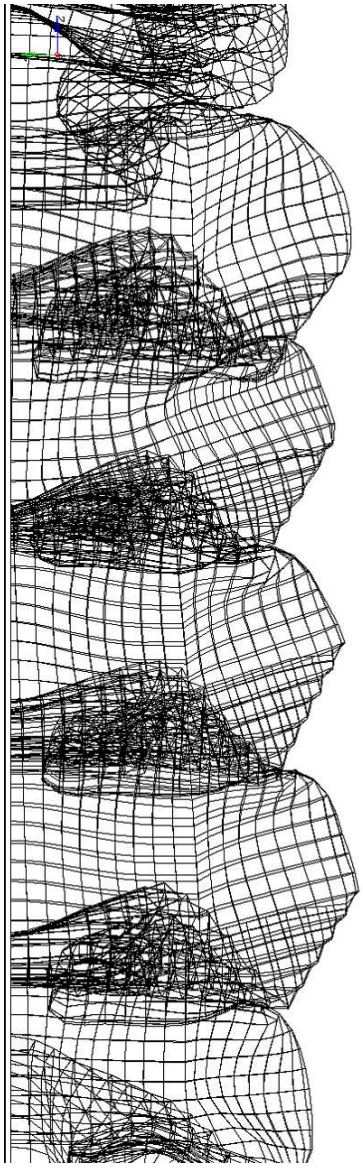

Fig. 3.8e SLO1

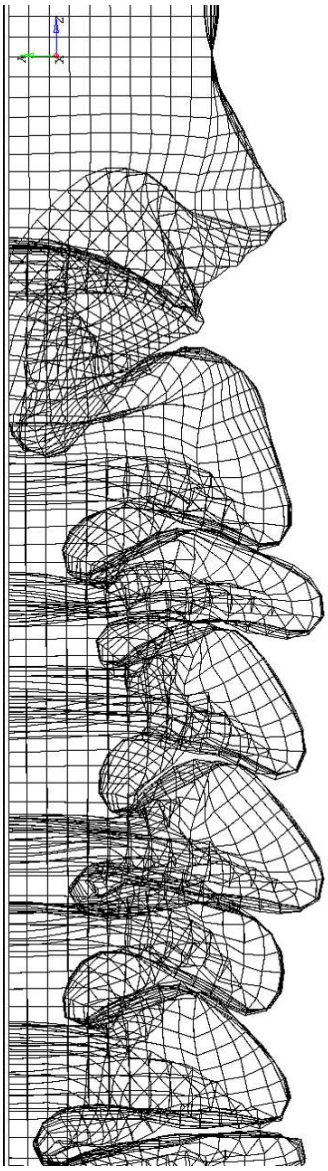

Fig. 3.8f SA3

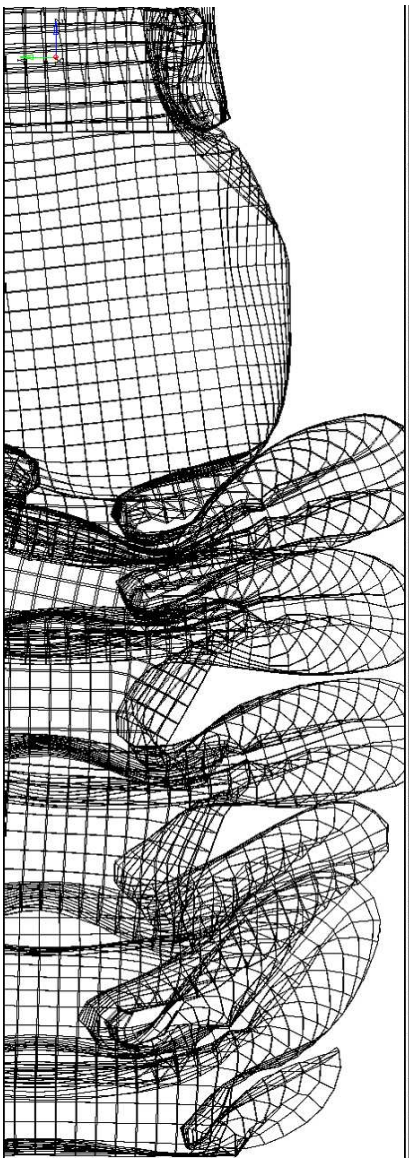

Fig. 3.8g SA4

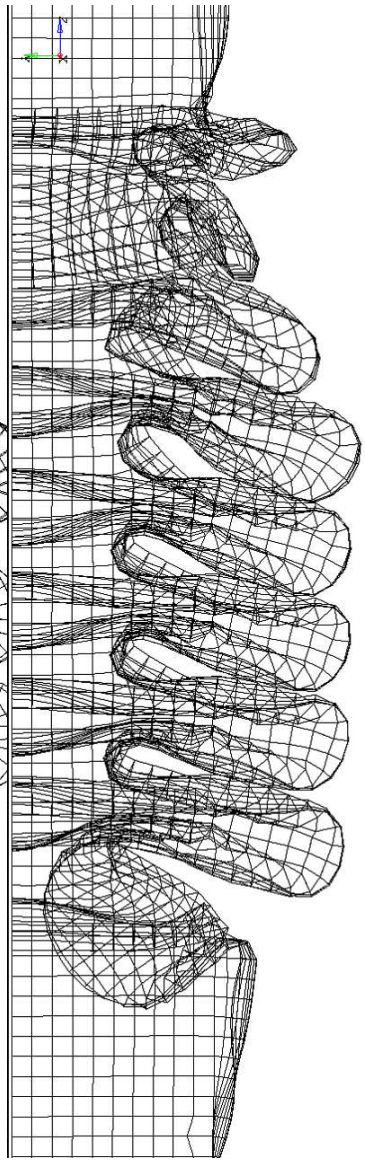

Fig. 3.8h SL3

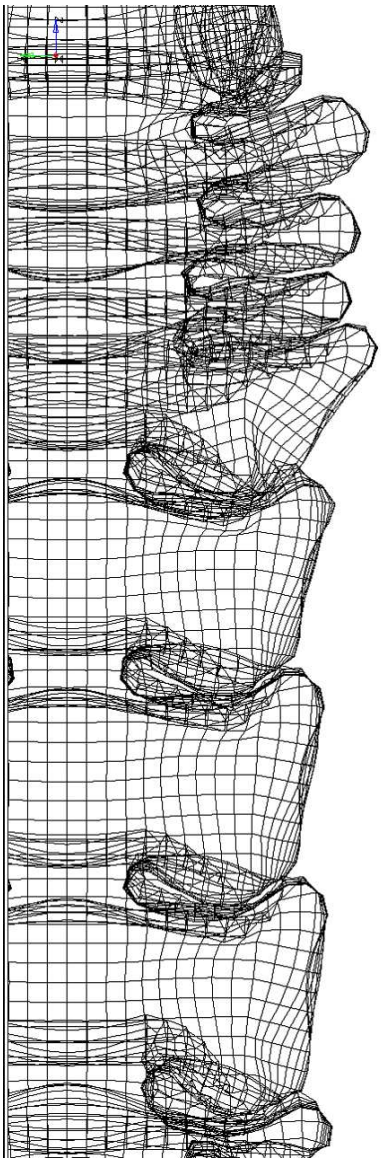

Fig. 3.8i SL4

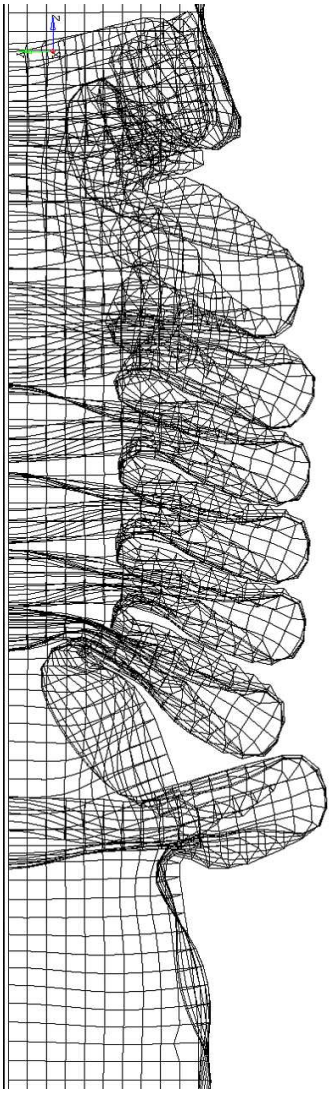

Fig. 3.8j SL5

The SL series and the TR series produced the most regular patterns. Buckling always initiated on the longitudinal nodal hinges if the perturbation amplitude was reasonably high. Ideally, if one nodal hinge folds outwards, its adjacent line should fold inwards. This however, did not always happen, as it can be seen in SL4 where two adjacent nodal hinges buckled together outwards or inwards.

The energy absorption did not show any improvement in any of these models tested.

3.4 Optimization criteria

It may be predicted that denser patterns absorb higher energy while collapsing. This assumption was referenced on the work of previous authors such as Wierzbicki and Abramowicz [2,3] who quantitatively associated closer hinge lines or denser buckles to a higher energy absorption.

A quantitative optimization based on cumulative energy absorption or reaction force values was difficult to carry out due to the variety of samples tested and the gross fluctuations of the force and energy values with respect to small variations in frequencies. The following optimization method was therefore adopted.

Stage one.

A variety of frequency perturbations were tested initially. The types of perturbations which tended to produce the most regular buckles after impact were identified.

Stage two.

The collapse behavior of selected designs at stage one were further studied. Various geometric parameters such as primary longitudinal wave amplitude, primary transverse wave amplitude, transverse wave frequency, phase difference between vertical and horizontal faces and phase difference between opposing faces was tweaked and manipulated to obtain the most regular collapse buckle formations.

Stage three.

In the designs in which the buckling deformation adhered well to the hinge lines, the longitudinal wave wavelength was systematically reduced, while tweaking other parameters to keep the buckle formation regular. The aim of this stage was to obtain the densest regular collapse mode possible.

3.5 SLD Series

The SLD Series was developed to counter the issue of multiple hinges per fold as experienced with the SL type patterns. In the SLD series a third frequency was added with a very light

amplitude (<0.3 mm), so that successive nodal hinges either pointed inwards or outwards as shown in Fig. 3.9. Adjacent nodal hinges had a slight preset tendency to bend either inwards and outwards respectively (higher and lower nodal lines). Nodal hinges on adjacent walls were preset with a phase offset to accommodate for asymmetric bending mode.

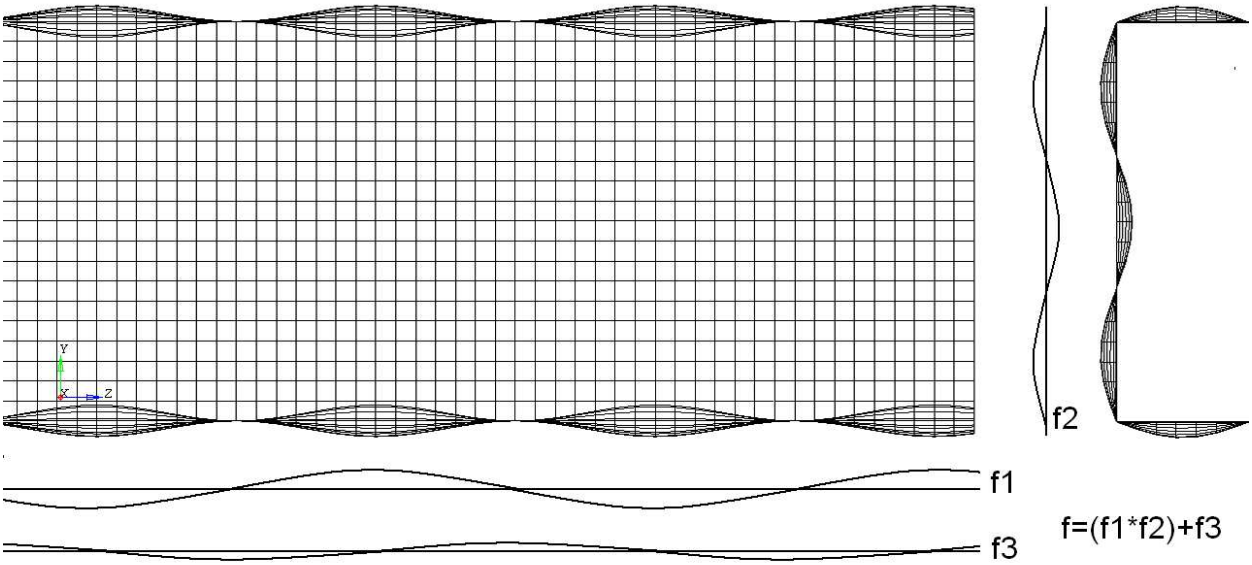

Fig. 3.9 SLD series diagram

3.5.1 Selected results of SLD Series

A total of 19 iterations of SLD type patterns were modeled in Hyper Crash™ and simulated in RADIOSS™. The crash behavior of SLD Type patterns is shown in Fig. 10b to Fig10e in comparison with the base model Fig10a.

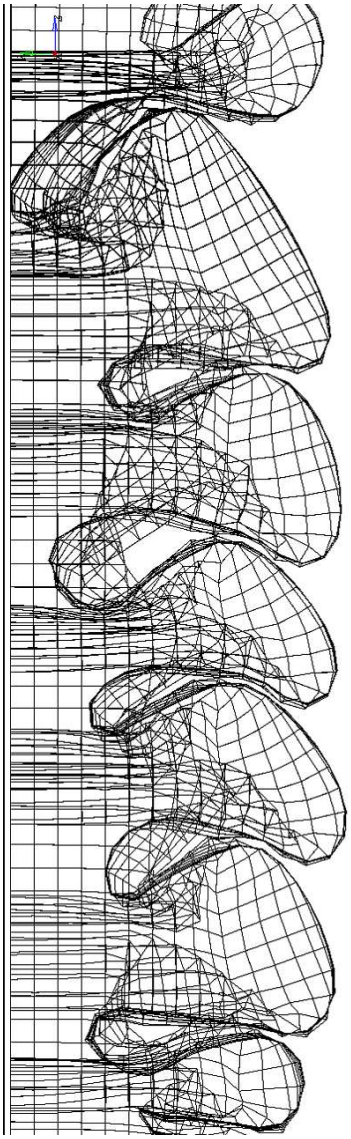

Fig. 3.10a Reference

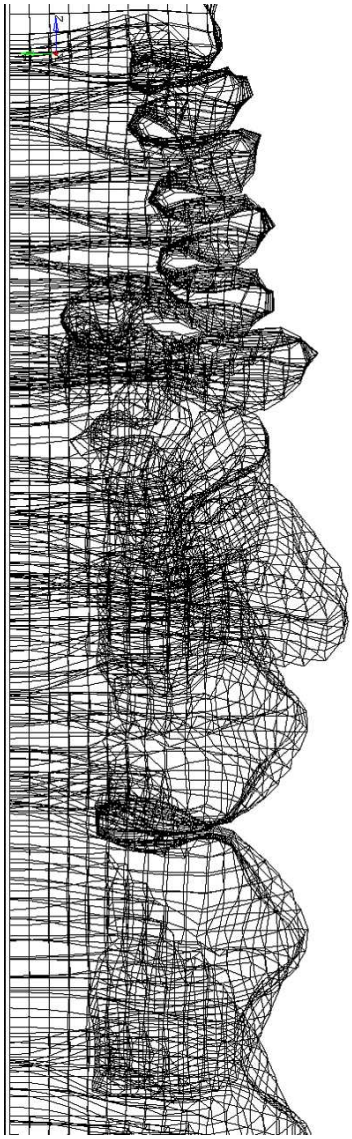

Fig. 3.10b SLD3

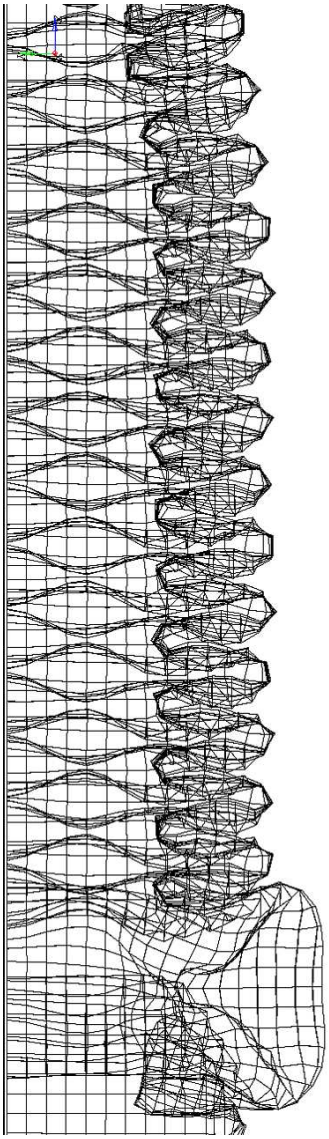

Fig. 3.10c SLD8

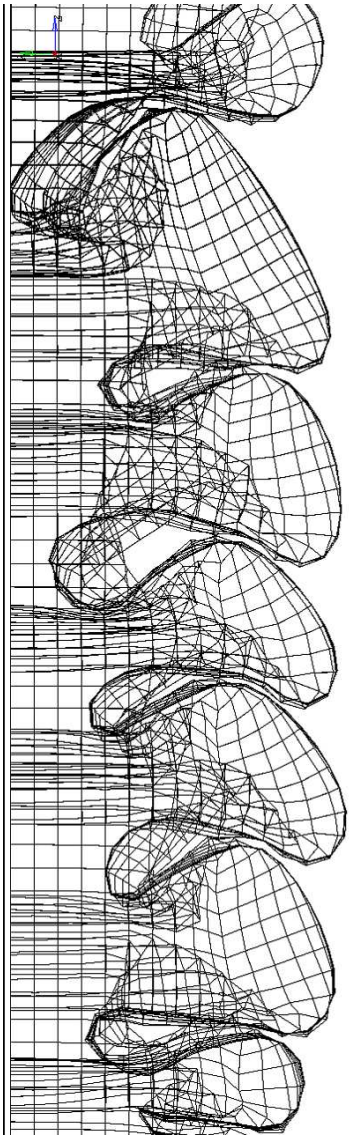

Fig. 3.10a Reference

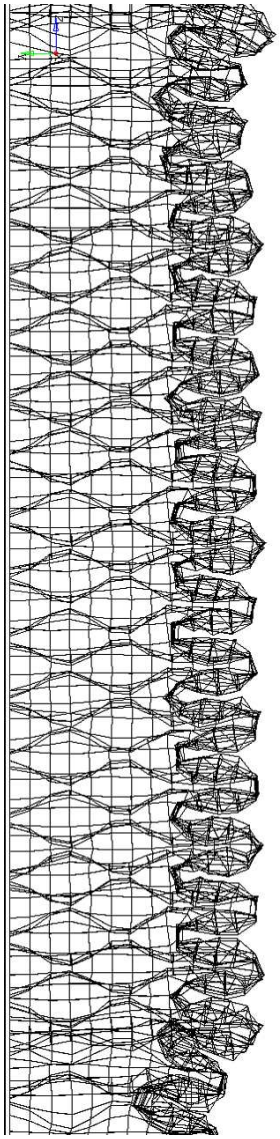

Fig. 3.10d SLD13

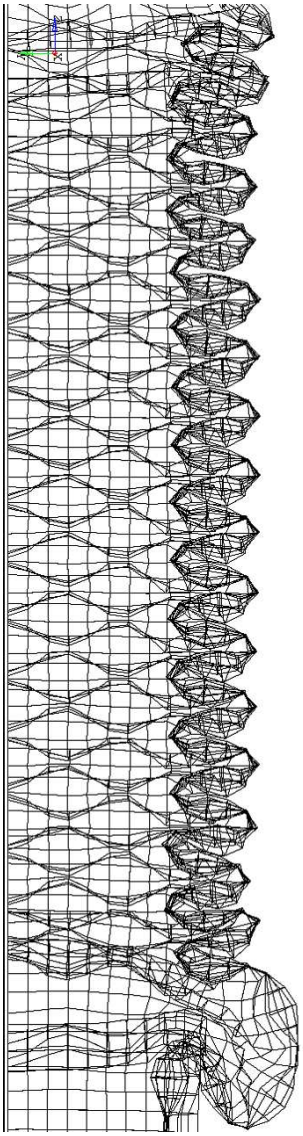

Fig. 3.10e SLD13

The initially proposed patterns exhibited a certain controllable, but not perfect behavior as it can be observed from Fig.10. For example, in SLD3 [Fig. 3.10b] the buckles initiated properly but then they fell out of sync later on. More refined iterations like SLD8, and SLD 13 [Fig. 3.10d and Fig. 3.10(e) were able to remain stable; SLD16 is the most optimized and stable pattern achieved so far. A summary of the results for the energy absorption E, the average collapse force P_m and the energy efficient factor φ for selected beams is collected in Table 3.2.

Name	E (900mm)	P_m (at 900mm)	φ	%age Inc. in E & φ
	k Joules	k Newton		
REFERENCE	36.86	40.95	1.08	0.00
SLD8	38.42	42.69	1.13	4.25
SLD10	43.53	48.37	1.28	18.11
SLD12	48.17	53.52	1.41	30.68
SLD13	50.16	55.73	1.47	36.09
SLD11	43.60	48.45	1.28	18.30
SLD14	47.76	53.06	1.40	29.57
SLD16	52.43	58.26	1.54	42.27

Table 3.2. Internal energy and energy efficiency factor of various designs.

The Internal energy graphs for the models listed in Table 2 are grouped in Fig. 3.11. Typical force vs. distance curves for two different SLD beams are shown in comparison with the reference beam in Fig. 3.12. SLD16 shows 42.27% increase in energy dissipation as compared to the reference model.

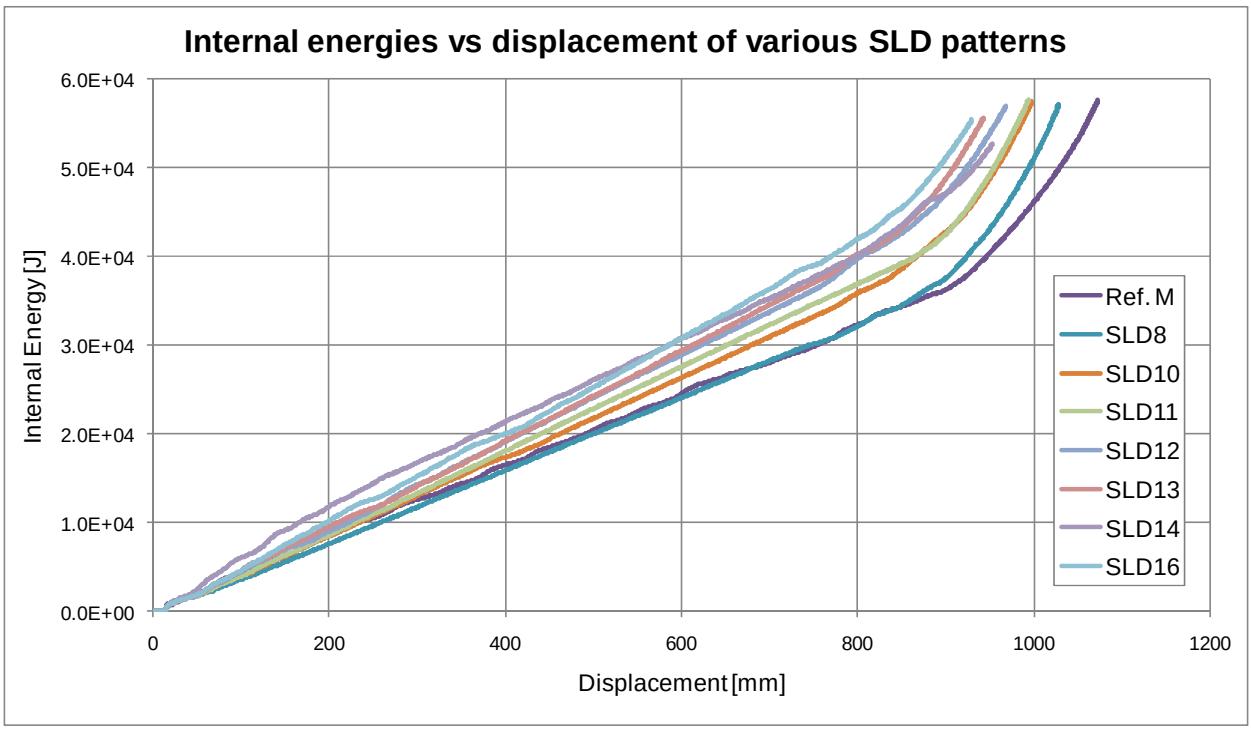

Fig. 3.11. Internal Energy vs. displacement of various designs in comparison to the reference model.

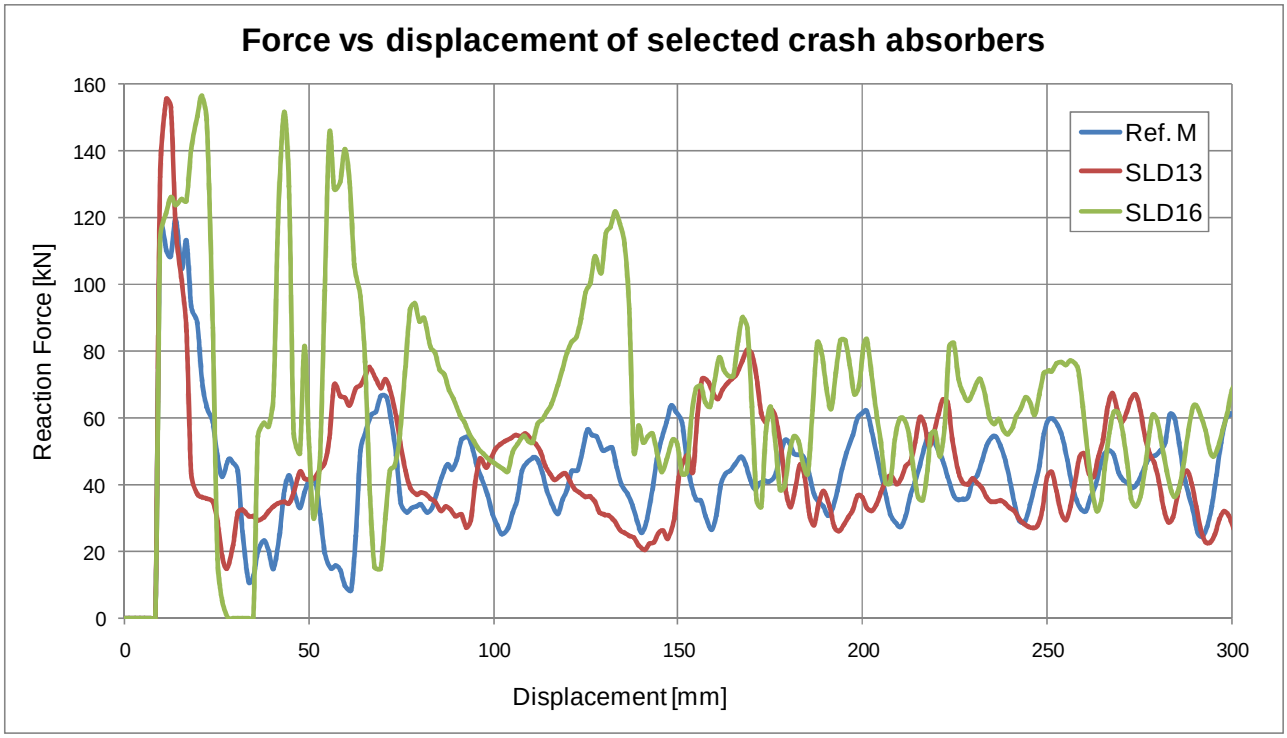

Fig. 3.12. Reaction Force vs. displacement in comparison to the reference model.

3.6 Conclusions.

Several types of sinusoidal patterns were embedded in the box beam surface and their performance as crash absorbers was assessed. Some frequency embedded beams displayed denser folds and more regular buckles than others. They also displayed great improvement in energy absorption.

It was observed that it is possible to alter the crash modes and buckle frequency by introducing patterns with nodal hinges and undulations, whereas patterns that did not have distinct nodal hinges did not improve or control buckle wavelength effectively. In the patterns with nodal hinges, the force peaks could be controlled by manipulating the longitudinal and horizontal wave amplitude. A sufficient amplitude also enabled the nodal line wavelength to be reduced.

The best results were achieved with the SLD type patterns. It was possible to reduce the buckling wavelength and lower it significantly from original freeform value. In the most optimized results of this series, the energy absorption was increased by more than 42% of the reference value. Similarly, the energy efficiency was improved from 1.08 of the reference model to 1.54 is the most optimized design.

Chapter 4. Trigger Design

4.1 Introduction and state of the art.

In the previous chapter, the focus was kept on studying the pattern formation and arbitrary, or where possible, no triggers were used in the FEM calculations. Neglecting the effect of triggers was possible because very long beams were simulated to obtain a good averaged out force value and the impact was perfectly perpendicular to the wall.

In real cases, however, triggers or buckling initiators are necessary for initiating a controllable collapse behavior. A beam without a suitable trigger could be vulnerable to global bending, and irregular buckling in crash.

Triggers or buckling initiators are designed to serve the following purposes.

1. The Initial force spike during the beginning of the collapse should be lowered.
2. The buckling has to start at a desired location (preferably close to the frontal tip) and nowhere else. This is extremely important in order to prevent kneeing out and global buckling during misaligned crashes.
3. Buckling must commence into a subsequent regular and stable collapse mode.

Previously, authors like X.W. Zhang, H. Su, T.X. Yu [24] have focused on designing novel triggering mechanisms using a pre-hit column and pulling strips for initiation. Recep Gumruk, S Karadeniz [25] studied bump type triggers on top hat, rectangular cross-sections through numerical studies and showed that the crush response also varied greatly with the placement and the size of the trigger. An experimental study on cross sections with triggers was also done by Minoru Yamashita, et. al. [26] Yong-Bum Cho [27] carried out numerical studies on hole and dent triggers to optimize the dent geometry and positioning of triggers.

However, all studies on triggers or buckling initiators have been done on plain surface beams. The viability of such triggers on pattern embedded beams such as those mentioned in the previous chapter has not been previously tested. In patterned beams, folding only initiates on predetermined hinge lines rather than anywhere. Therefore the use of the same triggering mechanism used for plain surface beams may not be as effective.

In the first part of this chapter, the effectiveness of using conventional notch type triggers for patterned beams mentioned the previous chapter two is tested.

In the second part, an alternate triggering mechanism for the patterned beams has been proposed in which the sinusoidal pattern formulation is slightly altered along the length of the beam to make certain zones more predisposed towards a collapse. Since it's a continuous variation in pattern rather than a point base trigger, progressively triggered beams are more robust towards forming unwanted stray deformations elsewhere along the length of the beam during collapse. This property is especially useful in the performance of impact absorbers during oblique impacts where globalized bending or kneeing-out is a common failure mode.

4.2 Notch type triggers in reference model

An FEM study was performed using the commercial pre-processor HyperCrash™ and the commercial explicit FEM solver RADIOSS™ to test the hypothesis. Patterned beams with notch type triggers were simulated for frontal impacts and analyzed. The proposed progressive triggers were studied comprehensively for frontal impacts in the second part of this chapter. Lastly, The proposed design was tested for oblique impact and off centered mass impact and compared against patterned beams with notch trigger and a plain reference beam.

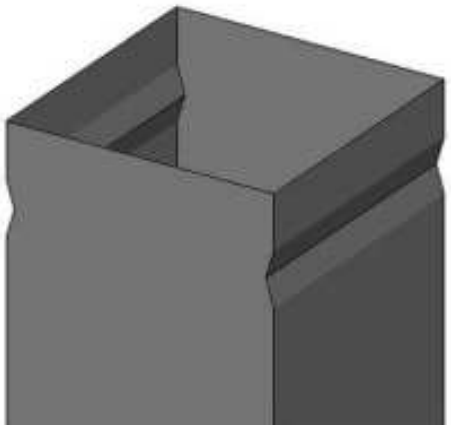

Fig. 4.1. Notch trigger on a crash absorber

Notches are commonly used as triggers for box beam sections to effectively initiate buckling. They can be added on all four sides or two opposing sides. Fig. 4.1 shows the depiction of a notch type trigger with notches on two opposing sides.

A comparison of force-displacement diagram between the first 200mm of a trigger less reference beam collapse and a well triggered beam collapse is shown in Fig. 4.2. A desired lower initial peak for the triggered beam is observed while the rest of the graph follows roughly the same average force value.

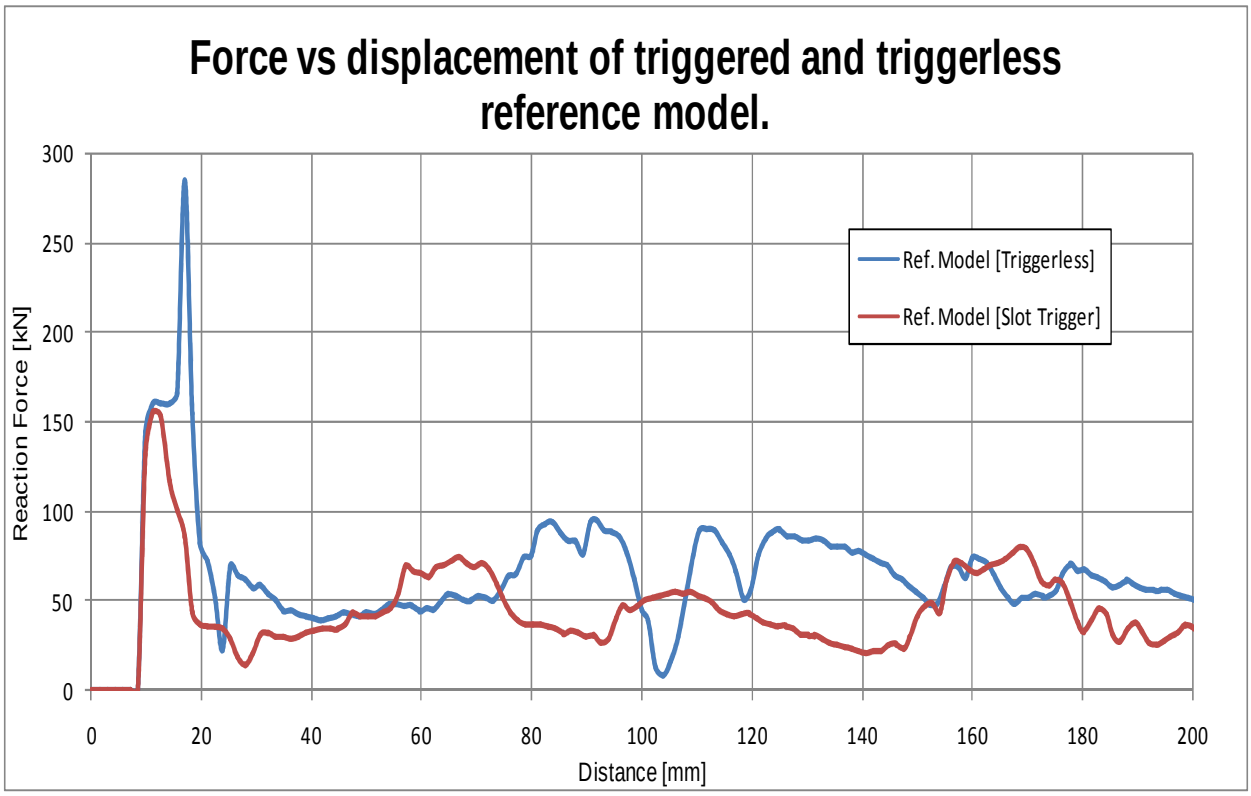

Fig. 4.2. Comparison of triggerless and notch trigger Force vs. displacement curves

4.3 Notch trigger design in SLD beams.

4.3.1 Description

Notch triggers were tried and tested for two of the best performing SLD patterns. Notches were placed directly at the hinge lines (normally the third hinge line from the front). In the case when notches were placed on all four sides, the adjacent walls were notched in the opposite directions (e.g. if notches on the top and bottom walls bulged outwards, notches at the left and right walls bulged inwards consequently). Two SLD patterns, SLD13 and SLD16 were tested as they had the most efficient dissipation characteristics. The description of the triggers is detailed in Table 4.1. Fig. 4.3 depicts a dual notch trigger on SLD16-T4.

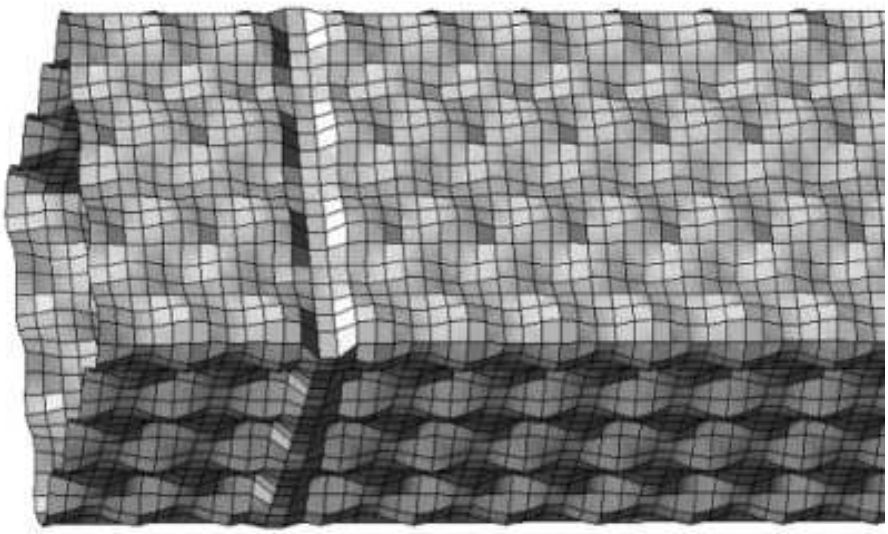

Fig. 4.3 SLD16-T4 showing notch triggers on all four sides of the patterned beam.

Model	No. of Notches	Notch Depth (mm)	Width at opening (mm)	Dist. form front edge (mm)
SLD13	0	-	-	-
SLD13T1	2	1.5	15	62.5
SLD13T2	4	1.5	15	62.5

SLD13T3	2	3.0	15	62.5
SLD13T4	4	3.0	15	62.5
SLD13T5	2	4:5	25	62.5
SLD16	0	-	-	-
SLD16T1	2	1.5	10	70
SLD16T2	4	1.5	10	70
SLD16T3	2	3.0	10	70
SLD16T4	4	3.0	10	70
SLD16T5	2	4.5	10	70

Table 4.1. Description of notches on SLD beams.

4.3.2 FEM Results for trigger design in SLD beams.

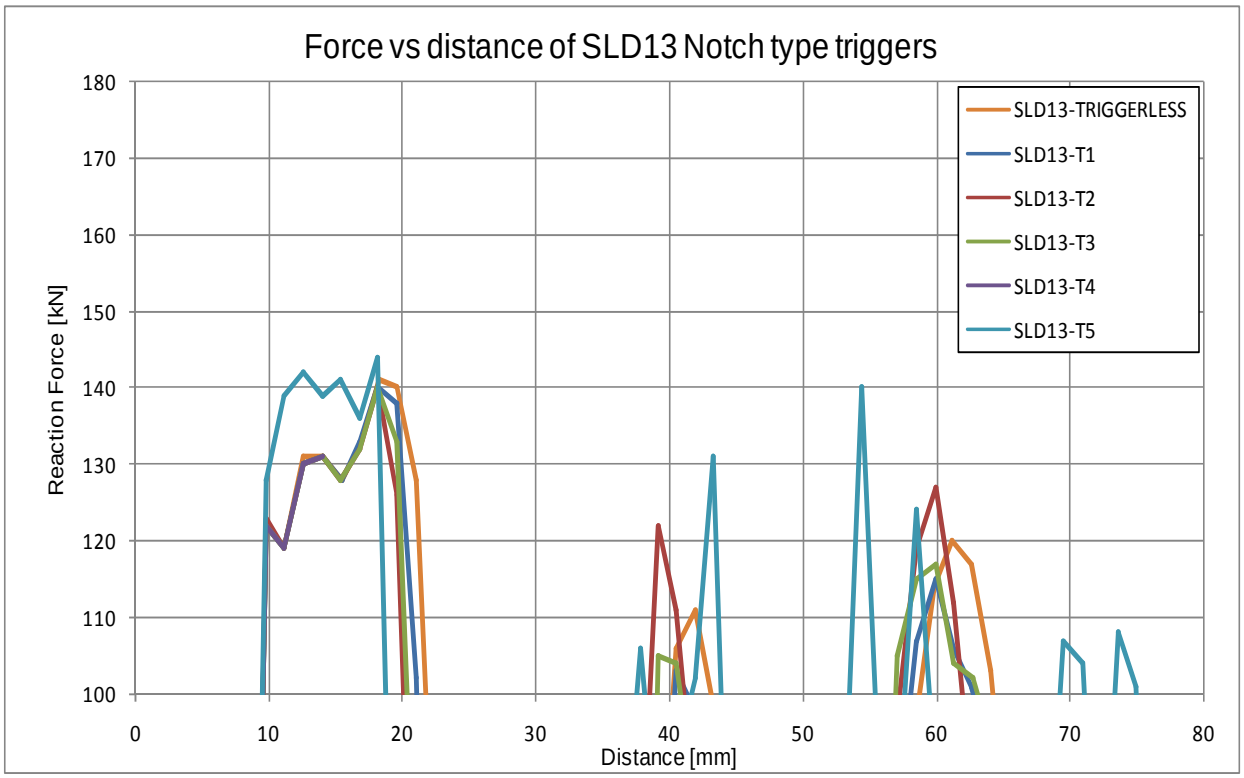

Fig. 4.4. Comparison of different triggers for SLD13 Force vs. displacement curves.

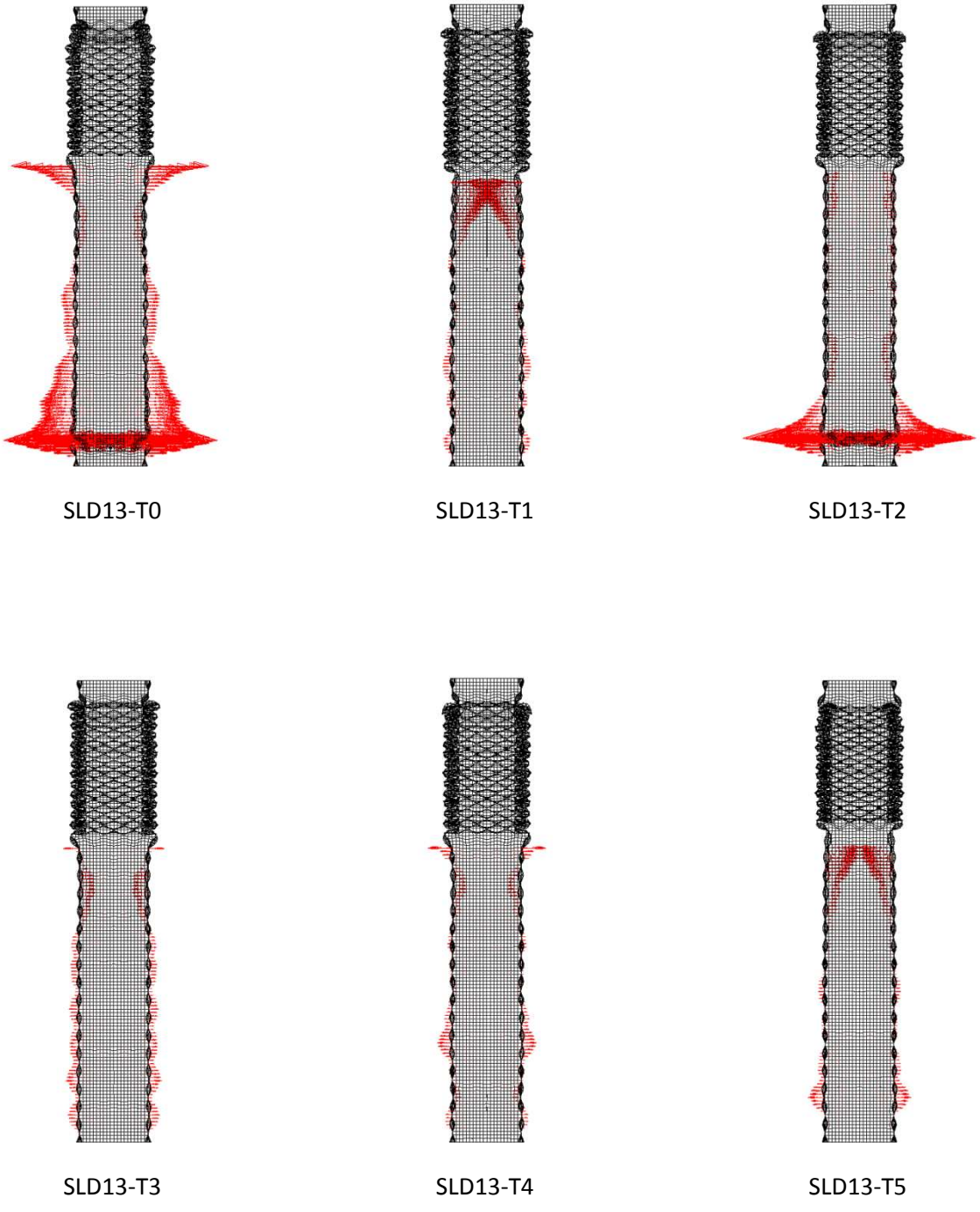

Fig. 4.5. Collapse shapes of triggers in SLD 13 patterns.

In the triggers tested on SLD13, the initial force spike is only slightly reduced as apparent in Fig. 4.4. On the contrary, due to the lopsided formation of the first fold upon impact a higher secondry force spike is seen on the graph when the second fold of the buckle initiates. This secondry spike undermines all advantage of lowerning the first spike and can lead to buckling occcuring elsewhere as seen in SLD13-T2 collapse shown in Fig. 4.5. This type of collapse makes the beam vunerable to global bending or kneeing out during misalinged crashes.

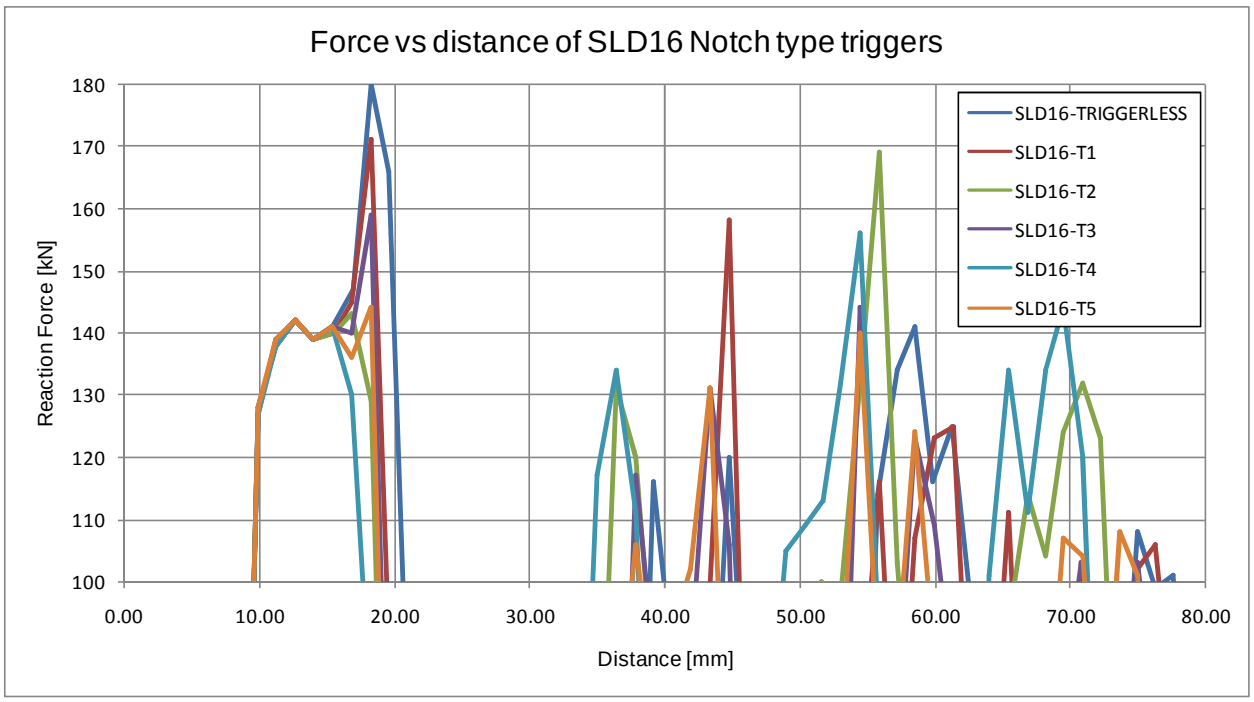

Fig. 4.6. Comparison of different triggers for SLD16 Force vs. displacement curves.

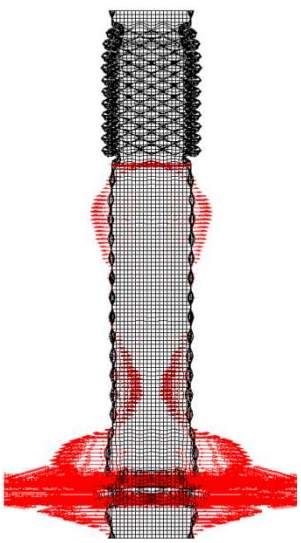

SLD16-T0

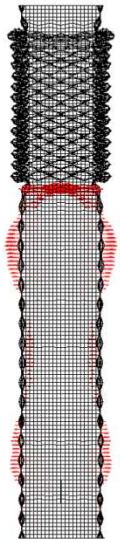

SLD16-T1

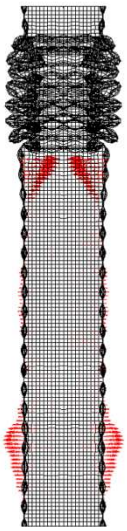

SLD16-T2

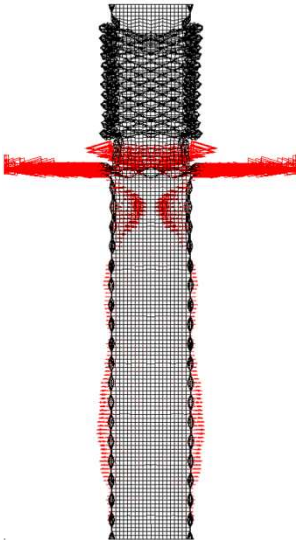

SLD16-T3

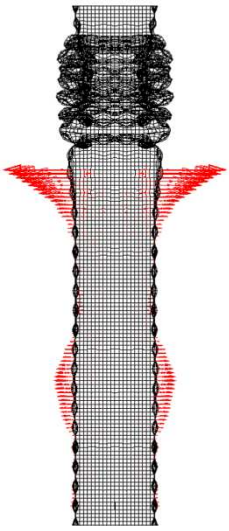

SLD16-T4

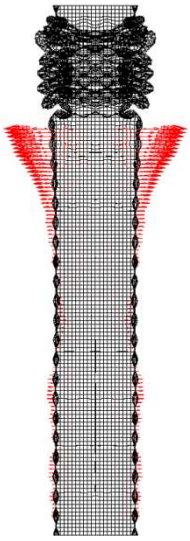

SLD16-T5

Fig. 4.7. Collapse shapes of triggers in SLD 16 pattern

For SLD16 the triggers are effective in the reduction of the first force spike as obvious in Fig. 4.6. The subsequent increase of the secondary force spike is still higher raising an issue of unwanted buckle initiation elsewhere as in SLD16-T4 in Fig. 4.7. Moreover, Fig. 4.7 also shows that the lopsided formation of the first buckle causes SLD16-T2, SLD16-T4 and SLD16-T5 patterns to fall into an undesirable multiple-hinge-per-fold collapse mode.

A schematic explanation of the behavior of Notch type triggers on a patterned SLD beam is given in Fig. 4.8. Since SLD beams have fixed hinge positions, the buckle formation on the triggering point is unbalanced. This causes a secondary force spike after the first fold has completely folded, which can sometimes be as high as the first force spike thus causing buckling elsewhere or causing multiple hinge per fold as visible in Fig. 4.7. A more desirable collapse formation is shown in Fig. 4.9.

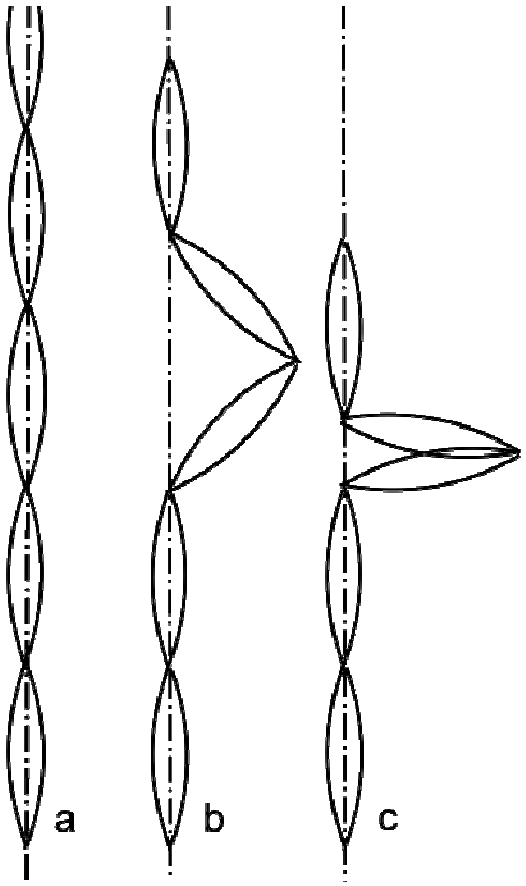

Fig. 4.8 Crash initiation of SLD patterns with notch triggers.

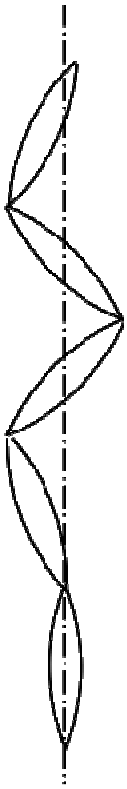

Fig. 4.9. Desirable crash initiation for SLD patterns

From these results, it can be concluded that it may be possible to optimize slot type triggers to eventually work for SLD patterned beams but it is evident that they may not be as universally effective as they are in simple box beams.

4.4 Progressive buckling triggers

4.4.1 Model description

In the progressive buckling trigger design, the third wave λ_3 is progressively amplified along the length of the beam. This increase in amplitude varies the pattern and makes the nodal hinges near the edge slightly more offset than the rest of the beam and collapse more readily than other areas of the beam. An exaggerated difference between both ends of the beam is shown in Fig. 4.10 and 4.11.

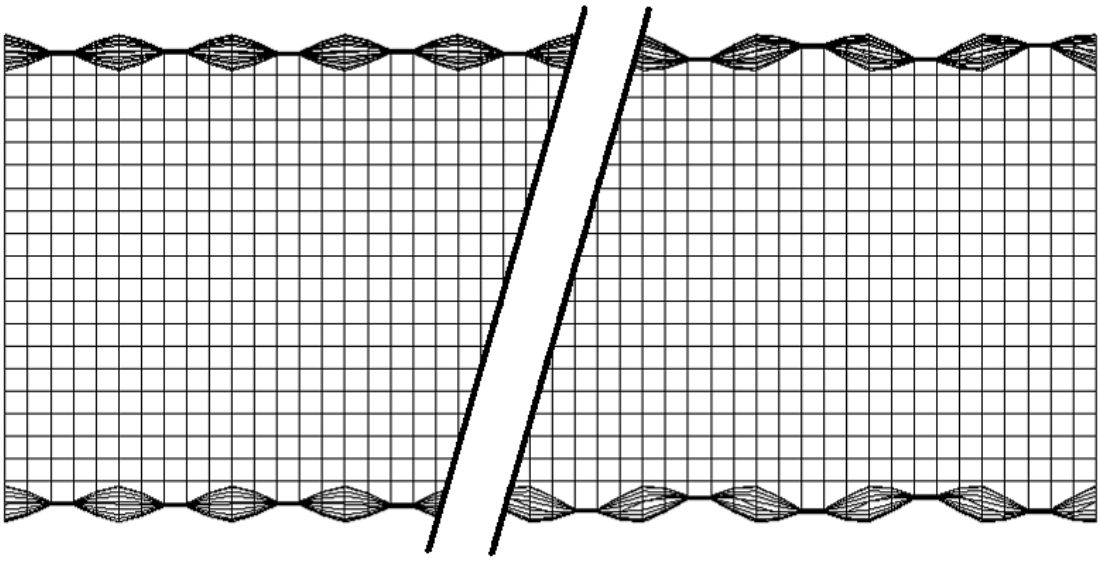

Fig. 4.10. Both ends of a SLD pattern with progressive triggering.

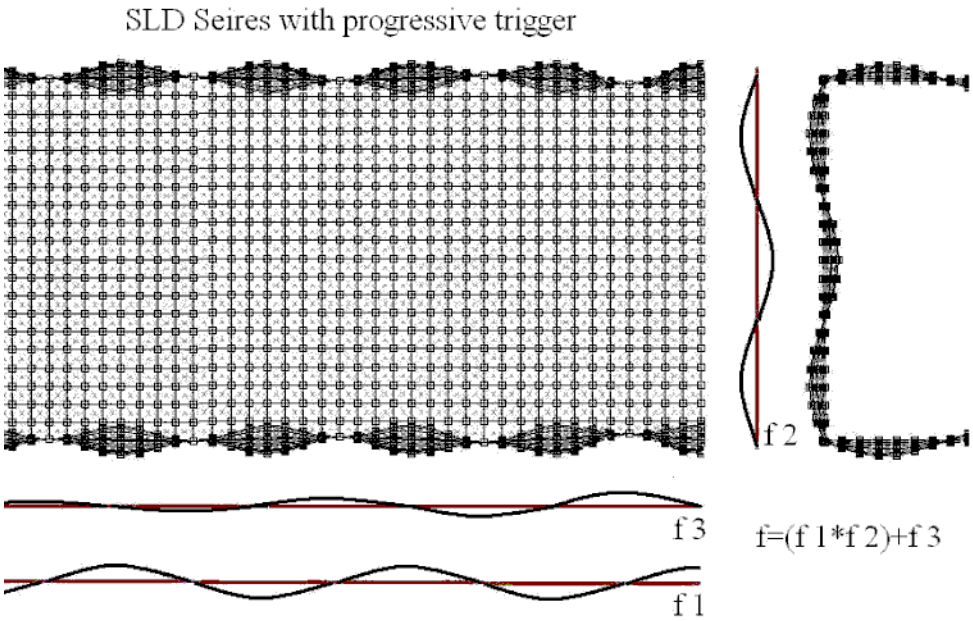

Fig. 4.11. SLD pattern with progressive triggering (the third wave, amplifying closer to the frontal edge).

The formulation used to construct progressive patterns is given in Equation 4.1. Note that the equation is also a function of z which denotes the longitudinal depth of the beam.

$$t \pm \frac{c}{2} \pm \cos\left(x * \frac{2\pi}{\lambda_1}\right) * \left(\left(\cos\left(z * \frac{2\pi}{\lambda_2}\right)\right) + 1\right) * a_{1,2} \pm \sin\left(z * \frac{2\pi}{\lambda_3}\right) * \left(a_{3min} + \left(\frac{z(a_{3max} - a_{3min})}{l}\right)^n \right) \quad (4.1)$$

a_{3min} and a_{3max} represent the minimum and maximum values of the amplitude of the third wave. l is the length of the beam, n is the progression exponent number. while the rest of the quantities have been described earlier.

The effect of parameters a_{3min}, a_{3max} and n will be analyzed separately in the following sections.

A tabulated description of the progressively triggered SLD patterns tested is given in Table 4.2.

Model	λ_1 (mm)	λ_2 (mm)	$a_{1,2}$ (mm)	λ_3 (mm)	a_{3min} (mm)	a_{3max} (mm)	n
SLD13-P1	26	28.57	2	52	0.05	1.05	2 (SQUARE)
SLD13-P2	26	28.57	2	52	0.1	1.10	3 (CUBIC)
SLD13-P3	26	28.57	2	52	0.16	1.16	3 (CUBIC)
SLD13-P4	26	28.57	2	52	0.16	0.66	2 (SQUARE)
SLD13-P5	26	28.57	2	52	0.16	0.66	1 (LINEAR)
SLD13-P6	26	28.57	2	52	0.16	0.66	3 (CUBIC)
SLD13-P7	26	28.57	2	52	0.16	1.16	1 (LINEAR)
SLD16-P1	25	28.57	2	50	0.16	0.66	1 (LINEAR)
SLD16-P2	25	28.57	2	50	0.16	0.827	1 (LINEAR)
SLD16-P3	25	28.57	2	50	0.16	1.16	1 (LINEAR)
SLD16-P4	25	28.57	2	50	0.16	1.66	1 (LINEAR)

Table 4.2. Description of progressive triggers on SLD patterns

4.4.2 Stage 1 FEM Results: Determining the α_{3min} value

In SLD13-P1 the amplitude α_3 varies between 0.05 to 1.05, whereas this amplitude was fixed at 0.3 in the trigger-less SLD13 version. In other designs such as SLD11, α_3 value of 0.15 has also been used and observed to work well. α_3 varies from 0.1 to 1.1 in SLD13-P2 and from 0.16 to 1.6 in SLD13-P3. Collapse formations for SLD13-P1, P2 and P3 for 40ms, 52ms and 80ms are given in Fig. 4.12.

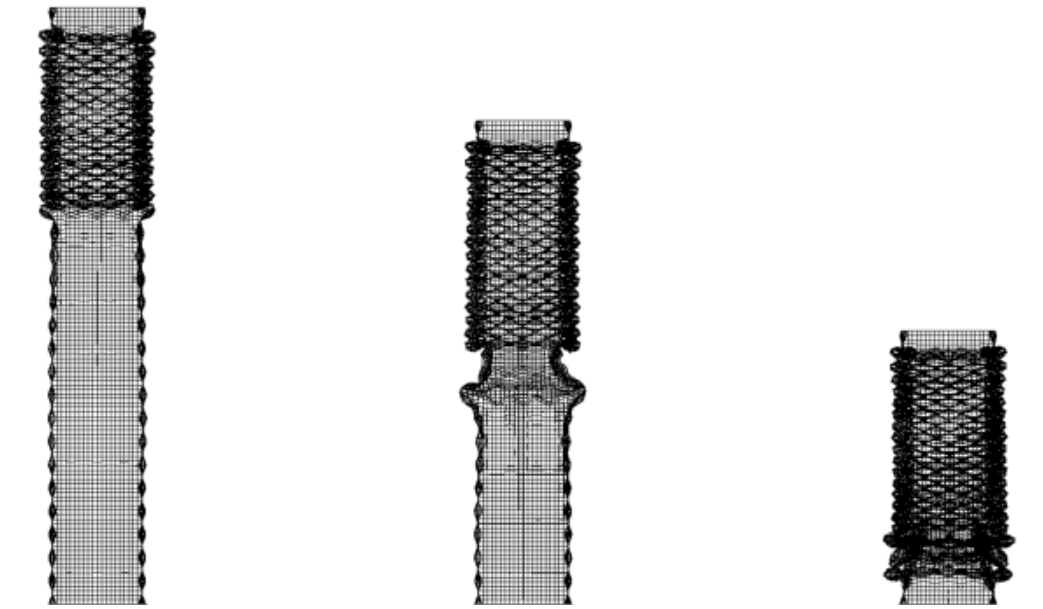

Fig. 4.12 (a). SLD13-P1, at three different stages of collapse.

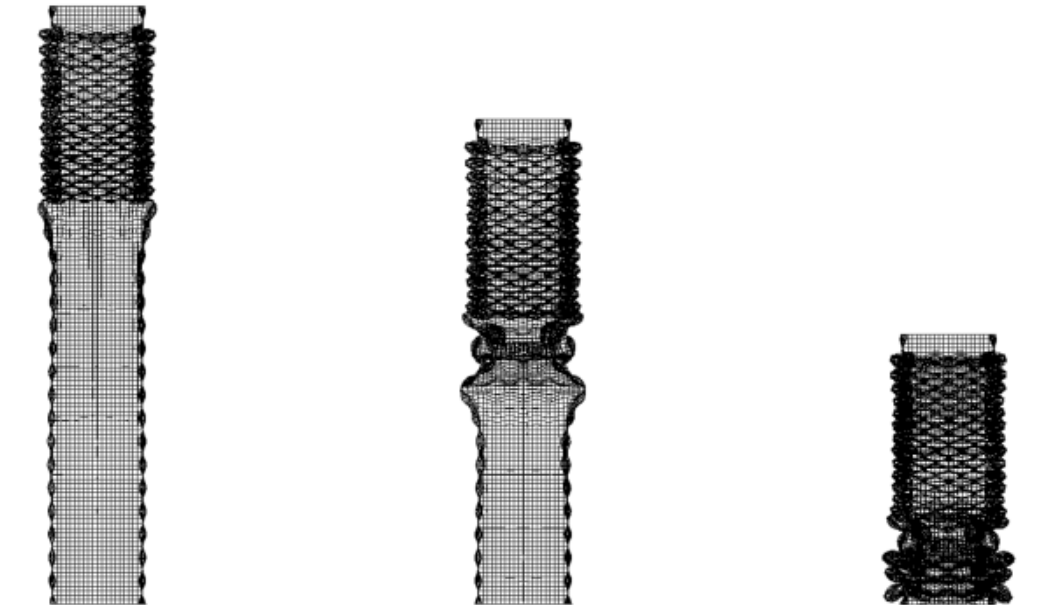

Fig. 4.12 (b). SLD13-P2, at three different stages of collapse.

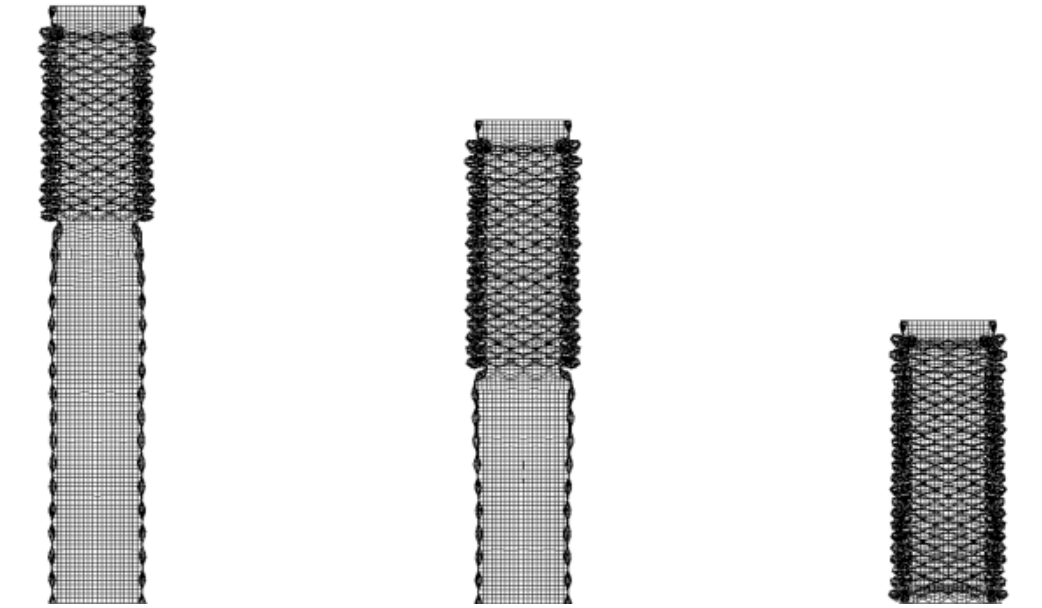

Fig. 4.12(c). SLD13-P3, at three different stages of collapse.

The triggers work well initially to initiate a stable collapse at the desired location in all three cases. However, in SLD13-P1 and SLD13-P2, as the instantaneous value of α_3 falls below approximately 0.15, the buckling mode changes from single hinge per fold to multiple hinge per fold mode. This does not occur in SLD13-P3 as the α_{3min} value is 0.16. In all subsequent models, the minimum value of α_3 was kept above 0.15 while no restraint was put on the maximum value.

4.4.3 Stage 2 FEM Results: Comparison of stray deformations on progressive triggers

The plastic stray deformations which occur out of sync on the beam were much lower and better in the progressively triggered beams as compared to the SLD beams with notch triggers.

In none of the progressively triggered beams tested did any stray buckles occur. A vector plot of displacement on the lower un-deformed part of the beams after 40ms of collapse is shown in Fig. 4.13. None of the beams showed any concentrated deformation at any hinge and the harmonic deformations are spread out more evenly indicating no early damage to the un-deformed part of the beam.

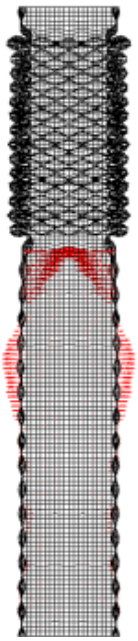
SLD13-P1


SLD13-P2

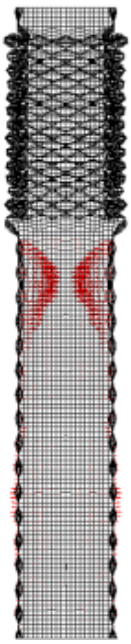
SLD13-P3

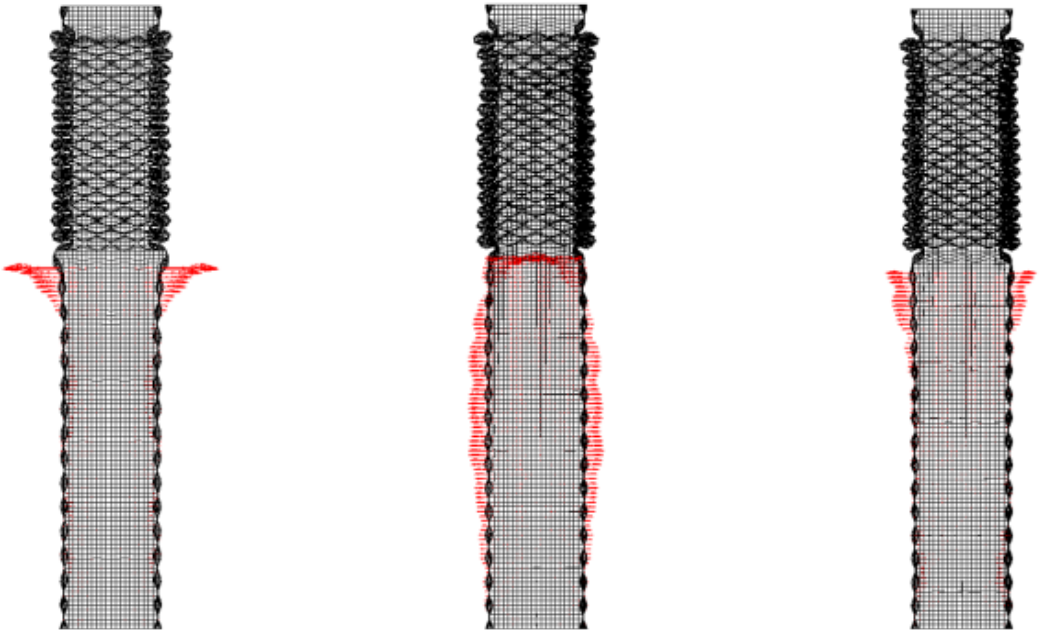

Fig. 4.13. Deformations at 40ms of selected SLD13 and SLD16 progressive triggers. Vector plot of stray deformations is shown to underline stray deformations.

4.4.4 Stage 3 FEM Results: Effect of a_{3max} on initial peak

Fig. 4.14 shows the reaction force vs. distance graphs of various SLD16 progressive triggers with varying a_3 maximum value. It is observed that progressive triggers can be effectively used to reduce the peak force. Furthermore, It is observed that the value of a_{3max} inversely affects the peak force, and thus can be set according to the peak force desired.

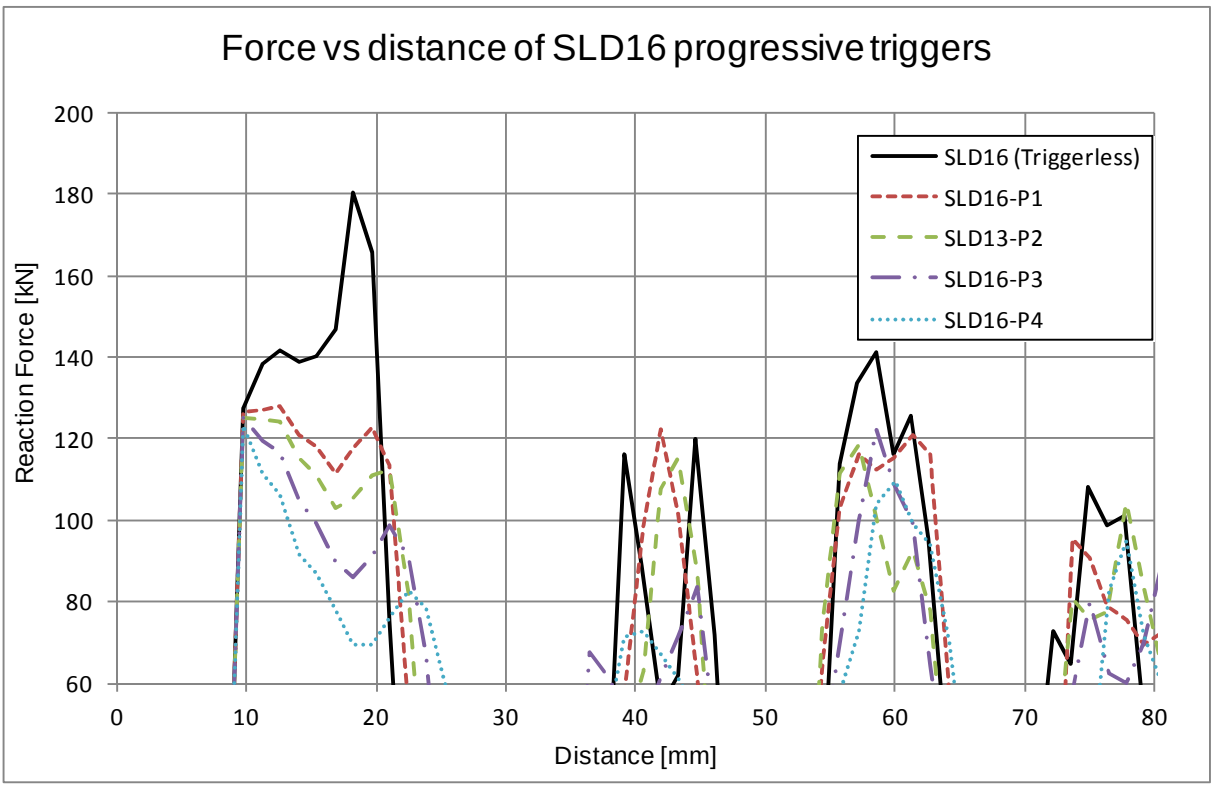

Fig. 4.14. Various SLD16 progressive triggers with varying a_3 maximum value. Force vs. distance graphs

4.4.5 Stage 4 FEM Results: Effect of progression coefficient *n* on the loss of energy.

Progressive triggers did not notably lower the total amount of energy absorption of the SLD beams despite lowering the initial force spikes. Since a_{3min} in progressive triggers was lower than the constant a_3 value in trigger less model in SLD13, the energy absorption per unit length became higher towards the end of the beam and compensated for the earlier loss. Fig. 4.15 shows the energy vs distance graph of SLD13 beam with progressive triggers with *n*=1,2,3 in comparison with the trigger-less model. Progressively triggered models all absorb less energy at the beginning, but the curves rise up later. The curves with higher coefficient n, minimize energy loss because the instantaneous value of a_3 falls steeply more just after the initial trigger. SLD13-P6 model with *n*=3 absorbs slightly higher energy than the trigger-less model. A slightly similar trend was noticeable in SLD16 models. The values of energy loss are given in Table 4.3.

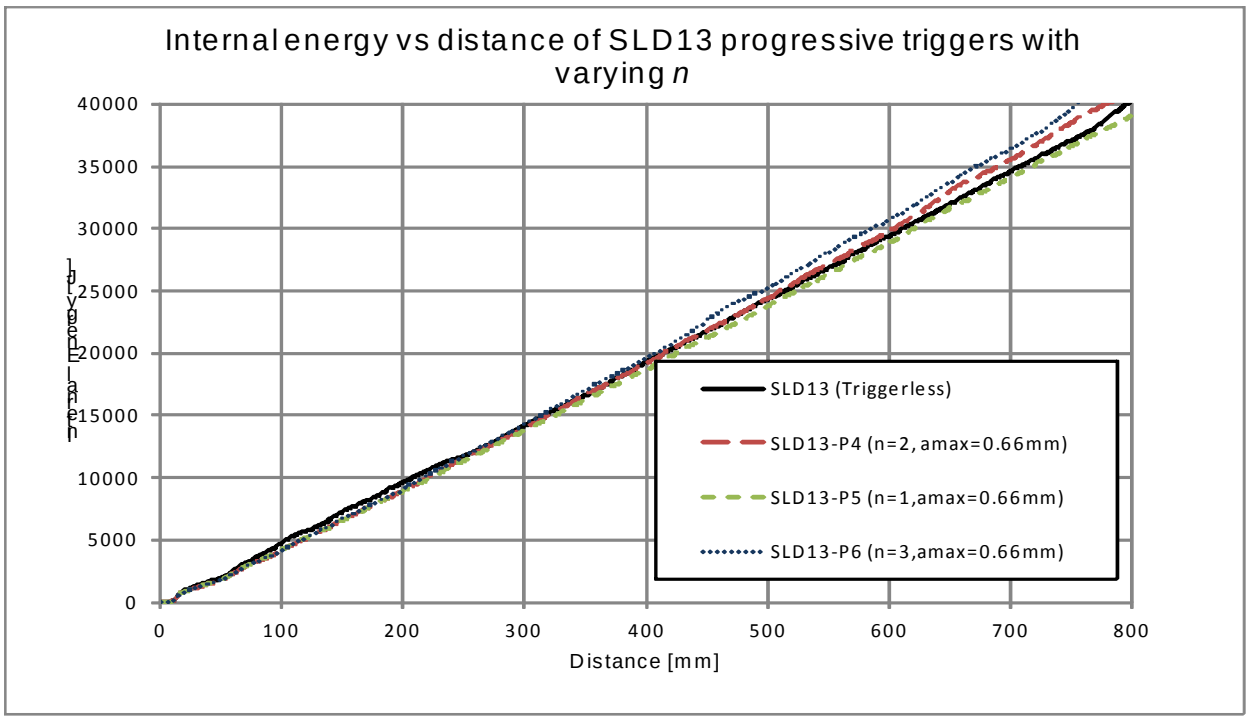

Fig.4.15. Energy vs. distance curves of SLD13 progressive triggers with varying *n* exponent.

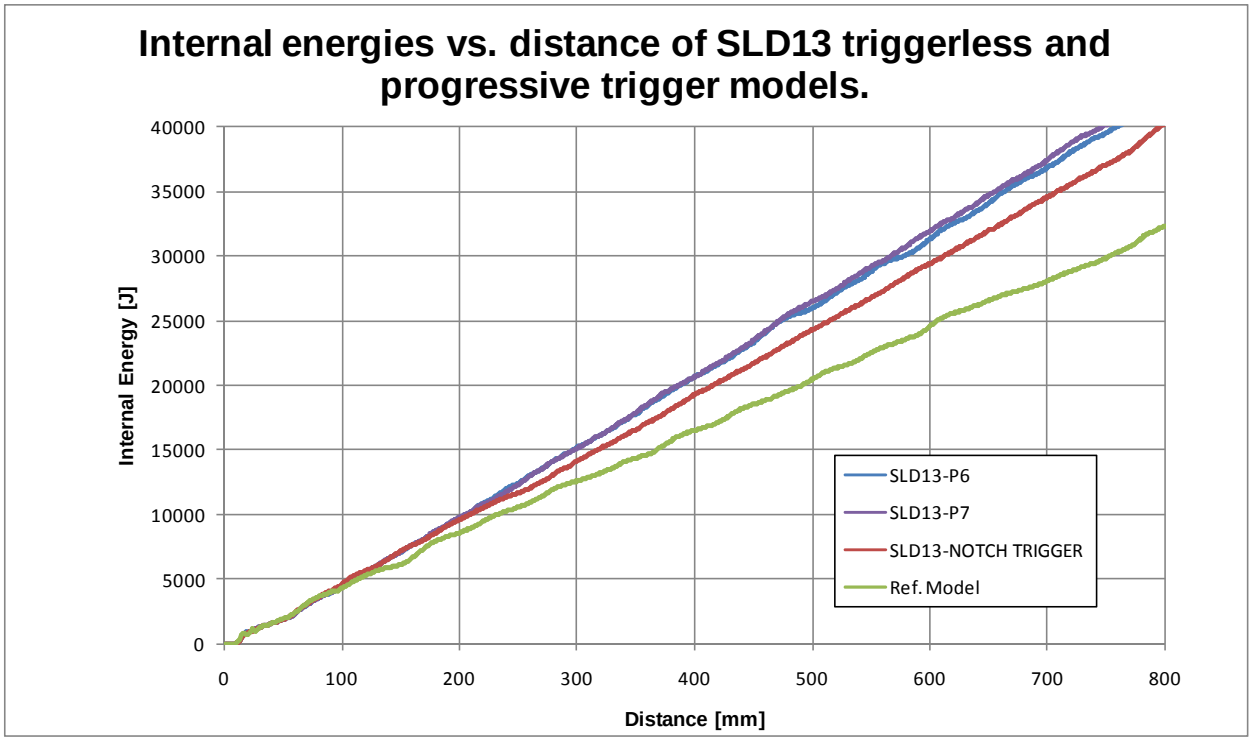

Fig. 4.16, Energy absorption of SLD13 progressive triggers in comparison to SLD13notch trigger and the reference model.

It can be seen in the graph that the progressive frequency trigger designs (SLD13-P6 and SLD13-P7) absorb slightly more energy than the SLD 13 Notch trigger design. It was observed in section 3 that notch triggers can cause instable buckling, with might explain the loss of energy in this case. Progressive trigger models are also seen to show a more stable buckling collapse mode without causing plastic deformations at undesirable places. The buckle formation of SLD13-P7 beam is shown in Fig. 4.17.

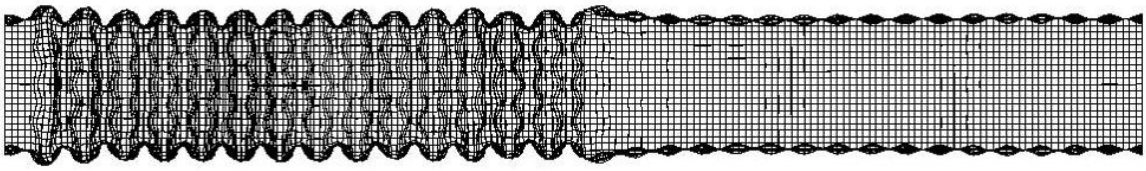

Fig. 4.17. SLD13-P7 Progressive trigger beam, buckle formation. (Displacement mag. x 0.63)

4.4.6 Summarized Results:

A tabulated summary for the performance of progressive triggers tested is given in Table 4.3

Model	a_{3min} (mm)	a_{3max} (mm)	n	E (kJ) at 900mm	φ	%age Inc. in E & φ from Triggerless	F_{max} (kN)	%age Inc. in F_{max} from Triggerless
SLD13	0.3	0.3	-	50.2	1.47	-	140.87	-
SLD13-P1	0.05	1.05	2	47.4	1.39	-5.41	140.86	-0.01
SLD13-P2	0.1	1.10	3	44.3	1.30	-11.77	140.10	-0.55
SLD13-P3	0.16	1.16	3	50.5	1.48	0.77	137.44	-2.44
SLD13-P4	0.16	0.66	2	50.8	1.49	1.37	136.08	-3.40
SLD13-P5	0.16	0.66	1	49.9	1.47	-0.54	128.62	-8.70
SLD13-P6	0.16	0.66	3	51.4	1.51	2.52	144.12	2.31

SLD13-P7	0.16	1.16	1	48.1	1.41	-4.01	126.10	-10.49
SLD16	0.1	0.1		52.4	1.54	-	180.26	-
SLD16-P1	0.16	0.66	1	52.3	1.54	-0.32	128.11	-28.93
SLD16-P2	0.16	0.827	1	51.7	1.52	-1.32	125.06	-30.62
SLD16-P3	0.16	1.16	1	48.8	1.43	-6.86	125.18	-30.56
SLD16-P4	0.16	1.66	1	46.4	1.36	-11.54	123.24	-31.64

Table 4.3. Crash performance of SLD-13 and SLD-16 progressive triggers.

F_{max} is the peak reaction force during the collapse. A lower max force at a minimal or no loss of energy is desirable. The energy absorption effectiveness factor of a plain beam of similar dimensions is 1.08 [1].

4.5. Conclusions.

It was observed that notch type triggers that are very widely and effectively used for regular beams have limited effectiveness in patterned beams where the hinges are predefined. Buckle formations for SLD beams with notch type triggers could cause irregular and out of place buckling, thus causing global collapses. Progressive triggers with a variable frequency could offer a reasonable alternative to using notch triggers for Patterned beams. These progressive triggers were observed to show a very regular pattern formation if the amplitude of the third wave was kept within a predetermined range.

These progressive triggers have to be tested for oblique loading and misaligned crash tests to determine their viability.

Chapter 5. SLD beams under bending, offset mass impact and oblique impacts.

5.1 Introduction

Most crash absorbers are tested for axial impact. There can be two principle modes of collapse for thin walled beams: axial and bending. In real life automotive accidents, crash absorbers collapse in mostly are a combination of the two modes and hardly ever does an automotive crash occur in only pure bending or only pure axial impact. It is very important to study the performance of thin walled beams in oblique impacts where a combination of axial force and lateral force act simultaneously on the crash beam.

Many authors have worked on the axial impact with numerical, experimental and analytical methods [1-24] Their work has been discussed in the previous chapters in detail.

The behavior of thin walled square and rectangular beams under pure bending has been extensively studied on various occasions previously. In one of the fundamental studies on the subject, Kecman [28] established an analytical folding mechanism based on a hinge geometry as shown in Fig.5.1, Weizerbiki and Abramowics [29] also further studied various aspects of the deep bending collapse and introduced plastic flow over toroidal surface hinge lines during buckling, these works were followed up by Kim and Reid [30] who developed fully analytical collapse curve models to give an improved analytical solution for the moment-rotation relationship.

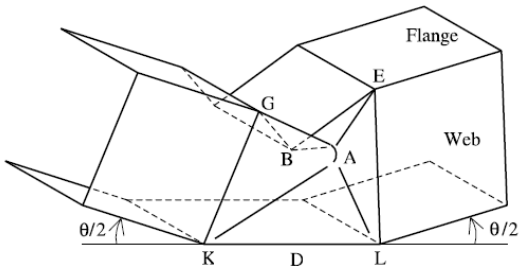

Fig.5.1. Kecman's [28] square beam collapse model

Amongst other significant works, Kotelko, Lim and Rhodes [31] experimentally analyzed post buckling behavior of box section beams and compared them to existing theoretical models. Corona and Vaze [32] also experimentally and analytically studied the buckling and collapse on long, thin walled square tubes. In yet another important and relevant study, P.Drazetic, E. Markiewicz et al. [33, 34] developed distinct analytical models for theoretical prediction of pre-collapse, collapse and post collapse behavior. P Hosseini, Tehrani and M Nikahd [35] studied various configurations of incorporating various formed ribs into the walls of the S-frame (used in the front crumple zone of a passenger car chassis) and considered their effects on energy absorption and force response during buckling collapses during crashes. An experimental study of the large deformation of plastic hinges was done by McIvor et al.[36] They also proposed semi empirical formulation for bending collapse. Work on large curvature modeling was done by Guy and Louis [37]. Kecman also gave a useful overview of the approach [38] for bending collapses. Numerical Investigation on plastic collapse of thin walled beams subjected to biaxial bending were carried out by Giovanni and Peroni[39], while a design method was proposed by Frode et. al. [40].

Interestingly, misaligned or oblique impacts they have received comparatively lesser interest by authors as compared to axial and pure bending collapses.

A comprehensive study on the bending compression interaction in the failure was done by Suh [41] in 1987. He carried out a purely theoretical plastic analysis of circular dented tubes under a combination of axial and bending load. Suh also worked on a simplified model and developed a failure locus. N. E. Shanmugam, J. Y. Richard Liew & S. L. Lee [42] studied biaxial loading analytically in steel beams for civil engineering applications. Reyes A, Langseth M, and Hopperstad OS [43-44] studied the oblique loading behavior of square aluminum beams by experimental tests and numerical techniques. They conducted experiments by fully fixing one

end of the tube and clamping the other end to a loading actuator, Oblique loading conditions were then achieved by applying a quasi-static load at different angles to the centre line of the beam. They concluded that the peak and mean reaction force dropped significantly as the load angle increased, i.e. when bending was introduced into the column, they also studied the validity of different finite element codes. Wallentowitz and Adam [45] also carried out experimental studies on the hat-type section column under oblique loads and underlined the need to further investigate the topic. Similar studies on foam-filled circular and square aluminum tubes have been studied under oblique quasi-static loading have been conducted by Borvik et. al. [46] and Reyes et. al. [47]. Another relevant Numerical study on the oblique loading of mild steel square columns was carried out by Han DC, Park SH. [48],They preformed oblique loading tests by axially impacting beams at an inclined rigid wall of varying degrees. Their study also included studying the impact of different parameters such as length, thickness and width. Results showed that there is a critical angle at which a transition occurs from a dominant progressive axial collapse mode to a dominant bending collapse mode. There was a sizeable drop in the amount of energy absorbed associated with this transition, an example of the transition is given in Fig.5.2.

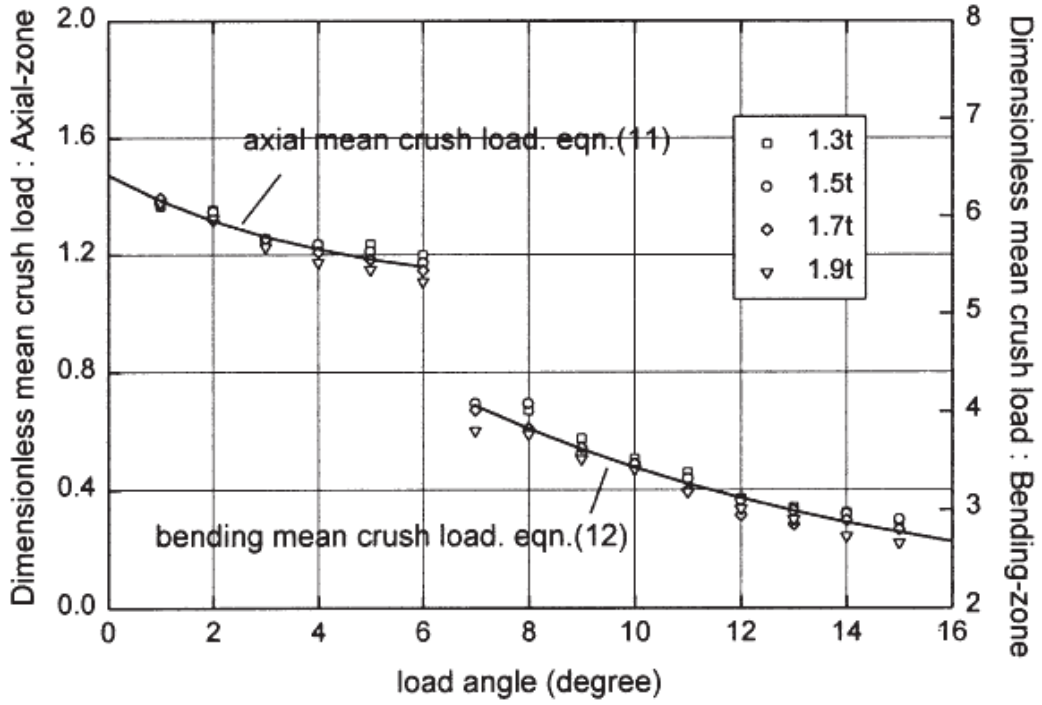

Fig. 5.2. Example of mean reaction force vs. load angle as studied by Han DC and Park SH [48].

Theoretical methods for a beam in combined bending and compression have been proposed by Kim and Wierzbicki [49].These models were also compared against numerical simulations in their study.

Some authors like Nagel, Thambiratnam [50-51] and Reid also worked upon the design and performance in oblique impacts of a tapered beams to improve performance in oblique loading. They concluded that tapered beams can be used as an effective method to increase resistance to kneeing out, but tapered beams absorbed lesser energy per weight as compared to normal beams.

The aim of this chapter is to test the proposed beams for oblique and offset loading conditions in which the impact angle is not perfectly normal to the beam direction. The author believes that the oblique test in which a rigid wall at an angle is impacted upon may not be a universal measure which can test a beams performance in all real life conditions. In reality, the surface is not frictionless. Secondly, impact surface and impact velocity may not be always perpendicular; the impact velocity may be at a one oblique angle, and the impacting surface might be at another oblique angle.

For this reason, Another test was also devised called the offset mass test along with the oblique impact test. In this an offset ball mass is placed behind the beam. The description of this test is given in the later sections.

Both the offset mass test and the oblique impact test were performed to test the stability of SLD pattern beams, and progressively triggered SLD pattern beams in case of on offset impact. This test gives a comparison between the stability of regular beams vs. those with patterns.

In this chapter, the behavior of SLD patterned beams under a variety of oblique impacts has been studied.

Many impact scenarios and loading conditions have been simulated and the proposed beams have been tested for them. A comparison in then drawn up with the reference model and the effectiveness of SLD beams in real life scenarios is further predicted.

5.2 Pure bending collapse

Typically, the reaction moment of a buckling collapse of a thin walled structure is characterized as shown in Fig.5.2. It can be divided into three main phases as done by P. Drazetic et al [6,7] as 1) pre collapse, 2) collapse and 3) post collapse behavior. Often, if the thickness of a certain cross section is too thin and below a certain critical value the beam might buckle before it is

fully plastic and post collapse phase might be reached directly from the pre-collapse phase. This is also characterized and described by Kecman [28] in his study of the topic.

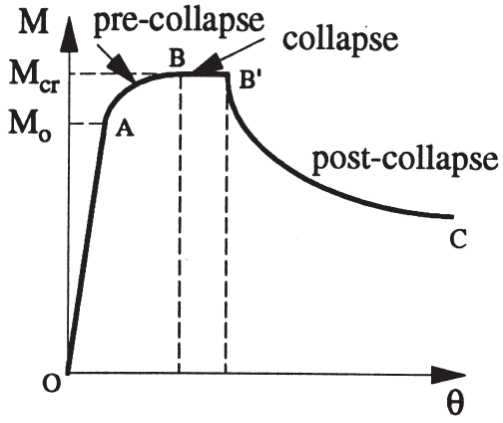

Fig. 5.3. Moment vs. rotation three stage curve as defined by P. Drazetic et. al.[34]

This section aims to fully comprehend deep bending collapse behavior in order to better predict deep bending collapses in automotive crashes amongst other applications. It is also desired to be able to control and manipulate the buckling behavior and enhance performances of desired parameters by optimizing the geometry. Furthermore, the performance of crash absorbers with SLD patterns is studied and compared with reference beams.

5.2.1 Theoretical formulation

For square cross sections, several authors have proposed analytical studies of the topic the moment of a beam vs. angle was be given by McIvor et al. [8] as:

$$M(\theta) = Mp\,[A + B\,(1 + k\,(\theta - \theta m))\,e^{-k\,(\theta-\theta m)}] \qquad (5.1)$$

where A, B and k represent constants pertaining to a specific beam dimensions The two coefficients *A* and *B* represent the constant and the vanish able parts of the moment. The last coefficient is the exponential decrement *k*. These three parameters are determined by applying a least-square analysis on either an experimental curve, a FE simulation of the plastic hinge or the analytic result given by the kinematic model of Kecman [2] [1]. M_p used in the equation above is the maximum Plastic moment given by the following equation:

$$Mp = \sigma_p t\,[a\,(b - t) + 0.5\,(b - 2t)^2]. \qquad (5.2)$$

where a, b and t are the width, depth and thickness of the rectangular section respectively

5.3 Offset mass test.

5.3.1 Model Description

In this test, both ends of the beam are linked to a central node to simulate a closed cap configuration. The central Nodes on each side are constrained to the vertical axis as shown in Fig. 5.4. A circular iron load of 500kg (with its respective moment of inertia) is connected to the beam through a rigid link with a varying offset. The beam and mass are given an initial velocity of 15.6m/s and impacted on a rigid wall.

The beam dimensions were 100mm by 100mm and a length of 600mm. The wall thickness of was kept at 1.7mm and boundary conditions were kept as shown in Fig. 5.4.

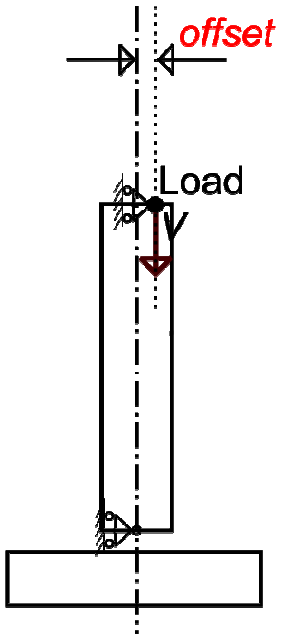

Fig. 5.4. Offset mass impact test configuration.

The rest of the parameters were left unchanged from the previous tests and Altair Hyperworks™ suite was used to model the test. The commercial solver Radioss™ was used as the explicit solver.

Eight different models belonging to three different categories of beams were tested for each degree increment of offset up till 10mm offset. A total of eighty runs were conducted for this test.

5.3.2 Results

Some of the selected results at different levels of offset are shown in Fig. 5.5. Since it is impossible to visually show all the tests run, only one of each category, namely, reference model. SLD notch type trigger and SLD progressive trigger design are shown.

	Reference Model	SLD11, Notch Trigger	SLD16-P1 Progressive Trigger
4mm Offset 40ms	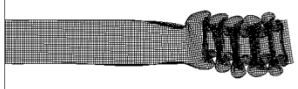		
4mm Offset 70ms		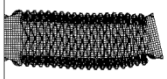	
	Reference Model	**SLD11, Notch Trigger**	**SLD16-P1 Progressive Trigger**
5mm Offset 40ms	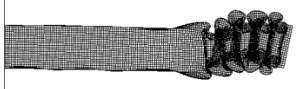		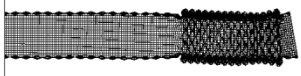
5mm Offset 70ms	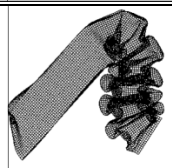	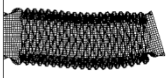	
	Reference Model	**SLD11, Notch Trigger**	**SLD16-P1 Progressive Trigger**
6mm Offset 40ms		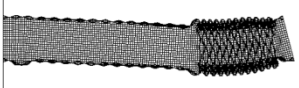	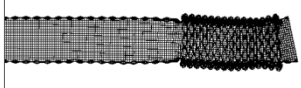

6mm Offset 70ms		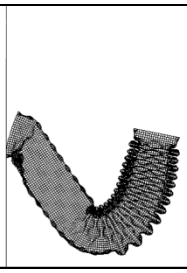	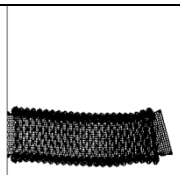
	Reference Model	**SLD11, Notch Trigger**	**SLD16-P1 Progressive Trigger**
7mm Offset 40ms	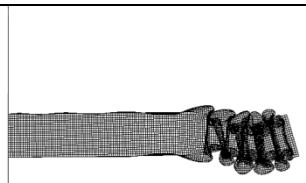	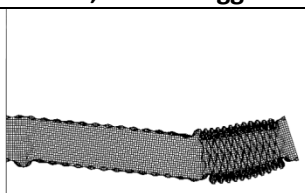	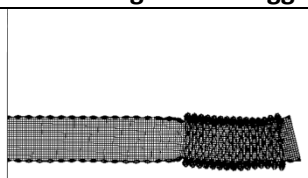
7mm Offset 70ms		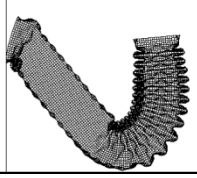	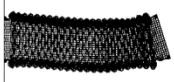
	Reference Model	**SLD11, Notch Trigger**	**SLD16-P1 Progressive Trigger**
8mm Offset 40ms	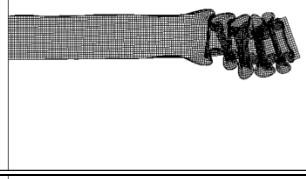	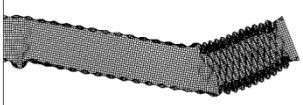	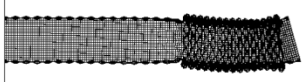
8mm Offset 70ms		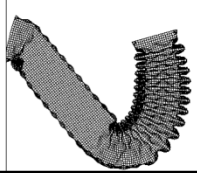	
	Reference Model	**SLD11, Notch Trigger**	**SLD16-P1 Progressive Trigger**
9mm Offset 40ms	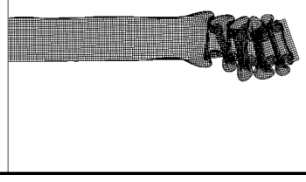		

9mm Offset **70ms**	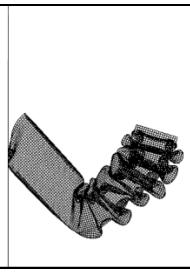	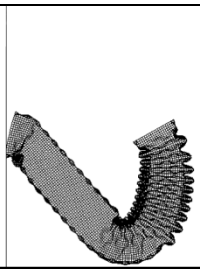	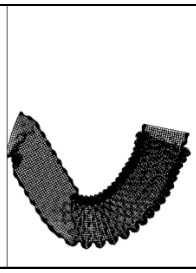
	Reference Model	**SLD11, Notch Trigger**	**SLD16-P1 Progressive Trigger**
10mm Offset **40ms**	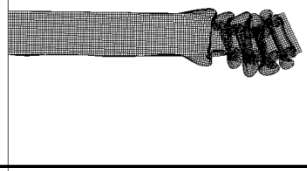	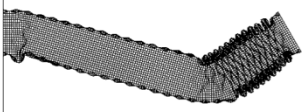	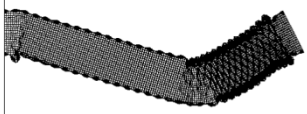
10mm Offset **70ms**		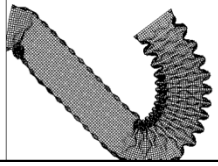	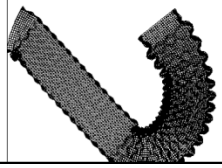

Fig.5.5. Crash formation of reference, SLD11(notch trigger) and SLD16-P1(progressive trigger).

The results indicate a very interesting behavior. The reference model with a notch trigger behaved erratically. It behaved well until an offset of 4mm. At 5mm offset the beam began to wobble and eventually globally bended in the same direction as the offset (It should have done so in the opposing direction logically) as shown in Fig.5.5. This shows a very unstably vibrating and thus unreliable behavior of the reference model. When the offset was increased, the beam surprisingly behaved better again until the next globally bended at 9mm offset.

The SLD beams with the notch triggers failed quite quickly, partly because notch type triggers are not very efficient for SLD beams. We tested two models, one in which the trigger worked reasonably, and the other in which the trigger did not work so well.

The SLD16 beam with an ineffective notch type trigger globally bended out at a mere 2 mm of offset. The working SLD11-notch triggered beam globally bended out at 6mm of offset, and behaved consistently.

The SLD beams with progressive triggers, as thought earlier offered the best behavior. They folded in the axial compression mode and kneeing-out or global bending failure did not occur till 9mm offset.

The Internal energy absorbed in collapse on various offset levels of the reference model and SLD16-P1 is shown in Fig.5.6 and 5.7. respectively

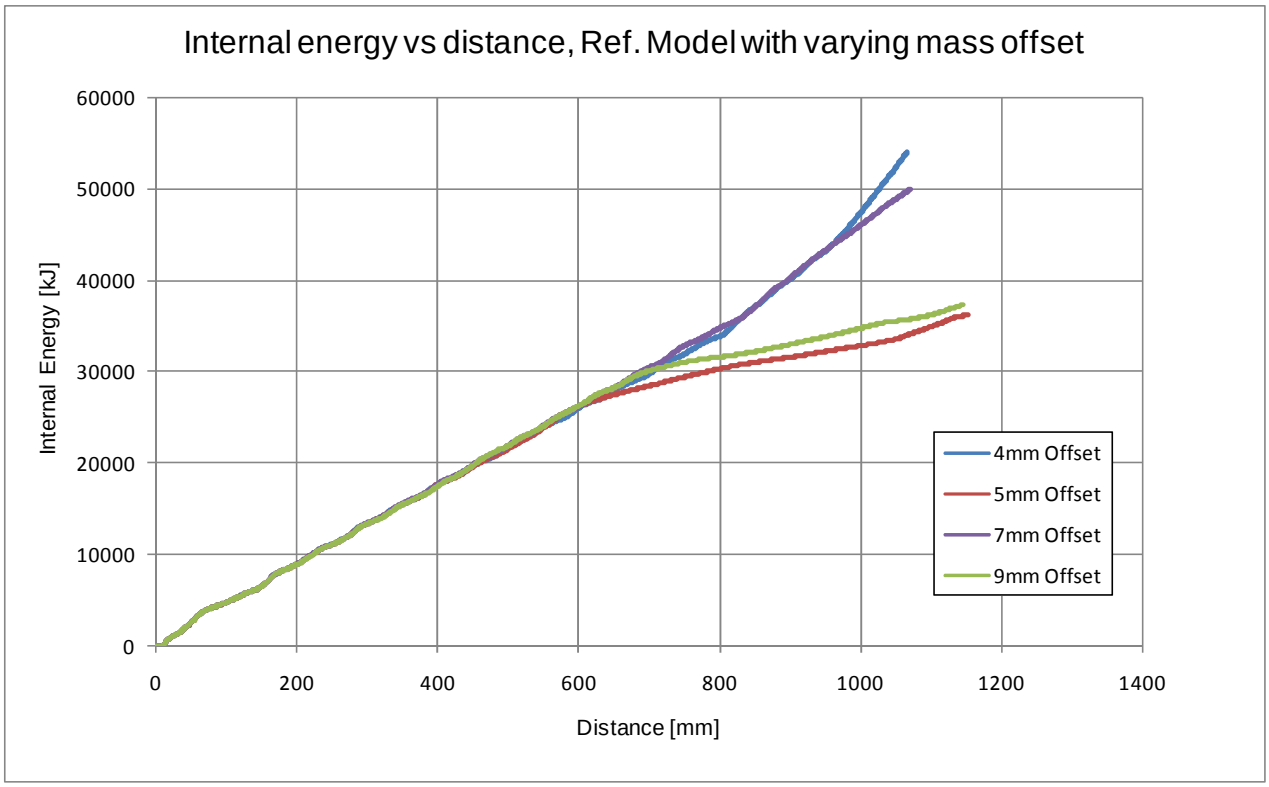

Fig. 5.6. The Internal energy absorbed in collapse on various offset levels of the reference model.

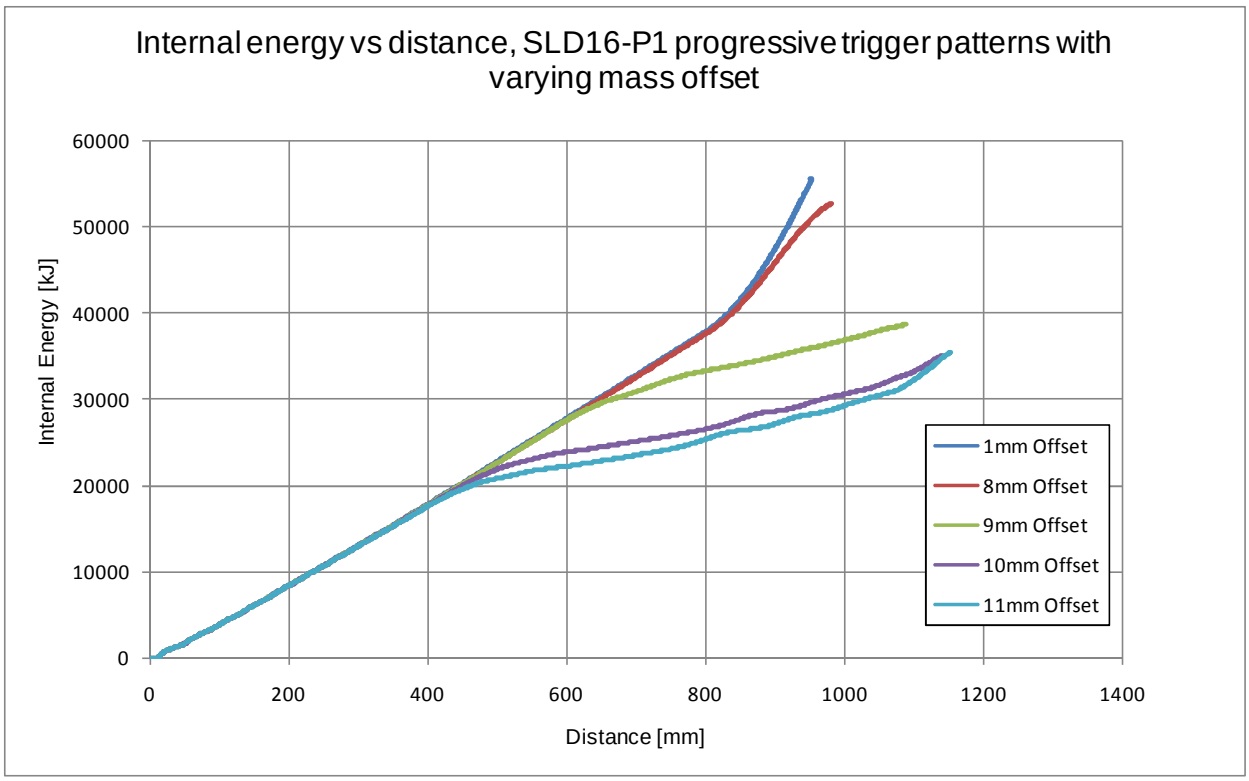

Fig. 5.7. The Internal energy absorbed in collapse on various offset levels of SLD16-P1 progressive trigger model.

It can be observed that in every case, there is a significant energy loss the moment global bending commences instead of axial collapse. The longer the axial collapse is sustained, the higher the energy absorbed. Progressive triggers behaved in axial collapse mode to the highest degree of offset.

Results are summarized in Table 5.1. The exact value of critical offset value when global buckling occurs cannot be determined as tests are run with 1mm interval. A range between it occurs the first time is mentioned instead. This can be a good measure of the stability of the beam.

Model	λ_1 (mm)	λ_2 (mm)	$\alpha_{1,2}$ (mm)	λ_3 (mm)	Min λ_3 amp	Max λ_3 amp	λ_3 Progression	Critical Offset range (mm)
REFERENCE MODEL								
Ref Mod.	-	-	-	-	-	-	-	**4 - 5**

NOTCH TRIGGERS								
SLD11	30	40	2	60	0.3	.3	-	**5 - 6**
SLD16	25	28.57	2	50	.3	.3	-	**< 1**
PROGRESSIVE TRIGGERS								
SLD13-P7	26	28.57	2	52	0.16	1.16	LINEAR	**7 - 8**
SLD11-P1	30	40	2	60	0.16	1.16	LINEAR	**7 - 8**
SLD11-P2	30	40	2	60	0.16	1.66	LINEAR	**6 - 7**
SLD16-P1	25	28.57	2	50	0.16	1.16	LINEAR	**8 - 9**
SLD16-P2	25	28.57	2	50	0.16	1.66	LINEAR	**8 - 9**

Table 5.1. Description of beams tested for offset mass impacts

5.4 Oblique Loading (capped and uncapped).

5.4.1 Model setup

The oblique loading model was setup using the same modeling conditions as used by many authors in the past [43-48]. In this setup shown in Fig. 5.8, A mass of 500 kg and the top rigid link is constrained against all linear and rotational motion except the z direction. The rigid wall is kept at a varying angle from 0 degrees to 10 degrees with a 1 degree interval. The contact surface is simulated as frictionless. The impact end of the beam is tested for both capped and uncapped front end.

As the normal beam of a length 1200mm was considered too long for this test, a shorter 600mm beam was modeled in this case. The cross-section and thickness dimensions were kept the same at 100x100mm and 1.7mm. The impact velocity was kept at 15.56m/s (56 km/h).

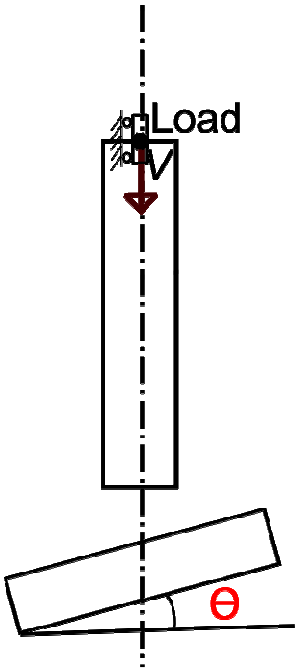

Fig.5.8. Oblique impact FEM setup.

5.4.2 Oblique crash behavior

Oblique impacts can be roughly classified into three modes of collapse. The first is purely axial collapse with no global bending (a). The second hybrid: predominantly axial mode of collapse with bending in the crushed zone only (b), the third type is the global bending collapse (c). The three collapse configurations are shown in Fig. 5.9.

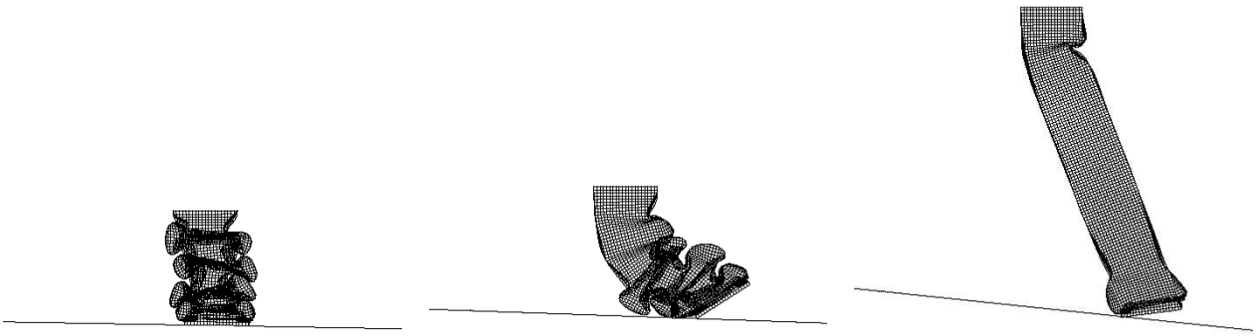

(a) (b) (c)

Fig. 5.9. Three different collapse modes in inclined impacts.

As noted by Han and Park [48], There is a critical inclination angle after which the collapse mode occurs predominantly in global bending mode. There is a significant loss in impact energy absorbed by the beam after this transition. This critical angle, therefore, becomes a very important performance parameter for beams. Fig. 5.10 shows the reaction force vs. distance graphs of the three failure modes.

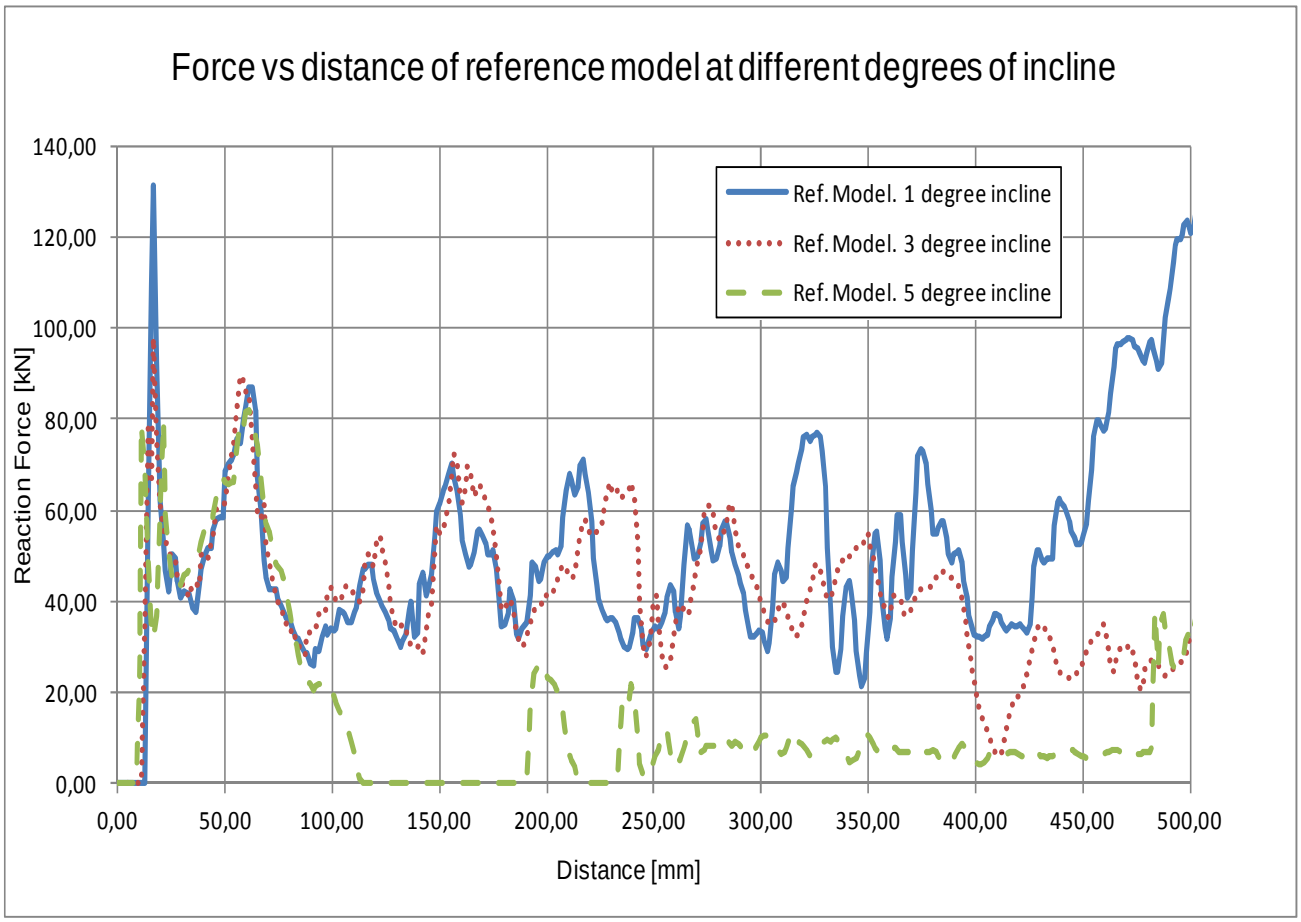

Fig. 5.10 (Force vs. distance graphs of the three modes)

Mode a and b have comparable force dissipation For the simple beam dimension tested, the critical angles from A to B lies between 1 to 2 degrees and from mode b to c is 4 to 5 degrees.

5.4.3 Capped and uncapped ends,

For oblique impacts, it is very important that the beams are triggered correctly and the buckling initiates at the front end only. In case a buckle occurs elsewhere, the beam is prone to behaving erratically and collapse in global bending even at very low inclination angles. Therefore, un-

triggered beams cannot be tested for oblique impacts and only triggered beams can be tested. A comparison is done between a plain reference beam with notch trigger, SLD patterned beams with a conventional notch trigger, and SLD beams with progressive frequency triggers.

The beams are tested both for capped and uncapped frontal ends as mentioned before. An capped end offers an advantage that the front end may not distort and have an unpredictable contact area with the inclined wall as shown in Fig. 5.11 and cause uncertain/erratic transformation from axial to bending.

However, capped end may hypothetically have a disadvantage also in inclined collapse. A capped ridged end may hinder the triggers to initiate a stable buckling, causing spikes and thus causing stray deformations on the beam.

For this reason, both have been tested and their results are compared.

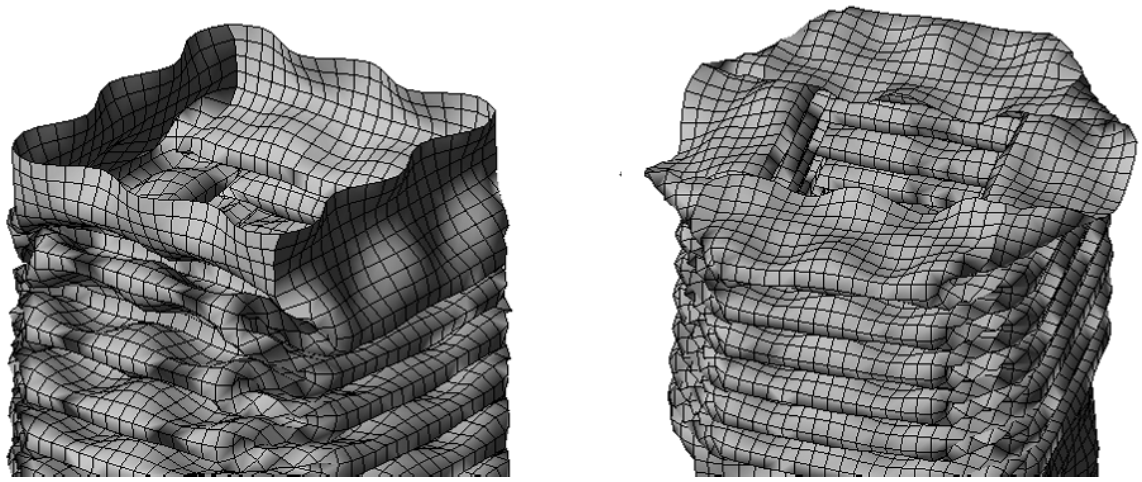

Impact end capped (rigid)

Impact end uncapped

Fig. 5.11. Uncapped impact end and capped impact end.

5.4.4 FEM Results: Critical angle

All samples are tested at 1 degree intervals of inclination up to 8 degrees. Fig. 5.12 shows the energy absorbed by the SLD16-P1 beam at various degrees of inclination. As energy dissipation and average reaction force decrease drastically as soon as the collapse mode changes from axial to global bending, it would be desirable to have a beam with a higher critical angle on which the transition takes place. The critical angle, thus becomes an important perimeter for assessing the performance.

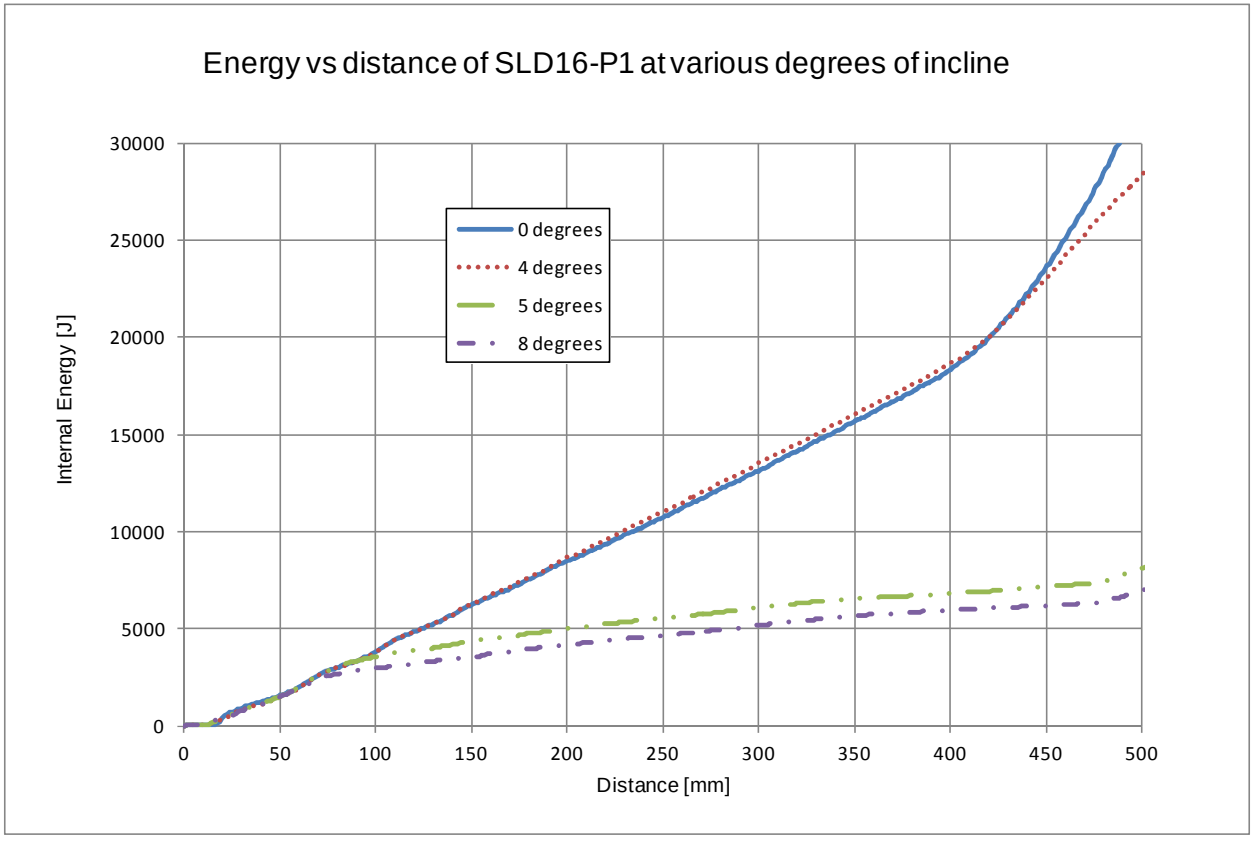

Fig. 5.12 Energy absorbed by the SLD16-P1 beam at various degrees of inclination.

The average collapse force vs. angle for uncapped models is shown in Fig. 5.13. The reference model has a critical angle of roughly 4 degrees. Notch triggered beams in uncapped model

behaved the worse with a critical angle of roughly 2.5 degrees. This may partly be because notch triggers do not work well for SLD beams and partly because of uneven impact surface. The progressively triggered beams showed the most resilient behavior and had the highest critical angle of all beams.

There was a fair degree of erratic behavior in the results. SLD13 and SLD16 behaved erratically (collapsing in global bending) at one degree inclination, SLD16-P2 also behaved erratically at 6 degree inclination. The critical angle results are summarized in Table 5.2.

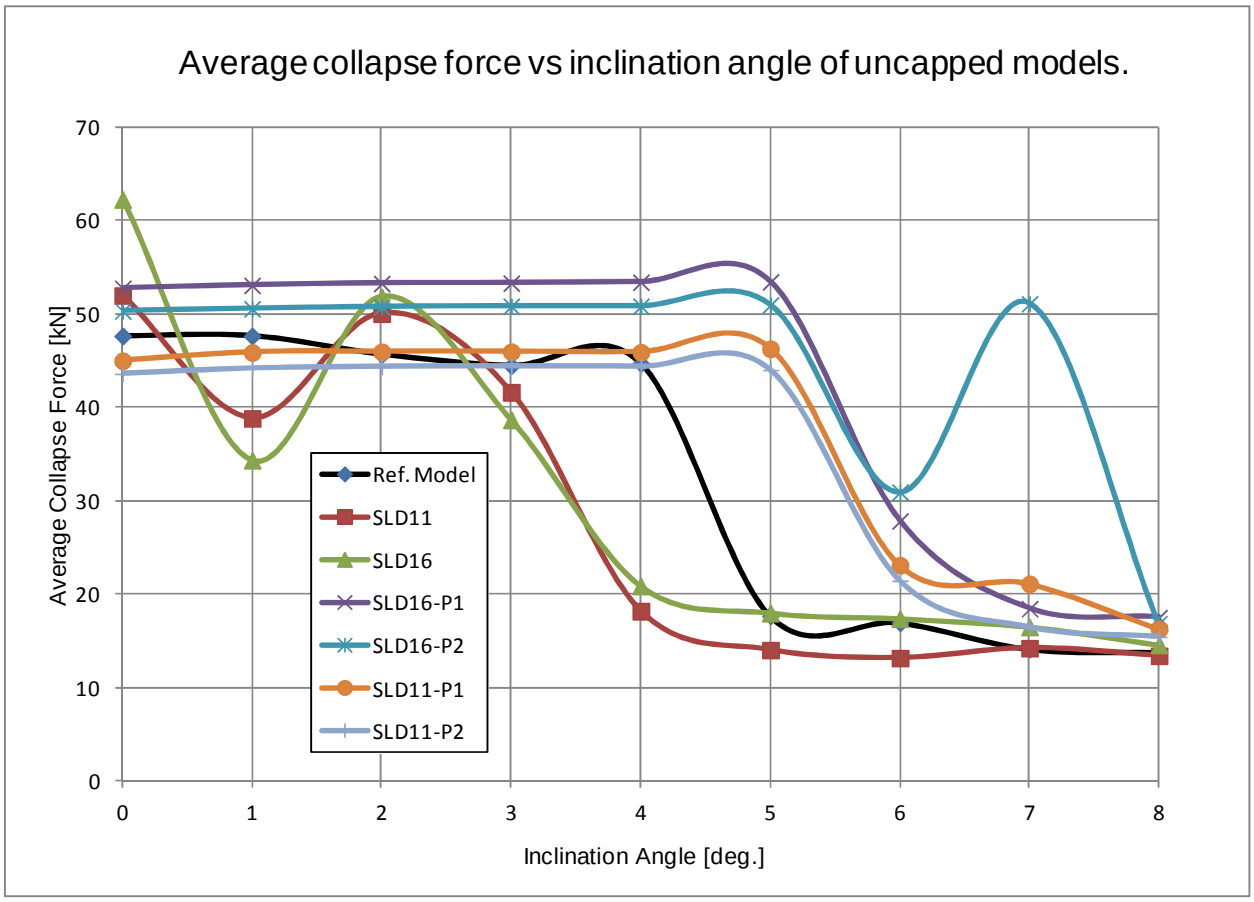

Fig.5.13 Average collapse force vs. angle for uncapped models.

Model	λ_1 (mm)	λ_2 (mm)	$\alpha_{1,2}$ (mm)	λ_3 (mm)	Min λ_3 amp	Max λ_3 amp	λ_3Progression	Critical Angle range (mm)
REFERENCE MODEL								
Ref Mod.	-	-	-	-	-	-	-	4.5
NOTCH TRIGGERS								
SLD11	30	40	2	60	0.3	.3	-	3
SLD16	25	28.57	2	50	.3	.3	-	3
PROGRESSIVE TRIGGERS								
SLD11-P1	30	40	2	60	0.16	1.16	LINEAR	5.5
SLD11-P2	30	40	2	60	0.16	1.66	LINEAR	5.5
SLD16-P1	25	28.57	2	50	0.16	1.16	LINEAR	5.5
SLD16-P2	25	28.57	2	50	0.16	1.66	LINEAR	7.5

Table 5.2. The critical angle results for uncapped beams.

The capped model had more persistent results than the uncapped model. Only one reading, i.e. SLD16 at 1 degree was erratic as shown in Fig. 5.14.

Another interesting fact was that the SLD notch triggered beams almost the same as the reference beam, unlike in the un-capped test. Progressively triggered SLD beams performed the best in this case too. The results are summarized in Table 5.3. Owing to its reliability, the capped test is considered a better criteria for judging inclined impacts.

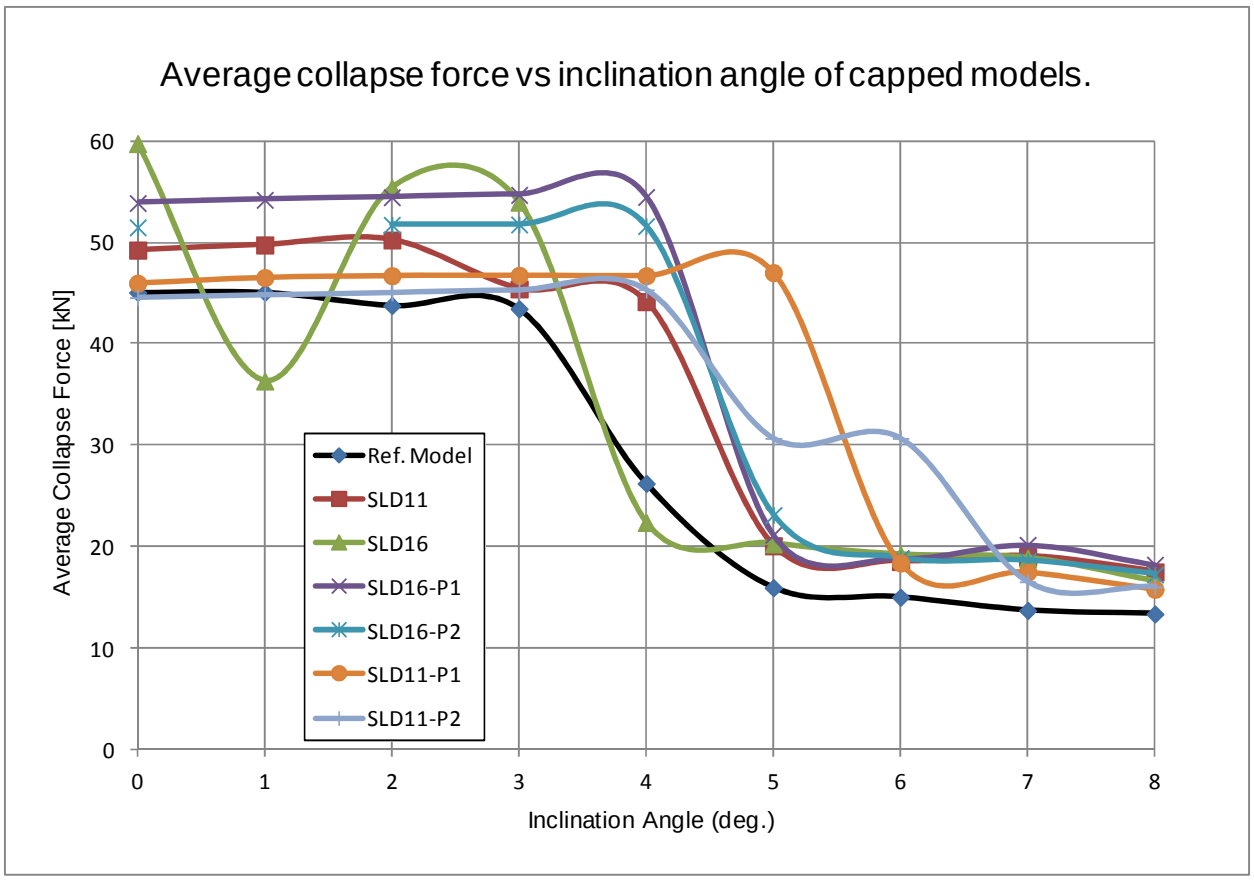

Fig.5.14 Average collapse force vs. angle for capped models.

Model	λ_1 (mm)	λ_2 (mm)	$\alpha_{1,2}$ (mm)	λ_3 (mm)	Min λ_3 amp	Max λ_3 amp	λ_3 Progression	Critical Angle range (mm)
REFERENCE MODEL								
Ref Mod.	-	-	-	-	-	-	-	4
NOTCH TRIGGERS								
SLD11	30	40	2	60	0.3	.3	-	4.5
SLD16	25	28.57	2	50	.3	.3	-	3.5
PROGRESSIVE TRIGGERS								

SLD11-P1	30	40	2	60	0.16	1.16	LINEAR	5.5
SLD11-P2	30	40	2	60	0.16	1.66	LINEAR	5.5
SLD16-P1	25	28.57	2	50	0.16	1.16	LINEAR	5.5
SLD16-P2	25	28.57	2	50	0.16	1.66	LINEAR	5.5

Table 5.3. The critical angle results for capped beams.

5.5 Conclusions

SLD Patterned beams with notch triggers, and SLD patterned beams with progressive triggers have been tested successfully for behavior in oblique and offset impacts.

In all three tests carried out, namely, the offset-mass impact test, oblique impact test with capped front end and oblique impact test with uncapped front end, SLD beams with progressive triggers had the best performance.

Offset-mass impact test proved to be slightly an unreliable measure of testing beam performance. Among oblique capped and uncapped tests, capped test were more reliable and had less erratic readings therefore can be claimed as the best testing criteria.

References:

1 Alexander JM, An approximate analysis of the collapse of thin cylindrical shells under axial loading, Q. J. Mechanics and Appl. Math. 13(1), (1960) 10–15.

2. W.Abramowicz, Thin Walled structures as impact energy absorbers.. Thin Walled Structures.41(2003). 91-107.

3. W. Abramowicz, . T Wierzbicki, Axial crushing of multi corner sheet metal columns, J Appl. Mech. Tran. ASME,56(1), (1989) 113–120.

4.T. Wierzbicki, W.Abramowicz, On the crushing mechanics of thin walled structures. J Appl. Mech. Trans. ASME 50(4a), (1983), 727–734.

5. W. Abramowicz, N.Jones, Dynamic axial crushing of square tube, Int. J. Impact. Eng. 2(2) (1984) 179–208.

6. W. Abramowicz, N. Jones, Dynamic progressive buckling of circular and square tubes, Int. J. Impact Eng. 4(4), (1986) 243–270.

7. D. Kecman, An engineering approach to Crashworthiness of thin-walled beams and Joints in Vehicle Structures, Thin-Walled Structures. 28, (1997) 309-320.

8. T. Wierzbicki, Crash behavior of box columns filled with aluminum honeycomb or foam. Comp. Struct. 68(4) (1998) 343–367.

9. LIU, Yu-cheng, Improved concept models for straight thin-walled columns with box cross section, Journal of Zhejiang University Science, 9(11), (2008) 1473-1479.

10. Yucheng Liu, Optimum design of straight thin-walled box section beams for crashworthiness analysis,.Finete Elements in Analysis and Design.44(3),(2008) 139-147.

11. H.-S. Kim, W. Chen, T. Wierzbicki, Weight and crash optimization of foam-filled three-dimensional‘‘S’’ frame. Computational Mechanics 28 (2002) 417–424.

12. Seitzberger M., Rammerstorfer F.G., Gradinger R., Degischer H.P., Blaimschein M., Walch C., Experimental Studies on the Quasi-Static Axial Crushing of Steel Columns Filled with Aluminium Foam,
Int.J.Sol.Struct. 37,(2000) 4125-4147.

13. A.G. Hanssen, M. Langseth, O.S. Hopperstad, Static and dynamic crushing of circular aluminum extrusions with aluminum foam filler, Int. J. Impact Eng. 24(5)(2000) 475–507.

14. S.R. Reid, T.Y. Reddy, M.D. Gray, Static and dynamic axial crushing of foam-filled sheet metal tubes, Int. J. Mech. Sci. 28(5),(1986) 295–322.

15. A.G. Hanssen, M. Langseth, O.S. Hopperstad, Optimum design for energy absorption of square aluminum columns with aluminum foam filler, Int. J. Mech. Sci, 43(1),(2001) 153–176.

16. Xiong Zhang, Gengdong Cheng, Hui Zhang, Theoretical prediction and numerical simulation of multi-cell square thin-walled structures,. Thin-Walled Structures 44 (2006) 1185–1191.

17. Kim, Heung-Soo, New extruded multi-cell aluminum profile for maximum crash energy absorption and weight efficiency, Thin-Walled Structures 40 (2002) 311–327.

18. X. W. Zhang, Q. D. Tian, T. X.Yu., Axial crushing of circular tubes with buckling initiators., Thin-Walled Structures 47 (2009) 788–797.

19. S.J. Hosseinipour, G.H. Daneshi, Energy absorbtion and mean crushing load of thin-walled grooved tubes under axial compression, Thin-Walled Structures 41 (2003) 31-46.

20. Sunghak Leea, Changsu Hahn, Meungho Rhee, Jae-Eung Ohd, Effect of triggering on the energy absorption capacity of axially compressed aluminum tubesMaterials and Design 20 (1999) 31-40.

21. X. Zhang, G. Cheng, Z. You, H. Zhang, Energy absorption of axially compressed thin-walled square tubes with patterns, Thin-Walled Structures 45, (2007) 737–746.

22. W. Jiang, J.L. Yang, Energy-absorption behavior of a metallic double-sine-wave beam under axial
crushing, Thin-Walled Structures 47 (2009) 1168–1176.

23. Norman Jones, Energy absorbing effectiveness factor, Journal of Impact Engineering, 37(6),(2010), 754-765.

24. X.W. Zhang, H. Su, T.X. Yu, Energy absorption of an axially crushed square tube with a buckling initiator, International Journal of Impact Engineering 36 (2009) 402–417.

25. Recep Fumruk, Sami, Karadeniz, A numerical study of bump type triggers on the axial crushing of top hat thin-walled section, Thin-Walled Structures 46 (2008) 1094–1106.

26. Minoru Yamashita, Hiromasa Kenmotsu, Toshio Hattori, Dynamic axial compression of aluminum hollow tubes with hat cross-section and buckling initiator using inertia force during impact, Thin-Walled Structures 50 (2012) 37–44.

27. Yong-Bum Cho, Chul-Ho Bae, Myung-Won Suh, Hyo-Chol Sin, vehicle front frame crash design optimization using hole-type and dent-type crush initiator, Thin-Walled Structures, 44 (2006) 415–428.

28 Kecman D. Bending collapse of rectangular and square tubes. Int J Mech Sci 1983;25(9-10):623–36

29 Abramowicz W. "Simplified crushing analysis of thin walled columns and beams". Engng. Trans 1981;29(1) pp 5-26

30 T.H. Kim, S.R. Reid "Bending collapse of thin-walled rectangular section columns" Computers and Structures 79 (2001) 1897-1911

31 M. Khtelko, T.H.Lim, J. Rhodes, "Post-failure behavior of box section beams under pure bending (an experimental study)" .Thin walled Structures 38 (2000) 179-194

32 Edmundo Corona, Suhas P. Vaze, "Buckling of elastic Plastic Square tubes Under Bending" Int:J.Mech. Sci. Vol. 38 pp753-775,1996.

33 P.Drazetic et al. "Calculation of deep bending collapse response for complex thin-walled columns I. Pre-collapse and collapse phases" thin-walled Structures 33 (1999) 155-176.

34 E. Markiewicz, F. Payen, D. Cornette, P. Drazetic, "Calculation of the deep bending collapse response for complex thin-walled columns II. Post-collapse phase" Thin-Walled Structures 33 (1999) 177–210

35 P Hosseini-Tehrani1 and M Nikahd "Effects of ribs on S-frame crashworthiness" Proc. IMechE Vol. 220 Part D*: J. Automobile Engineering* ,1679- 1689

36 McIvor, I.K., Anderson, W.J. and Bijak-Zochowski, M., 'An experimental study of the large deformation of plastic hinges', *Int. J. Solid Structures* **13**, 1977, 53–61.

37 GUY BIAKEU and LOUIS JÉZÉQUEL "Simplified Crash Models Using Plastic Hinges and the Large Curvature Description" *Multibody System Dynamics* **9:** 25–37, 2003.

38 D. Kecman "An Engineering Approach to Crashworthiness of Thin-Walled Beams and Joints in Vehicle Structures" *Thin-Walled Structures* Vol. 28,. 309-320, 1997

39 Giovanni Belingardi, Lorenzo Peroni "Numerical Investigation on plastic collapse of thin walled beams subjected to biaxial bending" *VIII International Conference on Computational Plasticity COMPLAS VIII, Ó CIMNE,* Barcelona, 2005

40 Frode Paulsen, Torgeir Welo, Odd Perry Sovik, "A design method for rectangular hollow sections in bending*" Journal of Materials processing technology* 113 (2001) 699-704

41 Suh. MS. Plastic analysis of dented tubes subject to combined loading, PhD thesis, Massachusetts Institute of Technology. 1987.

42 N. E. Shanmugam, J. Y. Richard Liew & S. L. Lee, Welded Steel Box,Columns under Biaxiai Loading, *J. Construct. Steel Research* 12 (1989) 119-139.

43 Reyes A, Langseth M, Hopperstad OS. Crashworthiness of aluminium extrusions subjected to oblique loading: experiments and numerical analyses. Int J Mech Sci 2002;44:1965–84.

44 A. Reyes, M. Langseth, O.S. Hopperstad, Square aluminum tubes subjected to oblique loading, International Journal of Impact Engineering 28 (2003) 1077–1106.

45 Wallentowitz H, Adam H. Predicting the crashworthiness of vehicle structures made by lightweight design materials and innovative joining methods. Int J Crashworthiness 1996;1(2):163–80.

46 Borvik T, Hopperstad OS, Reyes A, Langseth M, Solomos G, Dyngeland T. Empty and foam-filled circular aluminium tubes subjected to axial and oblique quasi-static loading. Int J Crashworthiness 2003;8(5):481–94.

47 Reyes A, Hopperstad OS, Langseth M. Aluminum foam-filled extrusions subjected to oblique loading: experimental and numerical study. Int J Solids Struct 2004;41:1645–75.

48 Han DC, Park SH. Collapse behavior of square thin-walled columns subjected to oblique loads. Thin-Walled Structures 1999;35:167–84.

49 Kim H-S, Wierzbicki T. Crush behavior of thin-walled prismatic columns under combined bending and compression. Comput Struct 2001;79:1417–32.

50 G.M. Nagel, D.P. Thambiratnam, Dynamic simulation and energy absorption of tapered thin-walled tubes under oblique impact loading, International Journal of Impact Engineering 32 (2006) 1595–1620.

51 S. R. Reid and T. Y. Reddy, Static and dynamic crushing of tapered metal sheet metal tubes of rectangular cross section, Int. J. Mech. Sci, Vol. 28, No. 9, pp, 623~37, 1986.

Appendix 1. Mathematical formulation for all beams tested

#	Name	Formulation, (for all walls where different)
C08T	ZE1	x=50+(sin(((z/2)+y)*pi/20))*sin(((z/2)-y)*pi/20)*2
		y=50+(cos(((z/2)+y)*pi/20))*cos(((z/2)-y)*pi/20)*2
		y=50+(cos(((z/2)+y)*pi/20))*cos(((z/2)-y)*pi/20)
c09t	ZE2	x=-50-(COS(((z/1.5)+y)*pi/20))*COS(((z/1.5)-y)*pi/20)
		y=-50-(COS(((z/1.5)+x)*pi/20))*COS(((z/1.5)-x)*pi/20)
		x=-50+(-COS(z*pi/20))*cos(x*pi/20)/2-(cos(z*pi/20))/2

		y=-50-(cos(((z/1.5)+x)*pi/20))*cos(((z/1.5)-x)*pi/20)-cos(z*pi/20)
c10t	TR1	50+(cos(((z/1.5)+y)*pi/20))*cos(((z/1.5)-y)*pi/20)+cos(y*pi/20)
c11t	F1	x=-50+(-COS(z*pi/50))*cos(x*pi/20)
c12t	A1	x=-50-(COS(y*pi/20))
c13t	SA1	50-cos(x*pi/33.33)*abs(cos(z*pi/50))*2
114t	SA2	50-cos(x*pi/33.33)*abs(cos(z*pi/40))*2
c15t	SA3	50-cos(x*pi/33.33)*abs(cos(z*pi/35))*2
c16t	SA4	50-cos(x*pi/33.33)*abs(cos(z*pi/90))*2
c17t	SLo1	50-cos(x*pi/33.33)*((cos((z+0)*pi/45))+1)*2
		50-cos(y*pi/33.33)*((cos((z+45)*pi/45))+1)*2
c18t	SL2	50-cos(y*pi/33.33)*((cos((z+35)*pi/35))+1)*2
		50-cos(x*pi/33.33)*((cos((z+0)*pi/35))+1)*2
c19t	SL3	
		50-cos(y*pi/33.33)*((cos((z+0)*pi/35))+1)*2
		50-cos(y*pi/33.33)*((cos((z+0)*pi/35))+1)*2
c20	SL4	50-cos(y*pi/33.33)*((cos((z+0)*pi/25))+1)*2
		50-cos(x*pi/33.33)*((cos((z+0)*pi/25))+1)*2
c21	SL5	50-cos(x*pi/33.33)*((cos((z+0)*pi/30))+1)*2
		50-cos(x*pi/33.33)*((cos((z+0)*pi/30))+1)*2
c22	SL6	50-cos(x*pi/33.33)*((cos((z+0)*pi/20))+1)*2
		50-cos(x*pi/33.33)*((cos((z+0)*pi/20))+1)*2
c23	SLD1	h=50-(cos(x*pi/33.33)*((cos((z+0)*pi/20))+1)*2)+((sin(z*pi/40))*.3)
		h=-50+(cos(x*pi/33.33)*((cos((z+0)*pi/20))+1)*2)-((sin(z*pi/40))*0.3)
		v=50-(cos(y*pi/33.33)*((cos((z+0)*pi/20))+1)*2)-((sin(z*pi/40))*.3)
		v=-50+(cos(y*pi/33.33)*((cos((z+0)*pi/20))+1)*2)+((sin(z*pi/40))*.3)

c24	SLD2	h=50-(cos(x*pi/33.33)*((cos((z+0)*pi/20))+1)*2)+((sin(z*pi/40))*.15)
		h=-50+(cos(x*pi/33.33)*((cos((z+0)*pi/20))+1)*2)-((sin(z*pi/40))*0.15)
		v=50-(cos(y*pi/33.33)*((cos((z+0)*pi/20))+1)*2)-((sin(z*pi/40))*.15)
		v=-50+(cos(y*pi/33.33)*((cos((z+0)*pi/20))+1)*2)+((sin(z*pi/40))*.15)
		h=50-(cos(x*pi/33.33)*((cos((z+0)*pi/17))+1)*2)+((sin(z*pi/34))*.15)
c25	SLD3	h=-50+(cos(x*pi/33.33)*((cos((z+0)*pi/17))+1)*2)-((sin(z*pi/34))*0.15)
		v=50-(cos(y*pi/33.33)*((cos((z+0)*pi/17))+1)*2)-((sin(z*pi/34))*.15)
		v=-50+(cos(y*pi/33.33)*((cos((z+0)*pi/17))+1)*2)+((sin(z*pi/34))*.15)
c26	SLD4	h=50-(cos(x*pi/33.33)*((cos((z+0)*pi/15))+1)*2)+((sin(z*pi/30))*.15)
		h=-50+(cos(x*pi/33.33)*((cos((z+0)*pi/15))+1)*2)-((sin(z*pi/30))*0.15)
		v=50-(cos(y*pi/33.33)*((cos((z+0)*pi/15))+1)*2)-((sin(z*pi/30))*.15)
		v=-50+(cos(y*pi/33.33)*((cos((z+0)*pi/15))+1)*2)+((sin(z*pi/30))*.15)
c27	SLD5	h=50-(cos(x*pi/33.33)*((cos((z+0)*pi/17))+1)*2)+((sin(z*pi/34))*.3)
		h=-50+(cos(x*pi/33.33)*((cos((z+0)*pi/17))+1)*2)-((sin(z*pi/34))*0.3)
		v=50-(cos(y*pi/33.33)*((cos((z+0)*pi/17))+1)*2)-((sin(z*pi/34))*.3)
		v=-50+(cos(y*pi/33.33)*((cos((z+0)*pi/17))+1)*2)+((sin(z*pi/34))*.3)
c28	SLD6	h=50-(cos(x*pi/20)*((cos((z+0)*pi/17))+1)*2)+((sin(z*pi/34))*.3)
		h=-50+(cos(x*pi/20)*((cos((z+0)*pi/17))+1)*2)-((sin(z*pi/34))*0.3)
		v=50-(cos(y*pi/20)*((cos((z+0)*pi/17))+1)*2)-((sin(z*pi/34))*.3)
		v=-50+(cos(y*pi/20)*((cos((z+0)*pi/17))+1)*2)+((sin(z*pi/34))*.3)
c29	SLD7	h=50-(cos(x*pi/20)*((cos((z+0)*pi/17))+1)*2)+((sin(z*pi/34))*.3)
		h=-50+(cos(x*pi/20)*((cos((z+0)*pi/17))+1)*2)-((sin(z*pi/34))*0.3)
		v=50+(cos(y*pi/20)*((cos((z+0)*pi/17))+1)*2)-((sin(z*pi/34))*.3)
		v=-50-(cos(y*pi/20)*((cos((z+0)*pi/17))+1)*2)+((sin(z*pi/34))*.3)
c30	SLD8	h=50+(cos(x*pi/20)*((cos((z+0)*pi/17))+1)*2)+((sin(z*pi/34))*.3)
		h=-50-(cos(x*pi/20)*((cos((z+0)*pi/17))+1)*2)-((sin(z*pi/34))*0.3)
		v=50+(cos(y*pi/20)*((cos((z+0)*pi/17))+1)*2)-((sin(z*pi/34))*.3)
		v=-50-(cos(y*pi/20)*((cos((z+0)*pi/17))+1)*2)+((sin(z*pi/34))*.3)
c31	SLD9	50-cos(y*pi/33.33)*((cos((z+0)*pi/34))+0)*2=((sin(z*pi/34))*.3)
		50-cos(y*pi/33.33)*((cos((z+0)*pi/34))+0)*2=((sin(z*pi/34))*.3)
		50-cos(y*pi/33.33)*((cos((z+0)*pi/34))+0)*2=((sin(z*pi/34))*.3)
		50-cos(y*pi/33.33)*((cos((z+0)*pi/34))+0)*2=((sin(z*pi/34))*.3)
c32	SLD10	h=50+(cos(x*pi/20)*((cos((z+0)*pi/15))+1)*2)+((sin(z*pi/30))*.3)
		h=-50-(cos(x*pi/20)*((cos((z+0)*pi/15))+1)*2)-((sin(z*pi/30))*0.3)
		v=50+(cos(y*pi/20)*((cos((z+0)*pi/15))+1)*2)-((sin(z*pi/30))*.3)

		v=-50-(cos(y*pi/20)*((cos((z+0)*pi/15))+1)*2)+((sin(z*pi/30))*.3)
		h=50+(cos(x*pi/20)*((cos((z+0)*pi/15))+1)*2)+((sin(z*pi/30))*.15)
c33	SLD11	h=-50-(cos(x*pi/20)*((cos((z+0)*pi/15))+1)*2)-((sin(z*pi/30))*.15)
		v=50+(cos(y*pi/20)*((cos((z+0)*pi/15))+1)*2)-((sin(z*pi/30))*.15)
		v=-50-(cos(y*pi/20)*((cos((z+0)*pi/15))+1)*2)+((sin(z*pi/30))*.15)
c34	SLD12	h=50+(cos(x*pi/20)*((cos((z+0)*pi/13))+1)*2)+((sin(z*pi/26))*.3)
		h=-50-(cos(x*pi/20)*((cos((z+0)*pi/13))+1)*2)-((sin(z*pi/26))*.3)
		v=50+(cos(y*pi/20)*((cos((z+0)*pi/13))+1)*2)-((sin(z*pi/26))*.3)
		v=-50-(cos(y*pi/20)*((cos((z+0)*pi/13))+1)*2)+((sin(z*pi/26))*.3)
		h=50-(cos(x*pi/14.2857)*((cos((z+0)*pi/13))+1)*2)+((sin(z*pi/26))*.3)
c35	SLD13	h=-50+(cos(x*pi/14.2857)*((cos((z+0)*pi/13))+1)*2)-((sin(z*pi/26))*.3)
		v=50-(cos(y*pi/14.2857)*((cos((z+0)*pi/13))+1)*2)-((sin(z*pi/26))*.3)
		v=-50+(cos(y*pi/14.2857)*((cos((z+0)*pi/13))+1)*2)+((sin(z*pi/26))*.3)
		h=50-(cos(x*pi/14.2857)*((cos((z+0)*pi/10))+1)*2)+((sin(z*pi/20))*.3)
c36	SLD14	h=-50+(cos(x*pi/14.2857)*((cos((z+0)*pi/10))+1)*2)-((sin(z*pi/20))*.3)
		v=50-(cos(y*pi/14.2857)*((cos((z+0)*pi/10))+1)*2)-((sin(z*pi/20))*.3)
		v=-50+(cos(y*pi/14.2857)*((cos((z+0)*pi/10))+1)*2)+((sin(z*pi/20))*.3)
c37	SLD15	h=50-(cos(x*pi/14.2857)*((cos((z+0)*pi/12.5))+1)*2)+((sin(z*pi/25))*.15)
		h=-50+(cos(x*pi/14.2857)*((cos((z+0)*pi/12.5))+1)*2)-((sin(z*pi/25))*.15)
		v=50-(cos(y*pi/14.2857)*((cos((z+0)*pi/12.5))+1)*2)-((sin(z*pi/25))*.15)
		v=-50+(cos(y*pi/14.2857)*((cos((z+0)*pi/12.5))+1)*2)+((sin(z*pi/25))*.15)
		h=50-(cos(x*pi/14.2857)*((cos((z+0)*pi/12.5))+1)*2)+((sin(z*pi/25))*.1)
c38	SLD16	h=-50+(cos(x*pi/14.2857)*((cos((z+0)*pi/12.5))+1)*2)-((sin(z*pi/25))*.1)
		v=50-(cos(y*pi/14.2857)*((cos((z+0)*pi/12.5))+1)*2)-((sin(z*pi/25))*.1)
		v=-50+(cos(y*pi/14.2857)*((cos((z+0)*pi/12.5))+1)*2)+((sin(z*pi/25))*.1)
c39	SLD17	h=50-(cos(x*pi/14.2857)*((cos((z+0)*pi/13))+1)*1)+((sin(z*pi/26))*.1)
		h=-50+(cos(x*pi/14.2857)*((cos((z+0)*pi/13))+1)*1)-((sin(z*pi/26))*.1)
		v=50-(cos(y*pi/14.2857)*((cos((z+0)*pi/13))+1)*1)-((sin(z*pi/26))*.1)
		v=-50+(cos(y*pi/14.2857)*((cos((z+0)*pi/13))+1)*1)+((sin(z*pi/26))*.1)
c40	SLD18	h=50-(cos(x*pi/14.2857)*((cos((z+0)*pi/13))+1)*1)+((sin(z*pi/26))*.3)
		h=-50+(cos(x*pi/14.2857)*((cos((z+0)*pi/13))+1)*1)-((sin(z*pi/26))*.3)
		v=50-(cos(y*pi/14.2857)*((cos((z+0)*pi/13))+1)*1)-((sin(z*pi/26))*.3)
		v=-50+(cos(y*pi/14.2857)*((cos((z+0)*pi/13))+1)*1)+((sin(z*pi/26))*.3)
c41	SLD19	h=50+(cos(x*pi/20)*((cos((z+0)*pi/15))+1)*1)+((sin(z*pi/30))*.3)

		h=-50-(cos(x*pi/20)*((cos((z+0)*pi/15))+1)*1)-((sin(z*pi/30))*.3)
		v=50+(cos(y*pi/20)*((cos((z+0)*pi/15))+1)*1)-((sin(z*pi/30))*.3)
		v=-50-(cos(y*pi/20)*((cos((z+0)*pi/15))+1)*1)+((sin(z*pi/30))*.3)
c42	B1	x=-50-(COS(z*pi/20))
		x=-50-(COS(z*pi/20))
c43	B2	x=-50-(COS(z*pi/30))
		x=-50+(COS(z*pi/30))
c45	SLD13-P1	h=50-(cos(x*pi/14.2857)*((cos((z+0)*pi/13))+1)*2)+sin(z*pi/26)*(.05+(z/1200)^2)
		h=-50+(cos(x*pi/14.2857)*((cos((z+0)*pi/13))+1)*2)-sin(z*pi/26)*(.05+(z/1200)^2)
		v=50-(cos(y*pi/14.2857)*((cos((z+0)*pi/13))+1)*2)-sin(z*pi/26)*(.05+(z/1200)^2)
		v=-50+(cos(y*pi/14.2857)*((cos((z+0)*pi/13))+1)*2)+sin(z*pi/26)*(.05+(z/1200)^2)
c46	SLD13-P2	h=50-(cos(x*pi/14.2857)*((cos((z+0)*pi/13))+1)*2)+sin(z*pi/26)*(.1+(z/1200)^3)
		h=-50+(cos(x*pi/14.2857)*((cos((z+0)*pi/13))+1)*2)-sin(z*pi/26)*(.1+(z/1200)^3)
		v=50-(cos(y*pi/14.2857)*((cos((z+0)*pi/13))+1)*2)-sin(z*pi/26)*(.1+(z/1200)^3)
		v=-50+(cos(y*pi/14.2857)*((cos((z+0)*pi/13))+1)*2)+sin(z*pi/26)*(.1+(z/1200)^3)
c47	SLD13-P3	h=50-(cos(x*pi/14.2857)*((cos((z+0)*pi/13))+1)*2)+sin(z*pi/26)*(.16+(z/1200)^3)
		h=-50+(cos(x*pi/14.2857)*((cos((z+0)*pi/13))+1)*2)-sin(z*pi/26)*(.16+(z/1200)^3)
		v=50-(cos(y*pi/14.2857)*((cos((z+0)*pi/13))+1)*2)-sin(z*pi/26)*(.16+(z/1200)^3)
		v=-50+(cos(y*pi/14.2857)*((cos((z+0)*pi/13))+1)*2)+sin(z*pi/26)*(.16+(z/1200)^3)
c48	SLD13-P4	h=50-(cos(x*pi/14.2857)*((cos(z*pi/13))+1)*2)+sin(z*pi/26)*(.16+((z/1200)^2)/2)
		h=-50+(cos(x*pi/14.2857)*((cos(z*pi/13))+1)*2)-sin(z*pi/26)*(.16+((z/1200)^2)/2)
		v=50-(cos(y*pi/14.2857)*((cos(z*pi/13))+1)*2)-sin(z*pi/26)*(.16+((z/1200)^2)/2)
		v=-50+(cos(y*pi/14.2857)*((cos(z*pi/13))+1)*2)+sin(z*pi/26)*(.16+((z/1200)^2)/2)
c49	SLD13-P5	h=50-(cos(x*pi/14.2857)*((cos(z*pi/13))+1)*2)+sin(z*pi/26)*(.16+(z/1200)/2)

		h=-50+(cos(x*pi/14.2857)*((cos(z*pi/13))+1)*2)-sin(z*pi/26)*(.16+(z/1200)/2)
		v=50-(cos(y*pi/14.2857)*((cos(z*pi/13))+1)*2)-sin(z*pi/26)*(.16+(z/1200)/2)
		v=-50+(cos(y*pi/14.2857)*((cos(z*pi/13))+1)*2)+sin(z*pi/26)*(.16+(z/1200)/2)
c50	SLD13-P6	h=50-(cos(x*pi/14.2857)*((cos(z*pi/13))+1)*2)+sin(z*pi/26)*(.16+((z/1200)^3)/2)
		h=-50+(cos(x*pi/14.2857)*((cos(z*pi/13))+1)*2)-sin(z*pi/26)*(.16+((z/1200)^3)/2)
		v=50-(cos(y*pi/14.2857)*((cos(z*pi/13))+1)*2)-sin(z*pi/26)*(.16+((z/1200)^3)/2)
		v=-50+(cos(y*pi/14.2857)*((cos(z*pi/13))+1)*2)+sin(z*pi/26)*(.16+((z/1200)^3)/2)
c51	SLD13-P7	h=50-(cos(x*pi/14.2857)*((cos(z*pi/13))+1)*2)+sin(z*pi/26)*(.16+(z/1200))
		h=-50+(cos(x*pi/14.2857)*((cos(z*pi/13))+1)*2)-sin(z*pi/26)*(.16+(z/1200))
		v=50-(cos(y*pi/14.2857)*((cos(z*pi/13))+1)*2)-sin(z*pi/26)*(.16+(z/1200))
		v=-50+(cos(y*pi/14.2857)*((cos(z*pi/13))+1)*2)+sin(z*pi/26)*(.16+(z/1200))
c52	SLD16-P1	h=50-(cos(x*pi/14.2857)*((cos((z+0)*pi/12.5))+1)*2)+(sin(z*pi/25)*(.16+z/2400))
		h=-50+(cos(x*pi/14.2857)*((cos((z+0)*pi/12.5))+1)*2)-(sin(z*pi/25)*(.16+z/2400))
		v=50-(cos(y*pi/14.2857)*((cos((z+0)*pi/12.5))+1)*2)-(sin(z*pi/25)*(.16+z/2400))
		v=-50+(cos(y*pi/14.2857)*((cos((z+0)*pi/12.5))+1)*2)+(sin(z*pi/25)*(.16+z/2400))
c53	SLD16-P2	h=50-(cos(x*pi/14.2857)*((cos((z+0)*pi/12.5))+1)*2)+(sin(z*pi/25)*(.16+z/1800))
		h=-50+(cos(x*pi/14.2857)*((cos((z+0)*pi/12.5))+1)*2)-(sin(z*pi/25)*(.16+z/1800))
		v=50-(cos(y*pi/14.2857)*((cos((z+0)*pi/12.5))+1)*2)-(sin(z*pi/25)*(.16+z/1800))
		v=-50+(cos(y*pi/14.2857)*((cos((z+0)*pi/12.5))+1)*2)+(sin(z*pi/25)*(.16+z/1800))
c55	SLD16-P3	h=50-(cos(x*pi/14.2857)*((cos((z+0)*pi/12.5))+1)*2)+(sin(z*pi/25)*(.16+(z/1200)))
		h=-50+(cos(x*pi/14.2857)*((cos((z+0)*pi/12.5))+1)*2)-(sin(z*pi/25)*(.16+z/1200))
		v=50-(cos(y*pi/14.2857)*((cos((z+0)*pi/12.5))+1)*2)-(sin(z*pi/25)*(.16+z/1200))
		v=-50+(cos(y*pi/14.2857)*((cos((z+0)*pi/12.5))+1)*2)+(sin(z*pi/25)*(.16+z/1200))

c56	SLD16-P4	h=50-(cos(x*pi/14.2857)*((cos((z+0)*pi/12.5))+1)*2)+(sin(z*pi/25)*(.16+z/800))
		h=-50+(cos(x*pi/14.2857)*((cos((z+0)*pi/12.5))+1)*2)-(sin(z*pi/25)*(.16+z/800))
		v=50-(cos(y*pi/14.2857)*((cos((z+0)*pi/12.5))+1)*2)-(sin(z*pi/25)*(.16+z/800))
		v=-50+(cos(y*pi/14.2857)*((cos((z+0)*pi/12.5))+1)*2)+(sin(z*pi/25)*(.16+z/800))
c57	SLD16shi-P1	h=50-(cos(x*pi/14.2857)*((cos((z+0)*pi/12.5))+1)*2)+(sin(z*pi/25)*(1.16-z/600))
	600mm length	h=-50+(cos(x*pi/14.2857)*((cos((z+0)*pi/12.5))+1)*2)-(sin(z*pi/25)*(1.16-z/600))
		v=50-(cos(y*pi/14.2857)*((cos((z+0)*pi/12.5))+1)*2)-(sin(z*pi/25)*(1.16-z/600))
		v=-50+(cos(y*pi/14.2857)*((cos((z+0)*pi/12.5))+1)*2)+(sin(z*pi/25)*(1.16-z/600))
c58	SLD16shi-P2	h=50-(cos(x*pi/14.2857)*((cos((z+0)*pi/12.5))+1)*2)+(sin(z*pi/25)*(1.66-z/400))
	600mm length	h=-50+(cos(x*pi/14.2857)*((cos((z+0)*pi/12.5))+1)*2)-(sin(z*pi/25)*(1.66-z/400))
		v=50-(cos(y*pi/14.2857)*((cos((z+0)*pi/12.5))+1)*2)-(sin(z*pi/25)*(1.66-z/400))
		v=-50+(cos(y*pi/14.2857)*((cos((z+0)*pi/12.5))+1)*2)+(sin(z*pi/25)*(1.66-z/400))
c59	SLD11-P1	h=50+(cos(x*pi/20)*((cos((z+0)*pi/15))+1)*2)+sin(z*pi/30)*(1.16-z/600)
	600mmlength	h=-50-(cos(x*pi/20)*((cos((z+0)*pi/15))+1)*2)-sin(z*pi/30)*(1.16-z/600)
		v=50+(cos(y*pi/20)*((cos((z+0)*pi/15))+1)*2)-sin(z*pi/30)*(1.16-z/600)
		v=-50-(cos(y*pi/20)*((cos((z+0)*pi/15))+1)*2)+sin(z*pi/30)*(1.16-z/600)
c60	SLD11-P2	h=50+(cos(x*pi/20)*((cos((z+0)*pi/15))+1)*2)+sin(z*pi/30)*(1.66-z/400)
	600mmlength	h=-50-(cos(x*pi/20)*((cos((z+0)*pi/15))+1)*2)-sin(z*pi/30)*(1.66-z/400)
		v=50+(cos(y*pi/20)*((cos((z+0)*pi/15))+1)*2)-sin(z*pi/30)*(1.66-z/400)
		v=-50-(cos(y*pi/20)*((cos((z+0)*pi/15))+1)*2)+sin(z*pi/30)*(1.66-z/400)

……. THE END …….